

**Investigating Impeller Wear and Its Effect on Pump Performance Using Soft  
Materials**

by

Chunyan Jiang

A thesis submitted in partial fulfillment of the requirements for the degree of

Master of Science

Department of Mechanical Engineering  
University of Alberta

© Chunyan Jiang, 2019

# Abstract

This project investigated the abrasive wear problem that commonly occurs in slurry pump impellers. The manufacturers' stock impellers were replaced by samples with the same geometry and fabricated using rapid manufacturing technology (3D printing technology). Soft materials which are often used in 3D printing were selected to build the samples. Garnet-water slurries were employed as the test slurry. Wear experiments with different wear time were conducted for five rotational speeds (1050, 1200, 1350, 1500 and 1750 rpm) and three solid concentrations (5wt.%, 10wt.% and 15wt.%). Pump performance tests were conducted using impellers with different damage conditions.

Using samples with soft materials saves time and costs, and can obtain acceptable similarity to normal conditions. The frequently worn spots are at the upper edge of the blades and near the hub. The solid concentration and flow rate will affect impeller wear rate. The flow rate has a dominant effect. The solid concentration and flow rate have a power relationship with the wear rate. The exponents of flow velocity for 5wt.% and 10wt.% are 2.5152 and 2.9403, respectively. The exponents of concentration for 1050 rpm and 1200 rpm are 1.5153 and 0.5168, respectively. The results in this work are reasonably consistent with previous studies using harder materials. Damaged impellers affect pump performance. A parabolic fit was imposed to describe the head and flow rate relationship. An empirical model was proposed to predict the pump head with damaged impellers. This project found an affinity law for different damage conditions of a certain impeller and coefficients  $C$  in the parabolic fitting functions. The exponent of the affinity law is in the range of 2.5 to 3, and depends on the damage conditions of the impellers. Hydraulic

power will also be affected by abraded impellers. When the rotational speed is high, the damage impeller has less effect on pump performance than when the rotational speed is low.

# Dedication

*In memory of my dearest grandma*

*To my family*

# Acknowledgements

First of all, I would like to show my greatest appreciation to my supervisors, Dr. Brian Fleck and Michael Lipsett. With their patient guidance and useful advice on my research, I can make a great change in my study. I am so lucky to work with both of them. Both of them always encourage me when I was frustrated. Their confidence in my research inspired me greatly. Their attitudes towards life will also affect me greatly in my whole life. I really benefit a lot from their advice not only on academic but also on daily life.

I have received a great deal of assistance from different people in the University of Alberta. I am so grateful for the help from all the staff in the machine shop of the Department of Mechanical Engineering. With their timely assistance, I can finish the project successfully. They are always patient and friendly to give me the advice on producing the samples and fix the problem I came into during the experiment. I would like to express my gratitude to Rick Conrad who can always help me solve electrical problems and lend some instruments to do measurements in the lab. I am so grateful to have many warmhearted friends and lab mates in the University of Albert. I thank all of them for the discussions on the academic problems and problems in my life

I am deeply grateful to my husband, Chen Zhang. Thank you for understanding and supporting me every moment when I am making big decisions in my lifetime. I also would like to thank my parents and sister. You are always encouraging me when I am in downtimes. I owe a very important debt to my parents-in-law. Thank you to support and give warm encouragement in my life. Also, my grandparents are the most important ones that I need to be appreciated. Thank you for raising me up when my parents worked outside the hometown. I love all of my family members.

# Contents

Abstract .....	ii
Dedication .....	iv
Acknowledgements.....	v
Contents .....	vi
List of Tables .....	ix
List of Figures .....	x
Nomenclature.....	xvii
1.Introduction.....	1
1.1 Background.....	1
1.1.1 Slurry pumps.....	1
1.1.2 Abrasive wear in the pump .....	3
1.2 Literature review.....	6
1.2.1 Flow model in the centrifugal pumps .....	6
1.2.2 Wear model.....	7
1.2.3 Abrasive wear mechanism .....	16
1.2.4 Properties of erodent affecting abrasive wear behavior .....	16
1.2.5 Wear location on the impeller.....	18
1.2.6 Wear locations on other wet-end parts in the slurry pumps.....	19
1.2.7 Wear behavior of typical materials applied in the pump .....	20
1.2.8 Indicators for wear behavior .....	21
1.2.9 Experimental methods for wear .....	22
1.2.10 Numerical analysis of flow motion and abrasive wear in the slurry pump.....	24
1.2.11 Pump performance .....	26
1.2.12 Summary of literature review .....	27
1.3 Research objective .....	28
1.4 Thesis outline .....	29
1.5 Current contribution.....	29
2.Experimental Methods.....	31
2.1 Main apparatus in the flow loop .....	31
2.1.1 Pipeloop .....	31
2.1.2 Slurry pump .....	32

2.1.3	Knife-gate valve.....	34
2.1.4	Tanks.....	34
2.2	Measurement Instrument.....	35
2.2.1	Coriolis flow meter .....	35
2.2.2	Pressure sensor.....	36
2.2.3	Tachometer .....	36
2.2.4	Other instruments.....	38
2.3	Erodent material in wear experiments.....	39
2.4	Impeller material in wear experiment .....	41
2.4.1	3D printing technology .....	41
2.4.2	Alternative materials in 3D printing technology.....	42
2.5	Data Acquisition System.....	46
2.6	Calibration.....	48
2.7	The principle of performance experiment.....	50
2.8	Experiment procedure .....	52
2.8.1	Flow capacity /Head ( $Q/H$ ) experiment.....	52
2.8.2	Wear experiment.....	53
3.	Experimental Results .....	57
3.1	Preliminary experimental results .....	57
3.2	Wear pattern observation .....	58
3.3	Degradation of solid particles .....	64
3.4	Relationship of mass loss and wear time .....	66
3.5	Effects of bulk velocity on wear .....	67
3.6	Effects of flow concentration on wear .....	68
3.7	Head of pump affected by a worn impeller.....	69
4.	Discussion .....	76
4.1	Discussion about the method .....	76
4.2	Discussion about the results.....	78
4.2.1	Discussion about the wear pattern .....	78
4.2.2	Discussion about parametric studies .....	79
4.2.3	Discussion about results of H/Q experiments .....	83
4.3	Limitations for the method.....	107
5.	Conclusions and Future Work .....	111
5.1	Conclusions.....	111

5.2 Recommendations for future work.....	113
Bibliography .....	115
Appendices .....	127
A. Data of other percentages of mass loss .....	127
B. 2D drawing for tested samples.....	138
C. Data sheet of performance curves of the pump (Given by manufacturer).....	140
D. NI-DAQmx interface .....	142
E. Dimensional analysis on wear rate from particle perspective.....	145
F. Experimental data of wear tests .....	148



# List of Tables

Table 1.1. Slurry pump classification .....	2
Table 2.1. The range and error of three parameters (Endress+Hauser Group).....	36
Table 2.2. Specification of the photo tachometer/stroboscope .....	37
Table 2.3. Specification of garnets (Sil Industrial Minerals).....	40
Table 2.4. Comparison of ABS, PLA and Verogray mechanical properties (Stratasys Company).....	45
Table 2.5. Comparison of ABS, PLA and Verogray thermal properties (Stratasys Company) .....	46
Table 2.6. Experimental conditions .....	56
Table 4.1. Relationships between flow rate and wear rate at solids concentration 5wt.% and 10 wt.% .....	80
Table 4.2. Relationships between solid concentration and wear rate at rotational speed 1200rpm and 1050 rpm .....	80
Table 4.3. Comparing the exponents in this work to those in previous studies.....	82
Table 4.4. The values of $A$ , $B$ and $C$ for different rotational speeds and damage conditions without fixing any coefficients.....	84
Table 4.5. Coefficient $C$ for different percentages of mass loss at different rotational speeds .....	88
Table 4.6. Flow rate ranges for definite integrals at different rotational speeds .....	99

# List of Figures

Figure 1.1.Recessed impeller pump.....	3
Figure 1.2.Parameters that affect the wear behavior (solid-liquid two-phase flow).....	6
Figure 1.3.Typical sites of abrasive wear (red marks).....	19
Figure 2.1.Schematic of testing loop .....	32
Figure 2.2.Slurry pump and motor.....	33
Figure 2.3.Three wet-end parts .....	34
Figure 2.4.The position for a tachometer.....	38
Figure 2.5.Magnified view of garnets' erodent on 5mm square grid .....	40
Figure 2.6.Samples using three different materials (PLA, ABS, Verogray) .....	43
Figure 2.7.Verogray impeller sample .....	44
Figure 2.8.LabView block program (front interface) .....	47
Figure 2.9.LabView block program (back interface).....	48
Figure 2.10.OMEGA calibrator .....	49
Figure 2.11.Calibration results.....	50
Figure 2.12.Sample impeller in the pump chamber.....	55
Figure 3.1.ABS samples after 1200 rpm and 5wt.% solid concentration and a wear time 24 hours .....	58
Figure 3.2.Worn surfaces at the end of the blades after different rotational speeds (1200 rpm, 1500 rpm, 1750 rpm), same concentration (5% weight concentration) and wearing time (24 hours) ..	59
Figure 3.3.Pressure sides of the blades after different rotational speeds (1200 rpm, 1500 rpm, 1750 rpm), same concentration (5% weight concentration) and wearing time (24 hours).....	60
Figure 3.4.Suction sides of the blades at different rotational speeds (1200 rpm, 1500 rpm, 1750rpm), same concentration (5% weight concentration) and wearing time (24 hours) .....	60
Figure 3.5.Worn surfaces at the end of the blades after different wearing time (24 and 110hours) at the same rotational speed (1200 rpm) and concentration of solids (5% weight concentration)	61
Figure 3.6.Pressure sides of the blades after different wearing time (24 and 110 hours) at the same rotational speed (1200 rpm) and concentration of solids (5% weight concentration) .....	62
Figure 3.7.Suction sides of the blades after different wearing time (24 and 110hours) at the same rotational speed (1200 rpm) and concentration of solids (5% weight concentration) .....	62

Figure 3.8. Worn surfaces at the end of the blades after different concentrations of solids (5% and 10% weight concentration), same rotational speed (1200 rpm) and wearing time (24 hours) .....	63
Figure 3.9. Pressure sides of the blades after different concentrations of solids (5% and 10% weight concentration), same rotational speed (1200 rpm) and wearing time (24 hours) .....	64
Figure 3.10. Suction sides of the blades after different concentrations of solids (5% and 10% weight concentration), same rotational speed (1200 rpm) and wearing time (24 hours) .....	64
Figure 3.11. Particle degradation .....	65
Figure 3.12. Mass loss vs. wearing time (1200 rpm and 5wt.% solid concentration) .....	66
Figure 3.13. Wear rate vs. flow rate with different concentrations (5wt.% and 10wt.% concentration) .....	68
Figure 3.14. Wear rate vs. concentration with different rotational speeds (1050 rpm and 1200rpm) .....	69
Figure 3.15. Head-flow rate relationship at 850 rpm with carried fluid (water) and different degrees of damage to the impeller .....	70
Figure 3.16. Head-flow rate relationship at 950 rpm with carried fluid (water) and different degrees of damage to the impeller .....	71
Figure 3.17. Head-flow rate relationship at 1050 rpm with carried fluid (water) and different degrees of damage to the impeller .....	71
Figure 3.18. Head-flow rate relationship at 1150 rpm with carried fluid (water) and different degrees of damage to the impeller .....	72
Figure 3.19. Head-flow rate relationship at 1250 rpm with carried fluid (water) and different degrees of damage to the impeller .....	72
Figure 3.20. Head-flow rate relationship at 1350 rpm with carried fluid (water) and different degrees of damage to the impeller .....	73
Figure 3.21. Head-flow rate relationship at 1450 rpm with carried fluid (water) and different degrees of damage to the impeller .....	73
Figure 3.22. Head-flow rate relationship at 1550 rpm with carried fluid (water) and different degrees of damage to the impeller .....	74
Figure 3.23. Head-flow rate relationship at 1650 rpm with carried fluid (water) and different degrees of damage to the impeller .....	74

Figure 3.24.Head-flow rate relationship at 1750 rpm with carried fluid (water) and different degrees of damage to the impeller .....	75
Figure 4.1.Coefficient $C$ after refitting using fixed $A$ and $B$ that varied with different rotational speeds.....	89
Figure 4.2.Head-flow rate relationship at 850 rpm with carried fluid (water) and different damage conditions after refitting using fixed $A$ and $B$ ( $A=-0.0088$ , $B=0.1468$ ).....	90
Figure 4.3.Head-flow rate relationship at 950 rpm with carried fluid (water) and different damage conditions after refitting using fixed $A$ and $B$ ( $A=-0.0089$ , $B=0.1868$ ).....	90
Figure 4.4.Head-flow rate relationship at 1050 rpm with carried fluid (water) and different damage conditions after refitting using fixed $A$ and $B$ ( $A=-0.0062$ , $B=0.1239$ ).....	91
Figure 4.5.Head-flow rate relationship at 1150 rpm with carried fluid (water) and different damage conditions after refitting using fixed $A$ and $B$ ( $A=-0.0036$ , $B=0.0523$ ).....	91
Figure 4.6.Head-flow rate relationship at 1250 rpm with carried fluid (water) and different damage conditions after refitting using fixed $A$ and $B$ ( $A=-0.006$ , $B=0.1317$ ).....	92
Figure 4.7.Head-flow rate relationship at 1350 rpm with carried fluid (water) and different damage conditions after refitting using fixed $A$ and $B$ ( $A=-0.007$ , $B=0.163$ ).....	92
Figure 4.8.Head-flow rate relationship at 1450 rpm with carried fluid (water) and different damage conditions after refitting using fixed $A$ and $B$ ( $A=-0.0015$ , $B=-0.0594$ ) .....	93
Figure 4.9.Head-flow rate relationship at 1550 rpm with carried fluid (water) and different damage conditions after refitting using fixed $A$ and $B$ ( $A=-0.0067$ , $B=0.1359$ ).....	93
Figure 4.10.Head-flow rate relationship at 1650 rpm with carried fluid (water) and different damage conditions after refitting using fixed $A$ and $B$ ( $A=-0.009$ , $B=0.241$ ) .....	94
Figure 4.11.Head-flow rate relationship at 1750 rpm with carried fluid (water) and different damage conditions after refitting using fixed $A$ and $B$ ( $A=-0.0083$ , $B=0.1965$ ) .....	94
Figure 4.12.Coefficient $C$ with the same coefficients $A$ and $B$ ( $A=-0.007$ , $B=0.163$ ) vs. percentage of mass loss.....	97
Figure 4.13.Value $n$ vs. percentage of mass loss .....	98
Figure 4.14.Power vs. flow capacity for different damage conditions (0%, 2.092%, 3.701%, 5.31%, 6.973% and 7.617% mass loss) at 850 rpm with carried fluid (water) ( $A=-0.0088$ , $B=0.1468$ ).....	100

Figure 4.15. Power vs. flow capacity for different damage conditions (0%, 2.092%, 3.701%, 5.31%, 6.973% and 7.617% mass loss) at 950 rpm with carried fluid (water) ( $A=-0.0089$ ,  $B=0.1868$ )..... 100

Figure 4.16. Power vs. flow capacity for different damage conditions (0%, 2.092%, 3.701%, 5.31%, 6.973% and 7.617% mass loss) at 1050 rpm with carried fluid (water) ( $A=-0.0036$ ,  $B=0.0523$ )..... 101

Figure 4.17. Power vs. flow capacity for different damage conditions (0%, 2.092%, 3.701%, 5.31%, 6.973% and 7.617% mass loss) at 1150 rpm with carried fluid (water) ( $A=-0.0036$ ,  $B=0.0523$ )..... 101

Figure 4.18. Power vs. flow capacity for different damage conditions (0%, 2.092%, 3.701%, 5.31%, 6.973% and 7.617% mass loss) at 1250 rpm with carried fluid (water) ( $A=-0.006$ ,  $B=0.1317$ )..... 102

Figure 4.19. Power vs. flow capacity for different damage conditions (0%, 2.092%, 3.701%, 5.31%, 6.973% and 7.617% mass loss) at 1350 rpm with carried fluid (water) ( $A=-0.007$ ,  $B=0.163$ ) ..... 102

Figure 4.20. Power vs. flow capacity for different damage conditions (0%, 2.092%, 3.701%, 5.31%, 6.973% and 7.617% mass loss) at 1450 rpm with carried fluid (water) ( $A=-0.0015$ ,  $B=-0.0594$ )..... 103

Figure 4.21. Power vs. flow capacity for different damage conditions (0%, 2.092%, 3.701%, 5.31%, 6.973% and 7.617% mass loss) at 1550 rpm with carried fluid (water) ( $A=-0.0067$ ,  $B=0.1359$ )..... 103

Figure 4.22. Power vs. flow capacity for different damage conditions (0%, 2.092%, 3.701%, 5.31%, 6.973%, and 7.617% mass loss) at 1650 rpm with carried fluid (water) ( $A=-0.009$ ,  $B=0.241$ ) ..... 104

Figure 4.23. Power vs. flow capacity for different damage conditions (0%, 2.092%, 3.701%, 5.31%, 6.973%, and 7.617% mass loss) at 1750 rpm with carried fluid (water) ( $A=-0.0083$ ,  $B=0.1965$ )..... 105

Figure 4.24. Power for a certain flow rate vs. percentage of mass loss for different rotational speeds (850 rpm, 950 rpm, 1050 rpm, 1150 rpm, 1250 rpm, 1350 rpm, 1450 rpm, 1550 rpm, 1650rpm and 1750 rpm)..... 106

A.1.Head-flow capacity relationship at 850 rpm & 5wt.% concentration after 24 hours 1500rpm wearing.....	128
A.2.Head-flow capacity relationship at 950 rpm & 5wt.% concentration after 24 hours 1500rpm wearing.....	128
A.3.Head-flow capacity relationship at 1050 rpm & 5wt.% concentration after 24 hours 1500rpm wearing.....	129
A.4.Head-flow capacity relationship at 1150 rpm & 5wt.% concentration after 24 hours 1500rpm wearing.....	129
A.5.Head-flow capacity relationship at 1250 rpm & 5wt.% concentration after 24 hours 1500rpm wearing.....	130
A.6.Head-flow capacity relationship at 1350 rpm & 5wt.% concentration after 24 hours 1500rpm wearing.....	130
A.7.Head-flow capacity relationship at 1450 rpm & 5wt.% concentration after 24 hours 1500rpm wearing.....	131
A.8.Head-flow capacity relationship at 1550 rpm and 5wt.% concentration after 24 hours 1500rpm wearing .....	131
A.9.Head-flow capacity relationship at 1650 rpm & 5wt.% concentration after 24 hours 1500rpm wearing.....	132
A.10.Head-flow capacity relationship at 1750 rpm & 5wt.% concentration after 24 hours 1500rpm wearing .....	132
A.11.Head-flow capacity relationship at 850 rpm & 5wt.% concentration after 24 hours 1750rpm wearing.....	133
A.12.Head-flow capacity relationship at 950 rpm & 5wt.% concentration after 24 hours 1750rpm wearing.....	133
A.13.Head-flow capacity relationship at 1050 rpm & 5wt.% concentration after 24 hours 1750rpm wearing .....	134
A.14.Head-flow capacity relationship at 1150 rpm & 5wt.% concentration after 24 hours 1750rpm wearing .....	134
A.15.Head-flow capacity relationship at 1250 rpm & 5wt.% concentration after 24 hours 1750rpm wearing .....	135

A.16.Head-flow capacity relationship at 1350 rpm & 5wt.% concentration after 24 hours 1750rpm wearing .....	135
A.17.Head-flow capacity relationship at 1450 rpm & 5wt.% concentration after 24 hours 1750rpm wearing .....	136
A.18.Head-flow capacity relationship at 1550 rpm & 5wt.% concentration after 24 hours 1750rpm wearing .....	136
A.19.Head-flow capacity relationship at 1650 rpm & 5wt.% concentration after 24 hours 1750rpm wearing .....	137
A.20.Head-flow capacity relationship at 1750 rpm & 5wt.% concentration after 24 hours 1750rpm wearing .....	137
A.21.NI-DAQmx interface of scaling of pressure transducer .....	143
A.22.Interface of setting data acquisition system .....	144
A.23.Flow rate, temperature and head vs. time in the experiments for 1200 rpm and 5wt.% solids concentration, part 1.....	149
A.24.Flow rate, temperature and head vs. time in the experiments for 1200 rpm and 5wt.% solids concentration, part 2.....	150
A.25.Flow rate, temperature and head vs. time in the experiments for 1200 rpm and 5wt.% solids concentration, part 3.....	151
A.26.Flow rate, temperature and head vs. time in the experiments for 1500 rpm and 5wt.% solids concentration, part 1.....	152
A.27.Flow rate, temperature and head vs. time in the experiments for 1500 rpm and 5wt.% solids concentration, part 2.....	153
A.28.Flow rate, temperature and head vs. time in the experiments for 1500 rpm and 5wt.% solids concentration, part 3.....	154
A.29.Flow rate, temperature and head vs. time in the experiments for 1750 rpm and 5wt.% solids concentration, part 1.....	155
A.30.Flow rate, temperature and head vs. time in the experiments for 1750 rpm and 5wt.% solids concentration, part 2.....	156
A.31.Flow rate, temperature and head vs. time in the experiments for 1750 rpm and 5wt.% solids concentration, part 3.....	157

A.32.Flow rate, temperature and head vs. time in the experiments for 1750 rpm and 5wt.% solids concentration, part 4.....	158
A.33.Flow rate, temperature and head vs. time in the experiments for 1200 rpm and 15wt.% solids concentration, part 1.....	159
A.34.Flow rate, temperature and head vs. time in the experiments for 1200 rpm and 15wt.% solids concentration, part 2.....	160
A.35.Flow rate, temperature and head vs. time in the experiments for 1050 rpm and 5wt.% solids concentration, part 1.....	161
A.36.Flow rate, temperature and head vs. time in the experiments for 1050 rpm and 5wt.% solids concentration, part 2.....	162
A.37.Flow rate, temperature and head vs. time in the experiments for 1050 rpm and 10wt.% solids concentration, part 1.....	163
A.38.Flow rate, temperature and head vs. time in the experiments for 1050 rpm and 10wt.% solids concentration, part 2.....	164
A.39.Flow rate, temperature and head vs. time in the experiments for 1050 rpm and 15wt.% solids concentration, part 1.....	165
A.40.Flow rate, temperature and head vs. time in the experiments for 1050 rpm and 15wt.% solids concentration, part 2.....	166



# Nomenclature

$\rho_s$	Solids density
$C_s$	Particle concentration
$V_s$	Velocity of the particle
$E_I$	Impact wear coefficient
$\alpha$	Impact angle
$E_0$	Coefficient when the particle is normal impact
$E_w$	Wear rate
$V$	Flow velocity
$d$	Particle size
$C_w$	Concentration of the slurry
$E_{w \text{ brass}}$	Brass wear rate
$E_{w \text{ mild steel}}$	Mild steel wear rate
$C_v$	Volume concentration of the slurry
$\alpha_1$	The impact angle at where wear develops
$n$	Function related $H_1/H_2$
$H_1$	Hardness of eroded materials

$H_2$	Hardness of solid particles
$\Delta W$	Wear rate
$\rho_k$	Density of k species
$C_k$	Concentration of k species
$V_k$	Velocity of k species
$E_{Ik}$	Impact wear coefficient of k species
$\dot{W}_{SL}$	Sliding wear rate
$\tau_s$	Solids shear stress
$u_{St}$	Solids tangential velocity
$E_{SL}$	Sliding wear coefficient
$\tau_k$	Shear stress of k species
$u_k$	Solids tangential velocity of k species
$u_{\tau k}$	Friction velocity
$d_{pk}$	Particle diameter of k species
$\alpha_k$	Impact of k species
$E_{SP}$	Coefficient of sliding wear rate
$d_s$	Particle diameter

$c_N$	Solids concentration
$H_M$	Hardness of materials
$V_{loss}$	Volume loss material due to abrasion
$I$	Current
$P$	Pressure
$H_{total}$	Total dynamic head
$V_A$	Velocity at suction side
$V_B$	Velocity at discharge side
$P_A$	Pressure at suction side
$P_B$	Pressure at discharge side
$\rho_f$	Density of liquid
$g$	Gravity acceleration
$Z_A$	Elevation of the reference level at suction side
$Z_B$	Elevation of the reference level at the discharge side
$P_{out}$	Output power
$Q$	Flow capacity
$H$	Total dynamic head of the head

$\omega$	Angular velocity
$n$	Rotational speed measured in revolution per second
$N$	Rotational speed measured in revolution per minute
$P_{in}$	Input power
$T$	Torque of the shaft
$\eta$	Efficiency of the pump
$t$	Wear time
$M_L$	Impeller weight left
$E$	Wear rate
$C$	Weight concentration
$C_D$	Drag coefficient
$\rho_a$	Density of the air
$r$	Particle radius
$\rho_p$	Particle density
$Q_{volume}$	Volume loss
$m_p$	Mass of the single particle
$V_p$	Velocity of the particle

$p$	Constant plastic flow stress
$\varphi$	Ratio of depth of particle contact the surface and depth of cut
$\alpha_p$	Angle of particles striking the surfaces
$E(\alpha_p)$	Erosion damage at arbitrary angles
$E_{90}$	Erosion damage at normal angle
$Hv$	Initial material hardness
$D$	Particle diameter
$R_f$	Particle roundness factor
$\sigma$	Material flow stress
$P$	Fluid power
$w$	Rotational speed
$M_{percent}$	Mass loss percentage
$A$	Coefficient in the parabola fitting of head and flow capacity relationship
$B$	Coefficient in the parabola fitting of head and flow capacity relationship
$C$	Coefficient in the parabola fitting of head and flow capacity relationship

# 1. Introduction

## 1.1 Background

### 1.1.1 Slurry pumps

Slurry pumps play a key role in fluid transportation. They are widely used in mining, dredging and power generation. Pumps can carry fluids such as liquid, gas and slurries. The flow in a pump is very complex and difficult to simulate, especially for a solid-liquid two-phase flow. Thus, the mathematical models and methods to define the flow in a pump are under investigation (Majidi, 2004). Two wet components in a pump, volute and impeller, intimately affect the pump performance and the wear of a pump: the volute and the impeller. For this reason, both the volute and the impeller are the most frequently replaced parts in industry.

A slurry pump, a type of the centrifugal pump, is specifically used to transport slurries. The slurry pump undergoes the most wear in harsh conditions. Slurry pumps are categorized based on the size, hardness, concentration and the velocity of solids that they can handle (Lobanoff & Ross, 1992). They can be classified based on solids size, as in Table 1.1. Slurry pumps are designed for their wear resistance at the cost of losing efficiency, which explains why slurry pumps often have low efficiency.

Recessed impeller pumps, also called vortex impeller pumps, are classified as centrifugal slurry pumps. As the name implies, the semi-open impeller is placed in the back of the pump casing. Vortex pumps are often used to handle the solids in the liquid. The recessed impeller pumps are special centrifugal pumps; it does not shovel the liquid and is located outside the volute. There are two stages to the vortex pump's pumping process. The impeller produces a primary vortex or

whirlpool in the liquid around the impeller itself, and this vortex creates another vortex in the volute that moves the flow (Evans, 2015). Figure 1.1 shows the typical structure of vortex impeller pumps. Due to the pumping mechanism of the recessed impeller pump, the impeller has minimal contact with the solid particle in the fluid and potential erosion is significantly reduced. The large clearance between the impeller and the volute allows large solids to pass and prevents clogging. Because of the constitution of the vortex impeller, the radial forces that act on the impeller are reduced, which explains why many vortex pumps can be operated at low flow rates, or even at shut off, for an extended period without damage (Evans, 2015). Thus, the recessed impeller pump is suitable for handling slurries, sludge or other liquids with large solids. Although the recessed impeller pump is often criticized for its low hydraulic efficiency, it is still superior at transporting solid-liquid phase flow. Therefore, vortex impeller pumps are popular in situations that requires high reliability and reasonable cost, but are useful in cases when there is a need for high efficiency.

Table 1.1. Slurry pump classification

Pump name	Slurry pump	Sand pump	Sand & Gravel pump	Dredge pump
Particle size	0.002mm-0.6mm	0.7mm-1.7mm	1.9mm-22.7mm	38.1mm-4060mm

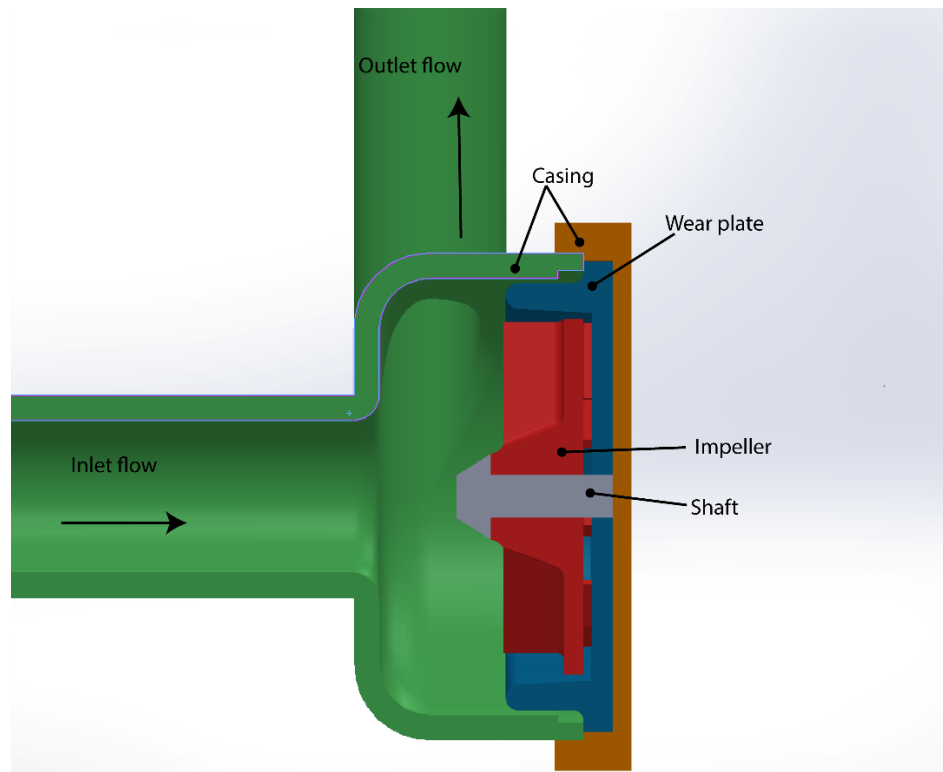


Figure 1.1. Recessed impeller pump

### 1.1.2 Abrasive wear in the pump

Abrasive wear, which is a common problem in slurry pumps, is a primary objective of this thesis. Wear is a process of removing material and leading to deformation on the target surface. It can be divided into two categories: mechanical and chemical. Abrasive wear results in a change in shape from the original design shape of an impeller. This, in turn, will result in the energy waste and poor pump performance, which leads to further problem such as the maintenance fees, cost of the components replacement and the loss due to interruption of the projects. For example, based on the GIW industries Inc's report in 2012 (GIW Industries Inc., 2012), in mining industries, which cost \$150,000 every hour. It took 10 hours to replace the slurry pump. This kind of replacement occurred eight times per year (GIW Industries Inc., 2012). Study on abrasive wear in a pump is



helpful for engineers to know the life of the wet components in advance and avoid operational failure when running the pump. Also, investigating the abrasive wear problem can give guidance when designing and optimizing pumps to save energy and cost. In slurry pumps, wet-end parts such as pump casing, impeller and other wet-end parts are mostly worn abrasively. Among the wet-end parts in the slurry pumps, the suction liner has the shortest life, and the casing has the longest life.

Roco et al. (1987) listed three types of abrasive wear that affects slurry pumps and pipelines: directional impact, random impact and friction. Different interaction between particles and wall cause different types of abrasive wear. When a pump transports a gas-liquid two-phase flow, the cavitation in the pump is one of the primary factors affecting the wear behavior. In the field of studying the wear caused by the solid-liquid two phase flow, many parameters may influence the abrasive wear behavior. These parameters are shown in Figure 1.2, which includes the chemical factors that affect total wear. Intensive investigations of abrasive wear will be presented in Section 1.3.

Two methods are used to examine abrasive wear in a laboratory: computer-aided simulation and empirical studies using either laboratory or industrial operation. Simulation using computational fluid dynamics (CFD) has the advantages of saving both money and time, but the disadvantage is that the models now used cannot accurately describe the multiphase flow motion in the pump due to the complexity of the flow.

The known laboratory apparatus used in most research are: impingement jet wear testers (Yoganandh, et al., 2012), Coriolis wear testers (Tuzson, 1984), pot wear testers (Clark, et al. 1995; 2001; 2002), Toroid wear testers (Worster et al., 1955) and pin-on-disc sliding wear testers (Janssen, et al., 2017). These testers simulate the situation of different abrasive wear to study the

different parameters that may affect the wear behavior (detailed information will be shown in Section 1.3). Other studies used the data from the industries in the actual operation, which may be more realistic, but it is time-consuming and expensive. Few investigations about pump wear exits that use a laboratory pipe loop. Time limitation and cost are why few investigators have conducted experiments on an actual production platform. An effective laboratory-scale method need to be developed, one with a lower cost, high efficiency and high accuracy is needed.

In previous investigations of wear in pumps, the wet-end parts in the pump have been taken into consideration. These parts include the pump casing, impeller, wear plate and sideliners. The wet-end parts vary based on the different types of pumps. In this work, we primarily investigated the wear on the impellers.

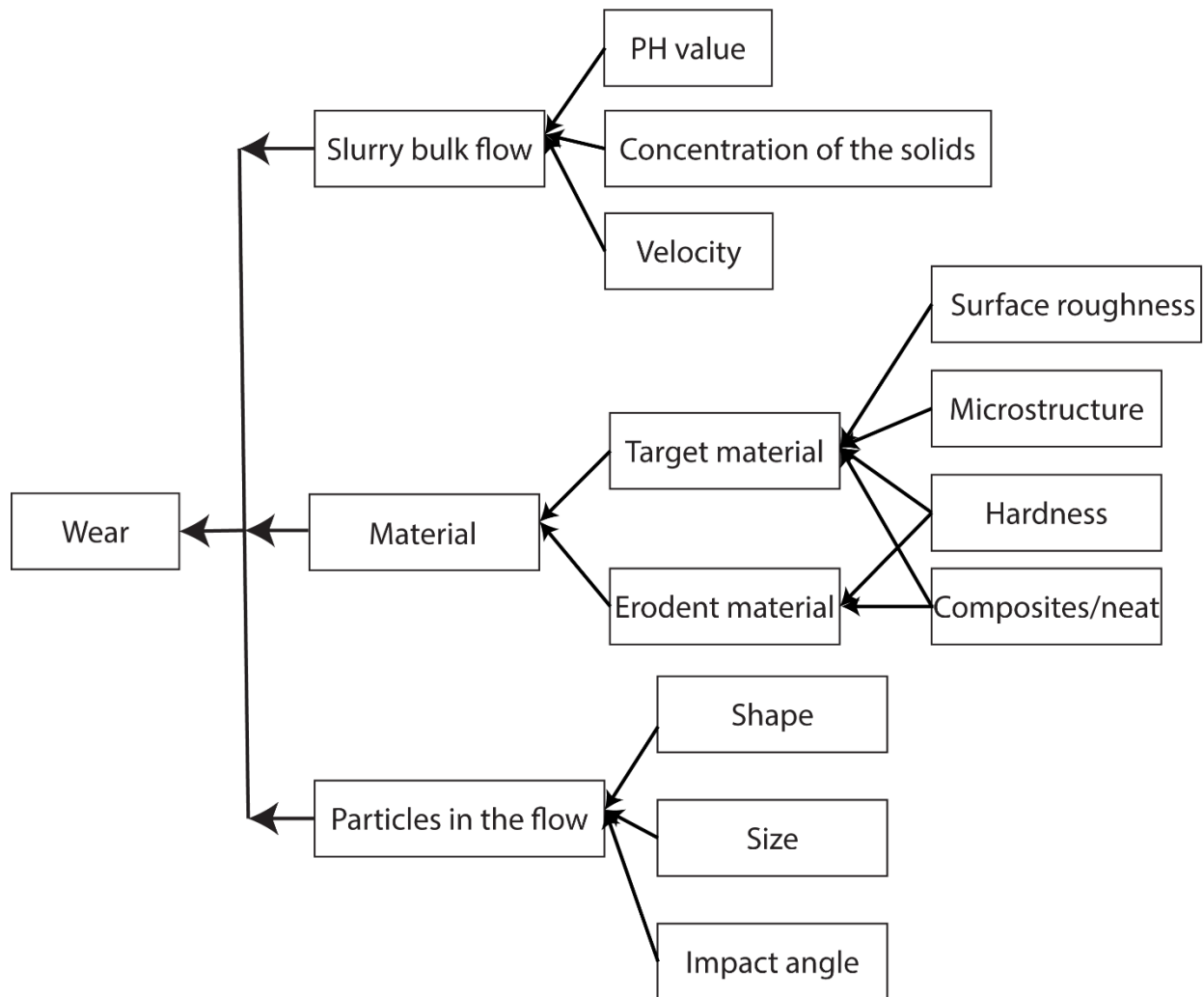


Figure 1.2. Parameters that affect the wear behavior (solid-liquid two-phase flow)

## 1.2 Literature review

### 1.2.1 Flow model in the centrifugal pumps

The flow motion inside of a pump chamber is complex and interesting to investigate. Secondary flow will often happen in the slurry vortex pump. Westra et al. (2010) observed and simulated the secondary flow around the shrouded centrifugal pump impeller. The secondary flow effects resulted in a jet wake structure near the shroud at the suction side. Also, the wake region

increased as the flow rate increased. It seems that the jet-wake flow was frequently observed inside of the chamber. Zhang et al. (2013) found that the jet-wake flow was observed at the volute tongue and became more apparent when the solid concentration was increasing. Zhang et al. also claimed that the impeller takes more abrasion than other parts in a pump. Kadambi et al. (2004) used Particle Image Velocimetry (PIV) technology to investigate flow in a pump. They found that the highest velocity of the particles is on the suction side and the trailing edge of the blades, but the velocity of the particle in these regions is still smaller than the circumferential velocity at the tip of the blades. Also, kinetic energy plays a role in abrasion. Kadambi et al. (2004) found that the maximum fluctuated kinetic energy appears on the suction side. The pressure side of the blades, tongue and casing of the slurry pump have more directional impingement, which means that these regions have a greater likelihood of wear (Kadambi, 2004). Random impingement occurs on both sides of the blades and casing, while frictional wear occurs on the pressure sides of the blades (Kadambi, 2004). Gupta et al. (2011) simulated the two-phase flow in the centrifugal pump and found that the location with the maximum kinetic energy is at the trailing edge of the blade, and that this region has the highest total pressure.

In general, the numerical computation with CFD is the best and most efficient way to investigate the flow model in a pump. The particle movement, especially the velocity angle of the solid when hitting the blades, is one of the most concerning issues that will affect abrasive wear in a slurry pump.

### **1.2.2 Wear model**

Based on the different particle motions for example the impingement angle, the abrasive wear rate is divided into two parts: the impact wear rate and the sliding wear rate. However, it is

not clear what proportion of these two kinds of abrasive wear occurs in pumps and few articles address it. Due to the complexity of the flow model in slurry pumps, random wear is the main wear behavior. Some researchers have investigated the impact wear and sliding wear separately, and some have proposed empirical correlations based on different factors that affect abrasive wear. Three factors affect wear behavior: the properties of carried flow, particles and target materials. The bulk flow rate, the solids concentration of the flow, density, viscosity and particle size distribution. are often discussed when discussing the properties of the carried flow. For particles in the slurry flow, the shape, hardness of the solid, velocity and impingement angles of the particles are often considered to be properties of the particles. Hardness and the roughness of the target surface are discussed in relation to the properties of target materials. Detailed information about factors affect abrasion will be presented in the following sections. For the wear in the pump specifically, the geometry of the components and the structure of the pumps should also be taken into consideration. The wear math models in this section did not consider the geometry of the target trial parts.

For single size slurries, the impact wear rate is related to the kinetic energy flux of the particles (Roco, et al., 1984):

$$\dot{W}_I = \frac{\rho_s C_s V_s^3}{E_I(\alpha)} \quad (1.1)$$

Where  $\rho_s$  is the solids density,  $C_s$  is the particle concentration,  $V_s$  is the velocity of the particle,  $E_I(\alpha)$  is the impact wear coefficient. For different impeller materials, the exponent of the  $V_s$  will be varied. The impact wear coefficient  $E_I$  is correlated with the impact angle  $\alpha$ . For a Ni-hard (a white iron alloy) material, the coefficient can be given as:

$$E_I(\alpha) = \frac{E_0}{\frac{4\alpha}{\pi} \left(1 - \frac{\alpha}{\pi}\right)} \quad (1.2)$$

Where  $E_0$  is the coefficient when the particle is the normal impact with wall,  $\alpha$  is the impact angle.  $E_0$  depends on the particle size and materials. Thus, different materials have different wear coefficients, which need to be determined by the experiments.

Gupta et al. (1995) had a math model for wear rate, which is given as:

$$E_w = KV^\alpha d^\beta C_w^\gamma \quad (1.3)$$

Where  $K$ ,  $\alpha$ ,  $\beta$ ,  $\gamma$  are the parameters determined by the different properties of the materials of solid particles and the target surface.  $V$  is the flow velocity,  $d$  is the particle size,  $C_w$  is the concentration of the slurry.

According to Equation 1.3, the flow velocity, particle size, and concentration have power relationship with the wear rate. Gupta et al. also obtained two specific equations for brass and mild steel. The equations are:

$$E_{w \text{ brass}} = 0.178V^{2.4882} d^{0.291} C_w^{0.516} \quad (1.4)$$

$$E_{w \text{ mild steel}} = 0.223V^{2.148} d^{0.344} C_w^{0.556} \quad (1.5)$$

Elkholy (1983) set up a study at a jet abrasion tester to determine the best material in a pump. An analytical model was proposed to predict the wear for hard and brittle materials under different operation conditions:

$$\Delta W = \frac{1}{2} K C_v^{0.682} \left(\frac{H_1}{H_2}\right)^n d^{0.616} V^{2.39} \left\{1 + \sin\left(\frac{\alpha - \alpha_l}{90 - \alpha_l} 180 - 90\right)\right\} f(t) \quad (1.6)$$

Where  $H_1$  (HB) is the hardness of eroded material,  $H_2$  (HB) is the hardness of solid particles,  $C_v$  is the volume concentration of the slurry,  $d$  is the particle size,  $K$  is the constant,  $V$  is the velocity of the particles,  $\alpha$  is the impingement angle,  $\alpha_l$  is the angle at which the wear develops,  $n$  is a function of  $H_1/H_2$  according to

$$n=3.817 \text{ if } \frac{H_1}{H_2} < 1.9$$

$$n=0.268 \text{ if } \frac{H_1}{H_2} > 1.9$$

$f(t)$  is a linear function from Brauer and Kriegel (1963).

For Elkholy's experiment on cast iron which used as hard and brittle materials, the final equation can be rewritten as:

$$\Delta W = 1.342 \times 10^{-5} C_v^{0.682} \left( \frac{H_1}{H_2} \right)^n d^{0.616} V^{2.39} \left\{ 1 + \sin \left( \frac{\alpha - \alpha_l}{90 - \alpha_l} 180 - 90 \right) \right\} T \quad (1.7)$$

Although Elkholy tested aluminum which used as ductile materials, the exact equation for aluminum did not show in the end.

Ravichandra (2004) developed an impact wear rate expression for multi-sized slurries. The wear rate is related to the size distribution of the slurry, which means that all the sizes of the particle need to be taken into consideration. The expression of the wear rate is given as:

$$\dot{W}_I = \sum_{k=1}^N \frac{\rho_k C_k V_k^3}{E_{Ik}(\alpha_k)} \quad (1.8)$$

Where  $\rho_k$  is the density of  $k$  species,  $C_k$  is the concentration of  $k$  species,  $V_k$  is the velocity of  $k$  species,  $E_{Ik}$  is the wear coefficient of  $k$  species.

It should be noted that the impact wear rate should be treated differently in different situations.

Sliding wear is often related to the friction of the particles. The sliding wear is given as:

$$W_{SL} = \frac{\tau_s u_{St}}{E_{SL}} \quad (1.9)$$

Where  $\tau_s$  and  $u_{St}$  are the solid shear stress and solid tangential velocity respectively,  $E_{SL}$  is the sliding wear coefficient.

From Equation 1.9, the sliding wear rate is related to the solid shear stress and the solid tangential velocity. For multi-sized slurry flow is:

$$W_{SL} = \sum_{k=1}^N \frac{C_k \tau_k u_k}{E_{SP}(d_{Pk})} \quad (1.10)$$

$$\tau_k = \rho_k u_{\tau k}^2 \quad (1.11)$$

Where  $C_k$ ,  $\tau_k$  and  $u_k$  are the concentration, shear stress and solid tangential velocity of  $k$  species respectively,  $u_{\tau k}$  is the friction velocity.

Visintainer, et al. (2005) defined the wear rate coefficient as:

$$E_{Ik}(\alpha_k, d_{pk}) = C_{adj} E_I(\alpha_k) \quad (1.12)$$

$C_{adj}$  is a factor that can be calculated by (1.12):

$$C_{adj} = A_{im} [1.65 d_{pk} + C_{im}]^{n_{im}} + B_{im} \quad (1.13)$$

Where  $A_{im}$ ,  $C_{im}$ ,  $B_{im}$  and  $n_{im}$  are the constant and can be determined by experiments.



Visintainer, et al. (2005) determined the value for specific Ni-Cr white iron alloy and sand particles, which are:

$$A_{im} = 8.578 \times 10^{10},$$

$$B_{im} = 3.645 \times 10^{-2},$$

$$C_{im} = 490,$$

$$n_{im} = -3.668,$$

Pagalthivarthi et al. (1992), Tuzson et al. (1984) and Clark et al. (2000) used a Coriolis test rig to determine the sliding wear coefficient:

$$E_{SP}(d_{pk}) = 10^8 [A_{sl}(d_{pk} + C_{sl})^{n_{sl}} + B_{sl}] \quad (1.14)$$

Where  $A_{sl}$ ,  $B_{sl}$ ,  $C_{sl}$  and  $n_{sl}$  are the constant determined by experiments.

These empirical constants for white iron alloy material are as following (Pagalthivarthi, 2009):

$$A_{sl} = 4.236 \times 10^{14},$$

$$B_{sl} = 180,$$

$$C_{sl} = 490,$$

$$n_{sl} = -3.861.$$

The total wear rate is the sum of the impact wear rate and sliding wear rate.

Batalovic (2010) came up with a simpler wear model based on the Monte Carlo method (Soboli, 1998) and other numerical analyses and experiments:

$$E(t) = KV(Y_i) \quad (1.15)$$

$V(Y_i)=V(Y_1, Y_2, Y_3)$  is the loss of volume-mass material due to abrasion.

$$V_{loss} = K[d_s^3 c_N^2 \left(\frac{\rho_s}{H_M}\right)^{\frac{3}{2}}] \quad (1.16)$$

Where  $K$  is a coefficient,  $d_s$  is the particle diameter,  $c_N$  is the concentration,  $\rho_s$  is the density of solids and  $H_M$  is the hardness of material.

Equation 1.16 shows that erosion loss is mostly affected by the transported solids, materials of the impeller and characteristics of the slurry flow.

Finnie (1960) considered material loss from a microscopic perspective. The volume loss of the target surface was given by:

If  $\tan \alpha_p \leq \frac{K}{6}$ , then

$$Q_{volume} = \frac{m_p V_p^2}{p\phi K} (\sin 2\alpha_p - \frac{6}{K} (\sin \alpha_p)^2) \quad (1.17)$$

If  $\tan \alpha_p \geq \frac{K}{6}$ , then

$$Q_{volume} = \frac{m_p V_p^2}{p\phi K} \left(\frac{K (\cos \alpha_p)^2}{6}\right) \quad (1.18)$$

Where  $Q_{volume}$  is the volume loss of material removed by a single abrasive particle,  $m_p$  is the mass of the single particle,  $V_p$  is the velocity of the particle,  $p$  is the constant plastic flow stress when the particle reached wall immediately upon impact,  $\phi$  is ratio of depth of particle contact the surface and the depth of the cut,  $\alpha_p$  is the angle of the particles striking the surfaces, and  $K$  is the constant defined by

$$K = \frac{3C_D\rho_a}{8r\rho_p} \quad (1.19)$$

Where  $C_D$  is the drag coefficient,  $\rho_a$  is the density of the air (in Finnie's study, air is the carried fluid),  $r$  is the particle radius, and  $\rho_p$  is the particle density.

Oka et al. (2005) also estimated the erosion damage due to the particle impact from the microscopic view. They assume that the parameters that related to the erosion damage include the impact velocity, angle, size and properties of the particle and hardness of the target materials. Among these parameters, the impact angle and harness are regarded as the most significant.

$$E(\alpha_p) = g(\alpha_p)E_{90} \quad (1.20)$$

Where  $E(\alpha_p)$  is the erosion damage at arbitrary angles,  $g(\alpha_p)$  is a function related to the hardness and impact angle,  $E_{90}$  is the erosion damage at the normal angle and  $\alpha_p$  is the impact angle.

$$g(\alpha_p) = (\sin \alpha_p)^{n_1} (1 + Hv(1 - \sin \alpha_p))^{n_2} \quad (1.21)$$

Where  $Hv$  is the initial material hardness,  $n_1$  and  $n_2$  are determined by the material hardness and other impact conditions including the particle properties.

$$E_{90} = K(Hv)^a v^b D^c \quad (1.22)$$

Where  $a$ ,  $b$  and  $c$  depend on other parameters and  $D$  is the particle diameter.

Hashish (1987) improved Finnie's model which is more suitable for the shallow impact angle, which is:

$$Q_{volume} = \frac{7}{\pi} \frac{m_p}{\rho_p} \left(\frac{V_p}{C_K}\right)^{2.5} \sin 2\alpha \sqrt{\sin \alpha} \quad (1.23)$$

Where  $C_K$  was defined as:

$$C_K = \sqrt{\frac{3\sigma R_f^{3/5}}{\rho_p}} \quad (1.24)$$

Where  $R_f$  is the particle roundness factor dependence of the average diameter of particle corners to the diameter of a maximum inscribed circle,  $\sigma$  is the material flow stress.

Based on the wear models proposed from the previous literature, it should be noted that the wear models can be seen from two perspectives: macroscope (flow) and microscope (particle). For the bulk flow, the following factors are often considered:

- Solids concentration
- Flow rate
- Density of the slurry flow
- Particle size distribution

For the particles, the following factors are often considered:

- Impact angle
- Particle shape
- Particle size
- Impact velocity
- Mass of the particle

The hardness of the particle material and target surface material should both be considered from these two perspectives.

### **1.2.3 Abrasive wear mechanism**

Roco (1987) first described the wear mechanism as a directional impact (gauging and fracture), random impact (fatigue cracking) and friction (sliding and rolling). Meng and Ludema (1994) separated the wear mechanism into cutting, fatigue and brittle fracture for mechanical wear, and chemical dissolution and reaction with a substrate for chemical corrosion and thermal actions like melting. Xing et al. (2009) came up with a process of wear in the pump, which is defined as having three stages: saturation, steady and sharp wear. Bitter (1962) and Arnell (1993) devised two ways of evaluating erosion wear: cutting and deformation. Arnell et al. (1993) attributed cutting wear to a low angle impingement of the particle and deformation to a high angle impingement. For abrasive wear mainly in the slurry pumps, when the pump is operated at a low speed, the solid particles have a strong chance to form pits and micro-cracking. Increasing the rotational speed will cause sliding wear and more material removal (Dasgupta et al., 1997).

### **1.2.4 Properties of erodent affecting abrasive wear behavior**

Impingement particles have two parameters (shape and size of the particles) which will affect the wear action. Arbnejad et al. (2015) validated the semi-mechanism erosion equation that related particle shape and size with direct impingement testing. Chandel et al. (2012) performed a series of experiments on brass and mild steel specimens with fly ash and a mix of fly ash and bottom ash to investigate the effect of particle size, solid concentration and rotational speed. They found that when the particle size was increased fivefold, the wear increased by 300% on brass and

350% on mild steel specimens at 600 rpm. Zhong et al. (1996) investigated the erodent on pump casing, and they found that an increased particle diameter would result in a greater erosion rate, but when the diameter was less than 1mm, the influence of solids' diameter was trifling. Shen et al. (2016) had results similar to those of Zhong. They found that the volume concentration had a more significant influence on wear behavior when the particle was larger than 1mm. Nguyen et al. (2016) studied the detailed effect of particle size on the erosion rate, erosion mechanism, and erosion pattern. They observed that the wear rate increased gradually until the particle reached 150um, and then it decreased as the particle grew. Xing (2009) used sphere coal as the erodent in a simulation experiment and found that the distortion degree and maximum Von Mises stress, also indicators of wear, increased as the diameter of the coal increased and the particle velocity rose. There was an opposite trend in the taper angle of the coal particles. Tian et al. (2005) studied narrow, semi-narrow and wide-banded particle size distribution to find the best situation to use a *D50* particle size to calculate the actual abrasion of slurry. Among these three size distributions, the *D50* works well when the size distribution is wide.

The properties of bulk flow will also influence wear behavior. Li (2011) showed that the impact of solid particles is not evident until the particle volume concentration is over 2.5%. Li also found that the weight loss is 12.9% when the volume concentration is over 10%. Chandel et al. (2012) increased the weight concentration of fly ash slurry from 20% to 65%, which resulted in wear on brass 65% increase and mild steel 62% increase at 600 rpm. The local solid concentration near the pressure side can be increased by increasing the rotational speed, which will cause more significant and damaging wear (Pagalthivarathi et al. 2009). Also, increasing the Reynolds number and the concentration will increase the wear rate (Pagalthivarathi et al. 2009). The wear is severe when the velocity of the bulk flow is low, which means that the wear rate can be decreased when

the slurry pump is operated in a high-efficiency state (Peng et al. 2015). Ni-hard material, as a commonly used metal in the pump, was studied by Yoganandh et al. (2012), who changed the parameters such as velocity, impact angle and pH in three different conditions. Yoganandh et al. found that velocity is a dominant factor affecting the erosion rate, and that maximum erosion occurs when the angle of impingement is 60°.

### **1.2.5 Wear location on the impeller**

Detecting the location of the most wear is useful for engineers who are designing the pump, as it will help them determine where to reinforce and optimize. Mehta et al. (2007) detected the flow pattern using Particle Image Velocimetry (PIV) and found that the suction side of the blade often has maximum fluctuation kinetic energy and also random impingement wear. The pressure side often has frictional wear. Xing (2009) indicated that the main wear locations on the impeller are the blade outlet, inlet and middle, and intersection of the inlet vane and hub, and the rear cover plate. Zhang et al. (2013) used CFD to simulate the particle distribution on the impeller and found that the suction side of the blades and the trailing edge of the pressure side undergoes more abrasion, and that both blades suffer severe abrasion when the solid concentration is more than 12%. Liu et al. (2012) used Fluent software and distributive rules of particulate to study the abrasion of a sewage pump. They concluded that large solids settle in the front of the vane near the impeller hub and the middle of impeller passage, and the fine solids often aggregate in the region near the cover and the middle of impeller passage. Zhang et al. (2016) used OpenFoam as a CFD tool to show that the wear locations are on the suction side near the hub and the trailing edge of the pressure side. A test rig was created to study the distribution of the wear pattern in the impeller (Khalid & Sapuan, 2014). Li et al. (2011) also showed that the hub of the impeller had the most wear impact due to maximum shear stress. Wilson and Hawk (1999) developed a test rig

called impeller-in-drum to simulate wear in the impeller. They found that the most damage occurred in the region of the blade tip. Kruger et al. (2010) used CFD simulation and experiments and found that a shock-like wear pattern occurred along the leading edge of the impeller blade mostly due to the particle impingement angle and solid concentration. Kruger et al. also found that a friction-like wear pattern occurred at the trailing edge, tip clearance and side plate. Figure 1.3 shows common sites of abrasive wear.

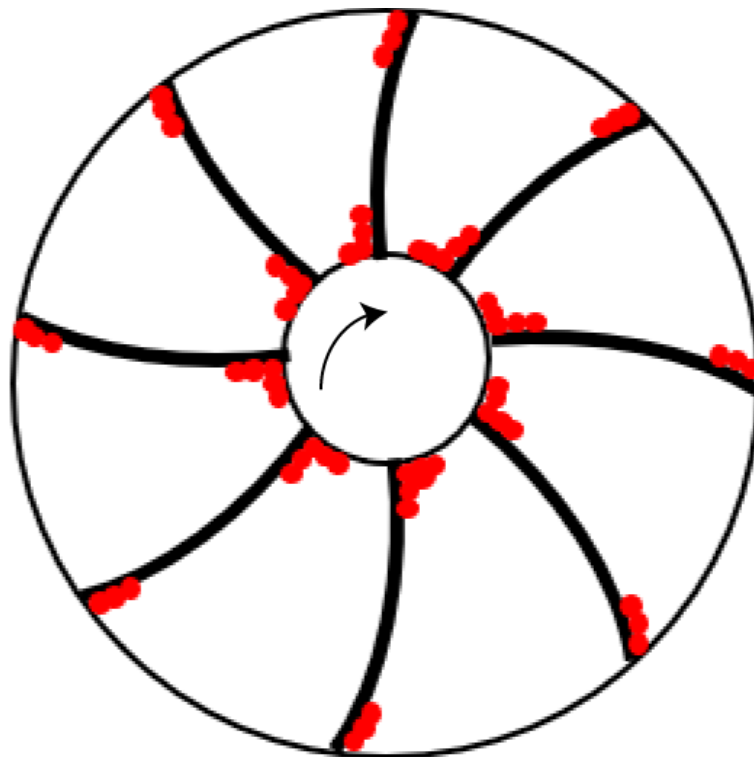


Figure 1.3. Typical sites of abrasive wear (red marks)

### **1.2.6 Wear locations on other wet-end parts in the slurry pumps**

Other wet-end components also experience abrasion. Apart from the impeller blades, Noon et al. (2016) found that the maximum velocity occurs near the tongue and belly regions of volute casing, especially near the discharge regions. Zhong et al. (1996) found a similar wear region in



pump casing. They also found that when the particle size was increased to 3mm, the wear rate doubled in whole volute casing except for the tongue region. Pagalthivartha et al. (2011) investigated the effect of various geometries of pump casing. They also used wall shear stress as an indicator to show wear behavior in the bell region and tongue, where abrasion is severe. Gandhi et al. (2001) identified that the area near the discharge side had the most erosion probably because an eddy appeared and increased the turbulence effect at the volute throat.

In conclusion, impeller and pump casing have the most abrasion. Other components such as sideliners and the wear plate are designed to protect these two significant parts. Thus, the cost for wear plates or linings is relatively low compared to the cost for volute casing and impellers.

### **1.2.7 Wear behavior of typical materials applied in the pump**

Metal materials like alloy are often the first choice to be used as wear-resistant materials. These materials have the potential to be applied in an impeller, which can prolong pump life. Lindgren et al. (2015) tested five different kinds of stainless steel on a small-scale reactor using samples on the impeller blades. Their results show that duplex grades LDX 2101 and 2507 had a better erosion resistance compared to austenitic grades 316L, 904L and duplex grade 2205. Shukla et al. (2015) simulated the performance of four different materials (copper alloy, bronze, stainless steel and titanium alloy) on the blades of the mixed flow pump using ANSYS 11.0. They found that titanium alloy had less deformation on the tip of blades and smaller Von Mises stress at the base of blades. Xie et al. (2015) tested a few different materials typically used in the slurry transport on the Coriolis slurry scouring erosion tester and Miller tester. Tungsten carbides and elastomers showed better wear resistance. Iwai et al. (1997) studied 13 different materials including polymers, metals and ceramic coatings. They also tested three lining materials in the

actual pump. They concluded that elastomer and rubber had higher wear resistance than metals. Sheldon (1970) discussed the similarities and differences of the wear behavior of different materials. Sheldon found that certain brittle materials were similar to ductile materials. Sheldon's results showed that the exponent on particle diameter for ductile and brittle materials was almost the same. The relationship between erosion resistance and strain energy is same for both ductile and brittle materials.

Lewis (1964) predicted the sliding wear of a polymer-matrix based on Holm's (1965) results on metal materials. Roy et al. (1993) proposed that the wear rate of polymer composites had an order of magnitude higher than that for metallic materials. Pool et al. (1986) concluded that the velocity exponent  $p$  will be in the range of two to three for a ductile polymer, but the value of  $p$  would be in the range of three to five for a brittle polymer.

To sum up, super hard metals are often applied in pump casing and impellers which sustain the most abrasion. Many investigations have been conducted on different metals to test wear resistance. Some studies on non-metallic materials used the experimental data of metal materials as a reference when determining the abrasive mathematical model.

### **1.2.8 Indicators for wear behavior**

To scale wear behavior on the impeller, some wear measurement methods need to be introduced. Summer (1987) indicated that the efficient ways to study pipeline erosion are weighing and surface morphology. Weight loss rate is a common indicator of wear rate because weighing or gravimetric measurement is the easiest method for performing. Chandel et al. (2012) used Scanning Electron Microscope (SEM) analysis as a surface activation technology. Because it is convenient and accurate, SEM analysis is often used in material engineering to observe the profile

of a surface and can determine the wear pattern (Garg et al. (2016), Xie et al. (2015) and Hemanth (2011)). Volume loss is also used to determine the wear rate (Batalovic (2010), Finnie (1960) and Hashish (1987)), especially when mass loss is inaccurate. For example, it is better to use volume loss when materials absorbing water, but sometimes volume loss is hard to detect when the shape of the samples is irregular. Weight loss can also be applied as a wear rate indicator when materials are water-absorbed, but the post-process should be conducted on the specimen i.e., the sample should be dehydrated in the oven.

### **1.2.9 Experimental methods for wear**

A Coriolis slurry erosion tester was created by Tuzson and Scheibe-Powell (1984) to simulate the flow pattern and wear on pump casing and the impeller in pipelines. Hawthorne et al. (2003) modified the design of the rotor-specimen holder assembly in this tester to more accurately model the slurry flow. Tian et al. (2005) used the Coriolis wear tester to determine the wear coefficient when predicting wear life. Tian et al. (2007) produced a new tester with a wide range of impact angles based on the Coriolis approach. Chandel et al. (2012) used the tester to study the way in which particle size, solid concentration and rotational speed affect wear behavior. Walker et al. (2015) looked at different mechanical properties of the wear rate of the erodent in the slurry to establish guidelines for how to choose a suitable erodent.

A pot tester is designed for a rectangular specimen under a 90° orientation angle with slurries. Clark et al. (1995; 2001; 2002) widely used pot testers to investigate the erosion wear process. Rajahram et al. (2011) studied the effect of velocity, sand size and sand concentration on a passive metal using a pot erosion tester. Amarendra et al. (2012) evaluated the material performance under water and slurry, with and without a cavitation inducer, using a pot tester.

Lindgren et al. (2014a) conducted experiments using a pot tester to study the influence of erodent on titanium and compare the results with 316L of stainless steel. Lindgren et al. (2014b) also used the method to study the same properties on austenitic and duplex stainless-steel grades.

A jet impingement tester is often used to study the effect of bulk flow properties on erosion. Yoganandh, et al. (2012) changed the velocity, slurry concentration, angle of impingement and pH to observe the difference in Ni-hard materials using a jet impingement tester. Zhao et al. (2015) tested three different erodents, sands, silica sand and sea sand, using this tester. Suh et al. (2011) tested the erosive mechanism of the new SiC composites using a jet impingement tester to feed the solids. Ojha et al. (2014) used the same method to determine the wear behavior of a polymer composite.

A toroid wheel tester (TWT) is often applied to study erosion-related problems in pipelines. Worster et al. (1955) developed the tester to investigate coal degradation. Cooke et al. (2015) found that this tester can simulate the flow in pipelines accurately, which is the most significant advantage of TWT. The disadvantage is the limited rotational speed. Sarker (2015) modified the TWT to study wear behavior in pipelines.

A pin-on-disc tester is often used to investigate the sliding wear behavior of the metal and non-metallic materials. Janssen, et al. (2017) used the pin-on-disc tester to confirm that the presence of laser manufactured dimples on the surface can reduce the friction and wear in the pump. Sarkar et al. (2010) evaluated the wear properties of a new composite made of industry waste (fly ash and aluminum matrix) using the pin-on-disc tester. Feyzullahoglu et al. (2010) used the pin-on-disc tester with lubrication to analyze the sliding wear rate on aluminum-based materials.

Walker et al. (2000) used less hard cast iron (HB 110) to accelerate wear and save time and cost when studying the wear relationship of side-liners. Wu, et al. (2011) used a multi-layer paint modeling technique to determine erosion damage “hot spots,” which is based on the similarity theory. Multi-layer paint technology has an advantage in cost and time-saving and is suitable for developing and optimizing flow geometries.

The methods mentioned above have a similar characteristic: they save time and money. The Coriolis slurry tester and pot tester have a similar principle. Both simulate the flow motion in the pump chamber by using centrifugal force. The jet impingement tester is used to simulate the movement that the particle around the pump impeller. TWT is often used to investigate abrasion in a pipe. Some researchers put samples in a simulated field condition but used some methods to accelerate experiments. Numerical analysis using CFD will be discussed in the next section.

### **1.2.10 Numerical analysis of flow motion and abrasive wear in the slurry pump**

Numerical analysis and computation to simulate the flow movement and wear behavior make up a significant part of the literature related to abrasive wear in slurry pumps. Liu et al. (2004) used a second-order dynamic model to solve the governing equations of solid-liquid flow and simulated a two-phase flow around the pump impeller. PIV technology was also used to observe the velocity of the particles and particle distribution. Liu et al. found that the relative velocity of both the radius and circumference decreased from the pressure side and suction side at the impeller outlet, which probably explains why vortex pump generates a second flow at the impeller outlet. The simulation results show slightly more particles near the pressure than near the suction side, and that the particles decreased from the impeller inlet and outlet due to diffusion. Li et al. (2011)

had similar simulated results: they found that more particles aggregated on the pressure side and there was more abrasion on this side. Zhang et al. (2013) used CFD to find that the velocity rises from the impeller inlet to the impeller outlet and that total pressure at the pressure side is higher than on the suction side. Also, a jet-wake flow structure was shown near the volute tongue, which causes an unequal level of relative velocity in each channel. The effects of separation flow and wake flow near the suction side of the impeller lead to an inconsistent passing flow rate. The concentration of the slurry can also affect the jet flow structure.

Comparing with the results of Liu (2004) and Li (2011), the results of Zhang (2013) is different. Zhang et al (2013) found that most particles are distributed on the suction side and so is the local concentration. In the tailing regions, the concentration is extremely high. The locations have a high local concentration and high particle numbers will have high levels of abrasion.

Gonzalez et al. (2002) captured a fluctuating pressure field at the blade-passing frequency. This phenomenon shows that the tongue region interacts with the flow at the impeller outlet and this effect intensifies with off-design conditions. The wake generated by the blades will superpose to the average pressure around the volute.

Wu et al. (2015) analyzed the velocity of the flow at the impeller outlet, particularly near the volute tongue, and found a velocity fluctuation phenomenon similar to the one identified by Gonzalez (2002). Wu et al. (2015) attributed the phenomenon to the interaction between the impeller and volute tongue. They also investigated the turbulence intensity distribution in the pump and found that turbulence flow often occurs at the suction side. They concluded that the appearance of a jet-wake might be one reason for energy losses and the reduction in maximum head and efficiency, which stabilizes but does not change the fluctuations.

In conclusion, studying wear behavior inside the pump using CFD is popular because some measurements that are difficult to be obtained in the experiments can be easily obtained using numerical simulations. Numerical analysis is also convenient and economical.

### **1.2.11 Pump performance**

The performance of the slurry pump with water flow and solid-liquid flow is often investigated due to its key role in transporting solids. Many factors can be attributed to the deviation in the performance curves. The specific head relationship works for both water and low concentration (less than 20 wt.%) slurry flows. However, for high concentration flows, the difference occurs with the data of water at each rotational speed (Gandhi, et al. 2002). Noon (2016) also found that the head and efficiency ratios dropped as slurry concentrations increased. The head and efficiency of the slurry pump can be influenced not only by the concentration of the slurry but also by the properties of the flow, for example, the size distribution of the slurry flow. Adding more fine particles can lead to reduce head loss, which will improve pump performance (Kumar et al., 2014). Burgess and Reizes (1976) confirmed the effect of size, specific gravity and concentration of the slurry on pump. Walker et al. (1984) found that rheological properties of slurries are reasons for the pump performance change. Walker et al. (1992) also concluded that the Froude number of particles mostly affects pump performance.

Geometry parameters of pumps are among the important factors affecting performance curves. Walker et al. (1992) studied the influence of vane numbers, inlet and outlet vane angles and the shape of the vane and found that the vane shape had the most effect on performance curves. Celtek et al. (2016) confirmed that the number of vanes is one of the most important parameters affecting the pump performance. Among the different number of blades, Celtek et al. (2016) found

that the three-blades impeller has the highest head. They also investigated blade heights from 30mm to 50mm. Their results showed that increasing the height of the blades increases hydraulic efficiency at a high flow rate while decreasing the head and shaft power.

An estimation of head-capacity characteristics was developed to save energy and improve efficiency. Roco et al. (1986) came up with a loss analysis to estimate the head-capacity curves when handling the solid-liquid mixtures. They tested their results on seven kinds of pumps and found that results were more accurate when the sand volume concentration is less than 35%. Gandhi et al. (1998, 2000) evaluated the leakage loss of clear liquid which can improve the prediction for pump performance with different slurry materials, solid concentrations, rotational speed and pump sizes. The losses in the centrifugal pump included impeller slip loss, mixing loss, frictional loss and energy loss. Gandhi et al. predicted the head-capacity characteristic based on these four losses.

### **1.2.12 Summary of literature review**

From the literature presented above, the erosion patterns are divided into three types due to mechanical damage: cutting, fatigue and brittle fracture. Wear behavior is related to the property of the erodent and the bulk flow and the target materials of the impeller. For erodent properties, the shape, size and materials will affect wear behavior. For bulk flow properties, the concentration of the slurry and velocity of the flow can also affect erosion behavior. The velocity of the flow can be changed through different pump operations. Theoretically, pumps need to be operated at the best efficiency point, which will help to reduce the wear rate. When the bulk flow rate is too small, it will increase the wear rate.



The wear rate can be calculated by the wear model that previous researchers came up with based on factors that influence the wear behavior; however, the wear coefficient is difficult to determine because the wear coefficient is different depending on materials used. Several experiments must be conducted to confirm the wear coefficient. Metal and non-metallic materials are fabricated and tested to ensure they can improve wear-resistant abilities. Different experiments such as the Coriolis wear tester, pot tester, TWT and pin-on-disc are common in laboratory testing. All these methods have advantages and disadvantages. Simulation using CFD is one of the most popular ways to investigate the flow motion and predict the wear rate. Some measurements that are difficult to conduct will be easier using the CFD method. The most commonly used indicators of wear behavior are weight loss and surface appearance. It is important to note that if the material absorbs water, then post-processing on the specimen should be performed. Wear behavior can affect the performance of the pump, which is a reason that pump performance under slurry flow deviates with the water flow. Thus, investigating wear behavior can help manufacturers to understand a pump's circulation life and improve performance.

For literature related to pump performance, most studies investigated the effect of slurry flow and impeller geometry on pump performance, few studies discussed on how damage impeller or other wet-end parts affect pump performance.

### **1.3 Research objective**

The primary objective of this project is to use the whole pipe loop in the laboratory to investigate the slurry pump performance and wear behavior of an impeller under different conditions. The major objectives include:

- Modifying the pipe loop in the laboratory to obtain pump performance curves.

- Understanding the flow pattern in the pump and the interaction between the solids of the slurry and the wall of the impeller.
- Analyzing wear behavior shown on the impeller under different experimental conditions.
- Analyzing wear behavior of the parts using FDM and Polyjet processes
- Finding how damage impellers affect pump performance

## **1.4 Thesis outline**

In this thesis, Chapter 1 introduces the background about slurry pumps, cost to maintain the pump system and wear in the pump. Also, this chapter includes literature reviews related to the wear model, wear mechanism, factors that affect wear behavior and previously used experimental methods. Research objectives and author's contributions are also in Chapter 1. Chapter 2 shows methods used in this project, which include the flow loop, instruments and equipment, the data acquisition system and materials of erodent and the target surface. Chapter 3 presents the results of the wear tests and head-capacity tests. Chapter 4 discusses the results. Chapter 5 includes the conclusions and recommends future studies.

## **1.5 Current contribution**

The following is a brief summary of the original contributions of this work, which is one of the requirements for an M.Sc. in Mechanical Engineering at the University of Alberta.

In this project, the pipe loop and data acquisition system were modified and customized for the experiments. The impeller in the original pump was measured using a laser scanner arm for the purpose of rebuilding a model of impeller in the SolidWorks. For every test, the pump was disassembled and assembled, and its operation was monitored. The samples for this project were

manufactured by Polyjet from the Stratasys Company based on drawings and designs I provided. head capacity tests and wear tests at different experimental conditions were performed. The samples were also pretreated and processed in each test. The results and analysis presented in this thesis were obtained. The pipeline received daily maintenance in the laboratory.

The presented analysis and investigation of the similarity relations are a completely novel approach and no similar studies were found in the literature. The procedure and analysis are unique in 2019 and suggest a new way to understand abrasive wear based on rapid and low-cost wear studies using soft materials to simulate the abrasive wear in harder materials.

## **2. Experimental Methods**

In the previous chapter, some literature related to the testing methods are introduced when studying abrasive wear are introduced. In this chapter, the experimental methods used in this work will be presented, including the pipe loop, main apparatus, instruments, samples, experimental procedures of wear tests and head-capacity tests.

### **2.1 Main apparatus in the flow loop**

In this section, the maker and model of the different apparatus will be shown. The testing pump and the setup of the pipe loop will also be introduced.

#### **2.1.1 Pipeloop**

The experimental setup is shown in Figure 2.1. The initial slurry loop was built by Victor Jaims and Suheil EI-Sayed (EI-Sayed,2010) and was further developed for the pump performance experiments and impeller wear behavior experiments. This loop was composed of 12 meters of two-inch Schedule 40 (true internal diameter is 5.25cm) plain steel pipe in the downstream of the pump and 5.5 meters of 3-inch rubber hose connected to 0.325 meters of three-inch Schedule 40 plain steel pipe (true internal diameter is 7.79cm) in the upstream. A slurry pump, knife-gate valve, and some ball valves and two tanks were added to the loop. Also, some measurement instruments such as pressure sensors and Coriolis flow meter (detailed makers, models and serial numbers will be introduced in Section 2.2) were used to observe the parameters of the flow loop. All the equipment used the flanged connection. This loop can functioned as a closed loop and open loop by switching the different open situations of Ball valve 1 and Ball valve 2. When Ball valve 1 was open and Ball valve 2 closed, the loop was a closed loop and the fluids in the loop could circulate

as required. When Ball valve 2 was open and Ball valve 1 closed, the loop was an open loop. Researchers can choose different modes as directed by research purposes.

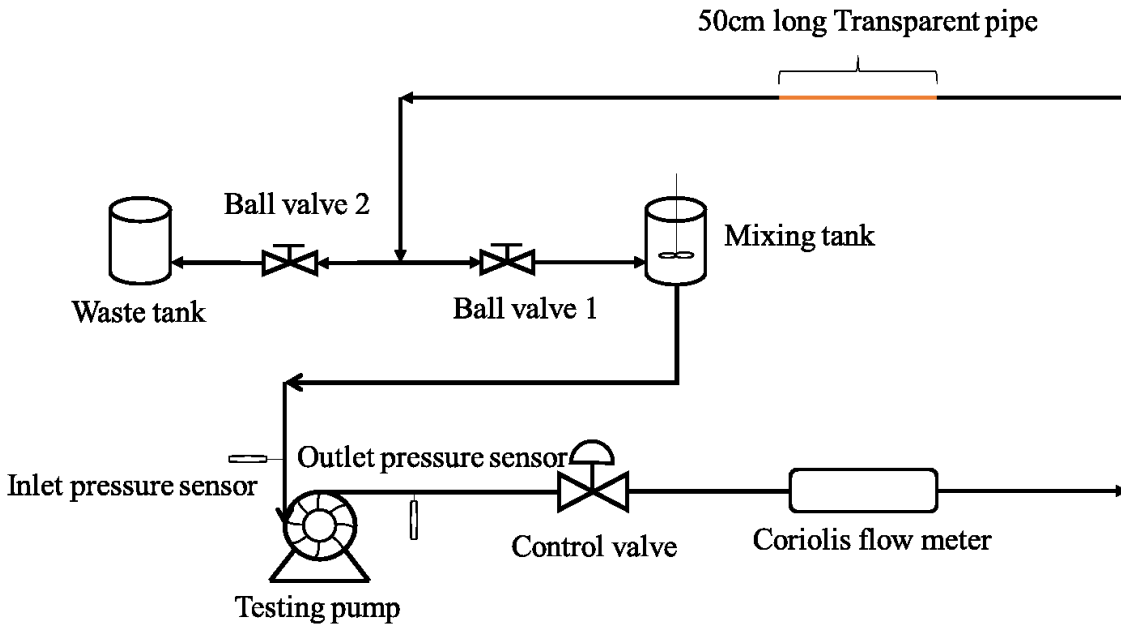


Figure 2.1. Schematic of testing loop

### 2.1.2 Slurry pump

The slurry pump in this project is from the Hayward Gordon Company (See Figure 2.2). The model is an XR2(7) Torus Recessed Impeller Vortex Pump. The pump size is  $2 \times 3 \times 7$ , which means that the discharge size, suction size and maximum nominal impeller size are two inches (5.08cm), three inches (7.62cm) and seven inches (17.8cm), respectively. This type of pump is often used to transport slurries. It is also one of the centrifugal pumps. The semi-open impeller is recessed in the back of the casing. The maximum rotational speed is 1765 rpm. The best efficiency is around 44%. This type of slurry pump often increases the service life at the cost of efficiency. This type of slurry pump that has a back-pullout structure can reduce the downtime for maintenance because all the wet-end parts can be taken out without disconnecting the motor and

shaft. The back-pullout structure makes it convenient for researchers to change the different impeller samples.

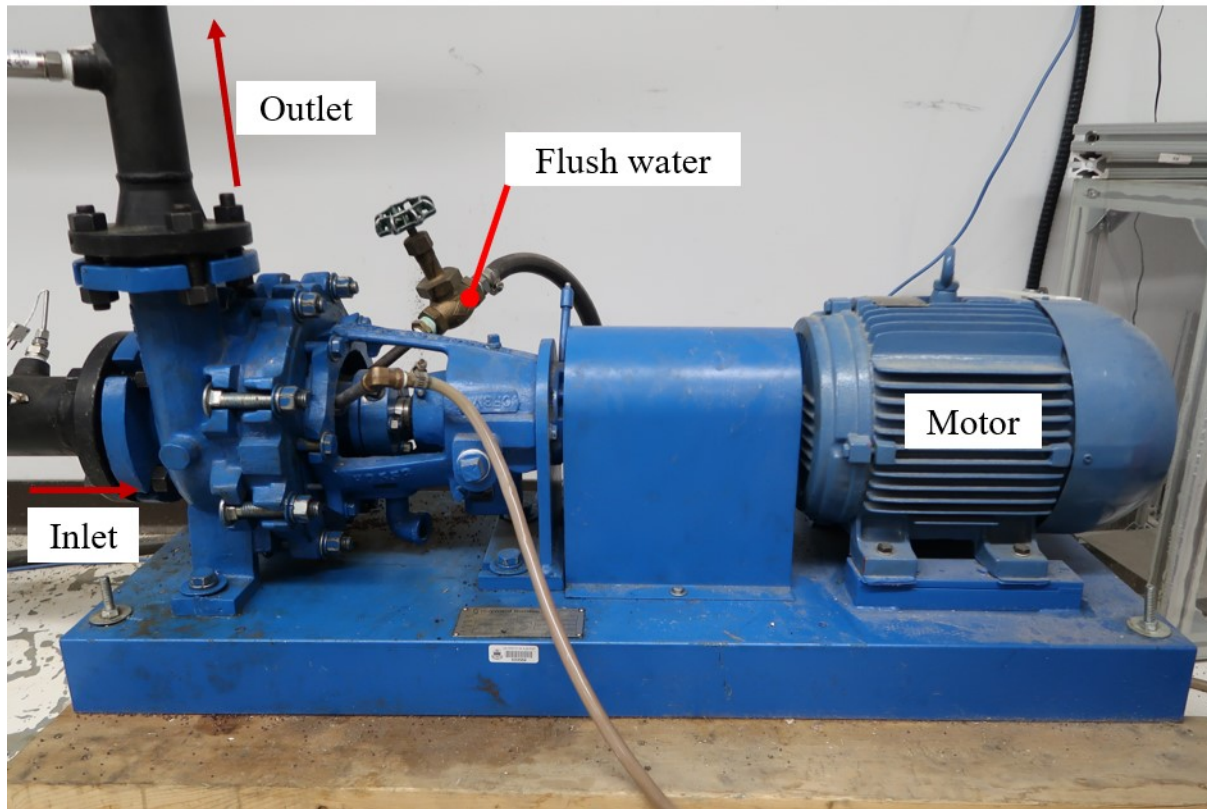


Figure 2.2. Slurry pump and motor

Figure 2.3 shows all the wet-end parts in this particular slurry pump. The wear plate often works as sacrificial because the cost to change the wear plate is not as high as the cost to change the impeller. The impeller has eight straight vanes. Straight vanes are easy to repair. The height of the vanes is two centimeters. Ni-hard and super Ni-hard metals are often used to cast the impeller to prevent abrasion. Ni-hard material ensures that the slurry pump will have maximum life. The one-piece casing has a certain thickness to ensure that it can deal with the solids up to eight inches (20.3cm).



Figure 2.3. Three wet-end parts

The motor to drive the pump is from the WEG Company (See Figure 2.2). The model is a W21 TEFC severe duty motor. It is a four-pole three-phase induction motor. The full load speed is 1765 rpm. The max frequency is 60 Hz. The motor is controlled by a Lenze ACT 0-60 Hz variable-frequency drive (VFD) unit.

### 2.1.3 Knife-gate valve

The control valve is a bi-directional resilient seated knife-gate valve from the Henry Pratt Company. The valve has a heavy-duty body design, and is very suitable for transporting slurry. Also, the stainless-steel stem can resist corrosion. With the knife gate valve, the liquid can go through the soft seals without interference.

### 2.1.4 Tanks

In this experiment, two tanks were put in the loop. One was labeled as a mixing tank, and the other as a waste tank. Sometimes the mixing tank worked as a waste tank and directly connected to the building drainage if the loop carried the city tap water without any harmful ingredient or large solids which may have clogged the drainage. If there were large solids in the flow, then the fluids would go to the waste tank, and there was a sieve under the tank to filter the

big particulates. Also, there was a rectangular bin underneath the sieve to catch the water and use the 0.5HP (372.85watts) submersible pump to transport waste water to the building waste line. If there are chemical components in the slurry, then the instructions of the Workplace Hazardous Materials Information System (WHMIS) should have been followed. An electronic mixer was mounted on top of the mixing tank. It was controlled by the Leeson Speedmaster Variable-frequency drive (VFD) with a frequency from 0 to 60 Hz. The mixing propeller had three blades and a drive shaft. A three-inch rubber hose connected the mixing tank to the inlet side of the pump to feed the fluids for the loop with. The mixer ensured better homogeneity of the slurry. Both tanks were the same size and made of polyethylene.

## **2.2 Measurement Instrument**

Measuring instruments will be presented in this section. Essential parameters related to this work will be measured. Also, the instruments' manufacturers and models will be shown. Precision, error and measuring range of instruments will be included.

### **2.2.1 Coriolis flow meter**

The Endress + Hauser Proline Promass 83i Coriolis meter was used in the pipeline. This type of flow meter can provide output for the normal parameters of the flow such as the mass flow, density and temperature. It is optional to output the inline viscosity measurement. The principle of the Coriolis flow meter is based on the Coriolis effect of the mass flow (Baker, 2000). The flow meter can obtain currents ranging from four to 20mA. In this experiment, the mass flow rate, temperature and density were chosen as parameters that shown in the front interface. The range and error of these three parameters are shown in Table 2.1. The flow meter was wired into a Data



Acquisition System (DAQ) using an NI-9208 module. The output data could be pre-scaled using an NI-DAQmx scale mode.

Table 2.1. The range and error of three parameters (Endress+Hauser Group)

	Mass flow rate	Temperature	Density
Range	0-10kg/s	0-100°C	500-1500kg/m <sup>3</sup>
Error	±0.1% for liquids ±0.5% for gases	±0.5°C ± 0.005 · T °C	±0.0005 g/cm <sup>3</sup>

### 2.2.2 Pressure sensor

The pressure drop between the inlet and outlet of the pump should be obtained for further analysis. Two identical American Sensor pressure transducers (model AST4000P00002B4E1000) were separately installed on the suction and discharge sides of the pump. The pressure sensor output was four to 20mA current, detectable by the DAQ system. The range of measurable pressure was from 0 to 2 bars (0-29 psi). The transducers were threaded into 0.5-inch NPT sockets and wired into the NI-9208 module. The output data could also be pre-scaled using the NI-DAQmx mode.

### 2.2.3 Tachometer

To ensure the accuracy of the rotational speed controlled by the VFD, the combination of tachometer/stroboscope (Extech Inc. Model: 461825) was used to detect the rotational speed. The specification of the detector is shown in Table 2.2.

Table 2.2. Specification of the photo tachometer/stroboscope

Specification	Photo tachometer (rpm)	Stroboscope (fpm/ rpm)
Range	5-99999	100-100000
Accuracy	$\pm 0.1\%$ rdg	$\pm 0.1\%$ rdg
Sampling time	1 sec $\geq$ 60 rpm	1 sec $\geq$ 60 rpm
Resolution	0.1 rpm (<1000 rpm)	0.1 fpm (<1000 fpm)
	1 rpm ( $\geq$ 1000 rpm)	1 fpm ( $\geq$ 1000fpm)

A short distance of the shaft of the pump was exposed to be used to observe the rotational speed. A small white piece of paper was attached to the shaft to be easily detected by the tachometer. The tachometer was held near the shaft. The exact location is shown in Figure 2.9. When the rotational speed was smaller than 1000 rpm, the tachometer needed to be at the 100-1000 rpm mode. When the rotational speed was over 1000 rpm, the tachometer needed to be switched into the 1000-10000 rpm mode.

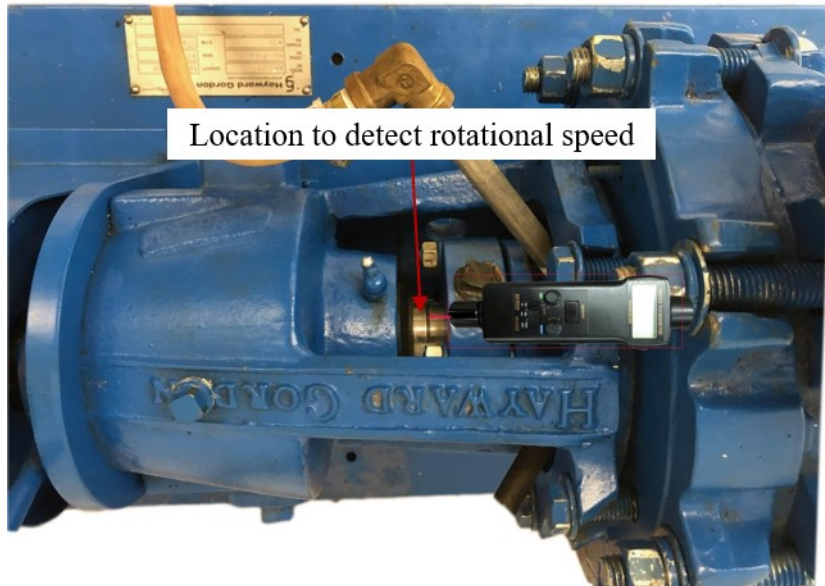


Figure 2.4. The position for a tachometer

## 2.2.4 Other instruments

To build the impeller using Computer aid design software (SolidWorks), the impeller needed to be measured using the laser scanner (Faro Laser Scanning, FaroArm Platinum) to digitalize a geometry that the 3D printer could recognize as an input model. Therefore, reverse engineering needed to be performed first. A flexible scanning arm with a high-resolution probe was able to digitalize most features of an impeller. The laser scanning machine used had three highly maneuverable arm lengths of -2.5m, 3.5m, and 4m. It also had a combination of contact and disconnects modes suitable for many complex parts. This kind of method was suitable for reverse engineering. Add-on software could be installed in SolidWorks, which was used to obtain the impeller measurements. With this data, it was possible to build a 3D virtual model in SolidWorks.

## 2.3 Erodent material in wear experiments

Silica sand is one of the most easily accessible and popular materials in mining industry. Many researchers use silica as erodent when investigating wear. At the beginning of our wear experiment, the solids used in the slurry were medium-sized SIL-4 industrial blasting sand. This sand is 40-50 US mesh size (297-420  $\mu\text{m}$ ). It was obtained from the SIL Industrial Minerals Company. There was not an obvious wear scar on the impeller after wearing for five hours. Ultimately, we chose to use garnet because they are easily available and not very expensive and produce a higher wear rate due to their shape and hardness. The size distribution of the garnets is shown in Table 2.3. The garnets are also displayed in Figure 2.10. The garnets have sharp edges that can quickly produce scratches on the samples.

Li (2011) found that the impact was visible when the volume concentration was larger than the 2.5% and it became drastic when beyond 10%. Thus, the weight concentration of our experiments was determined to be 5%, 10% and 15%.

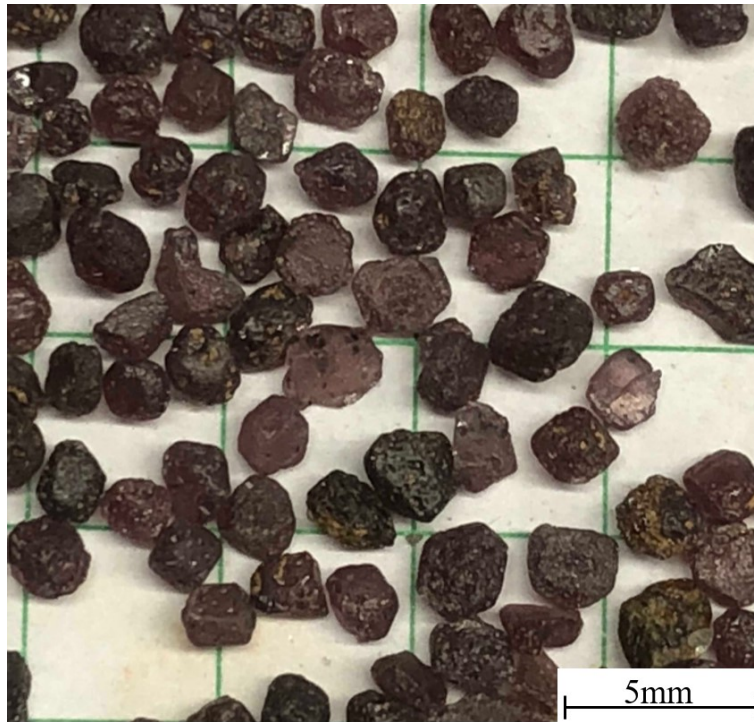


Figure 2.5. Magnified view of garnets' erodent on 5mm square grid

Table 2.3. Specification of garnets (Sil Industrial Minerals)

Particle size (mm)	Sieve (US standard)	Percentage retained
2.38	8	0-10
1.68	12	40-75
1.41	14	20-40
1.19	16	0-5

## **2.4 Impeller material in wear experiment**

### **2.4.1 3D printing technology**

Soft materials were first thought to be applied in this project to reasonably accelerate the experiments. To shorten the manufacturing time, rapid manufacturing technology was used to produce impeller samples in this project. Impellers made of plastic were applied because they can show wear behavior in a short time, which can save time. Also, plastic is cheaper than metal. With plastic samples, the wear location and wear pattern can be easily obtained. With the development of additive manufacturing (AM), it is convenient to manufacture samples or prototypes using a 3D printer.

Fused deposition modeling (FDM), Selective laser sintering (SLS) and polyjet are the classic types of AM. FDM is a process using a thin filament of plastic, melting it and then extruding it to a specific thickness (Wong & Hernandez, 2012). The most important advantage of FDM is that it is cost-effective (Wong & Hernandez, 2012). SLS is a process in which the powder is sintered or fused by a carbon dioxide laser beam (Wong & Hernandez, 2012). Using a 3D printer with SLS technology, more materials, even metals can be applied in production. For example, copper can be reinforced into a polymer, thus, improving the mechanical properties. The disadvantage of SLS is that the producing environment has very strict conditions: oxidation must be avoided and the temperature kept constant (Wong & Hernandez, 2012). Polyjet is a process that uses inkjet technology. The layer thickness can reach 16 $\mu$ m, which means that the parts produced have a high resolution (Wong & Hernandez, 2012).

In this project, we used the FDM process with Acrylonitrile Butadiene Styrene (ABS) and PolyLactic Acid (PLA) materials and Polyjet 3D-printing technology with Verogray material. In the 3D printing process, the process parameters such as layer thickness, part-build orientation, the raster angle, the raster width, and air gap had the potential to influence the mechanical properties of the parts (Sood et al. 2012). Part-build orientation can affect the tensile, flexural and impact strength (Es-Said et al. 2000). Layer thickness, and the raster angle and air gap will affect the elastic performance (Khan et al. 2005). It is believed that wear behavior can also be affected by these process parameters.

## **2.4.2 Alternative materials in 3D printing technology**

Sample impellers used ABS, PLA and Verogray in this project. These three materials are commonly used and easy to obtain in the AM process. In addition, these materials are relatively cheaper compared to materials such as nylon or composites with metal enforcement. Figure 2.11 shows impellers made of three different materials. The ABS and PLA were used in FDM process and Verogray was used in the Polyjet printer. The samples built using ABS and PLA have obvious layer liners and air gaps in the produced parts while the samples built using the Polyjet printer have fine resolutions and show details. The weights of Verogray impeller, ABS impeller and PLA impeller are 559.0g, 415.7g and 178.6g, respectively. The air gap between the ABS impeller is smaller than that in the PLA impeller. The impellers built using Polyjet had the best high-resolution surface finish. For example, the back blades of the impeller did not print well; they printed with a flat plan. In general, the quality of the Verogray impeller was the best and the quality of the ABS impeller was better than that of the PLA impeller. Also, the Verogray impeller was the most expensive. The ABS impeller cost more than the PLA impeller.

The Stratasys F123 3D Printer Series was used to build the PLA impeller and Fortus 3D printer for the ABS impeller. The comparison of the mechanical properties and thermal properties of ABS, PLA and Verogray are shown in Table 2.4 and Table 2.5, respectively. Table 2.4 shows that the tensile strength of these three materials is similar, but the tensile elongation is different, which means that the Verogray material has a relatively high deformation. The water absorption properties of ABS and PLA are not provided, but both materials can absorb water. The exact values of their water absorption are unknown. The data in Table 2.5 show the safe temperature used to dehydrate the samples.

The surface roughness of ABS, PLA and Verogray is closely related to the dimensional accuracy. For the FDM process 3D printer, the dimensional accuracy was  $\pm 0.5\%$ , and for the Polyjet it was  $\pm 0.1\%$ . In other words, the samples produced by the Polyjet 3D printer had the smoothest surface, and those produced by the FDM process 3D printer with PLA materials had the roughest surface of the three materials.

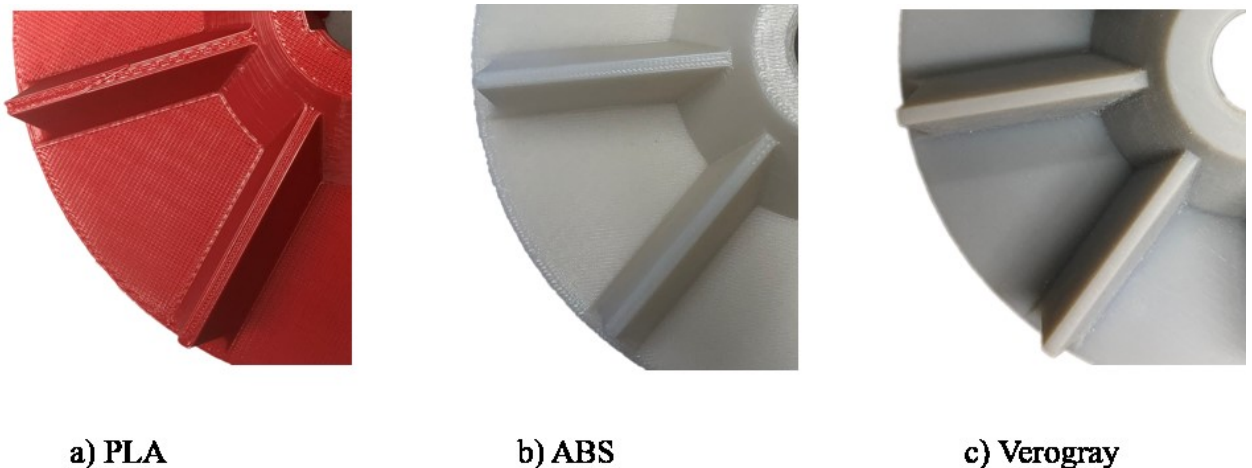


Figure 2.6. Samples using three different materials (PLA, ABS, Verogray)





Figure 2.7. Verogray impeller sample

Table 2.4. Comparison of ABS, PLA and Verogray mechanical properties (Stratasys Company)

Mechanical properties	ABS	PLA			Verogray
		XZ Axis		ZX Axis	
Tensile strength (ASTM D638) (Type 1, 0.125", 0.2"/min)	41MPa	Yield	45MPa	26MPa	58MPa
		Ultimate	48MPa	26MPa	
Tensile modulus (ASTM D638) (Type 1, 0.125", 0.2"/min)	1900MPa	3039MPa		2539MPa	N/A
Tensile elongation (ASTM D638) (Type 1, 0.125", 0.2"/min)	6%	Break	2.5%	1%	10%-25%
		Yield	1.5%	1%	
IZOD impact, notched (Method A, 23°C)	196J/m	27J/m		N/A	25J/m
IZOD impact, un-notched (Method A, 23°C)	481J/m	192J/m		N/A	N/A
Water absorption	N/A	N/A			1.1%-1.5%

Table 2.5. Comparison of ABS, PLA and Verogray thermal properties (Stratasys Company)

Thermal properties	ABS	PLA	Verogray
Heat deflection (ASTM D648) (HDT) @ 66psi	110°C	53°C	48°C
Heat deflection (ASTM D648) (HDT) @ 264psi	96°C	51°C	48°C
Vicat softening temperature (ASTM D1525) (Rate B/50)	112°C	54°C	N/A
Glass transition temperature (DMA SSYS) (Tg)	125°C	63°C	52-54°C
Coefficient of thermal expansion (flow)	N/A	$101 \times 10^{-6} \mu\text{m} / (\text{m} \cdot ^\circ\text{C})$	N/A

## 2.5 Data Acquisition System

The National Instruments LabView is the software that applied for the data acquisition system (DAQ). The DAQ system was divided into three parts: flow rate, temperature and pressure. Every parameter had a line chart to show the change of these three parameters. For the block diagram of the program (See Figure 2.13 & 2.14), a while loop was used to obtain data every time when stopping the program. Once the sensor began to obtain the data, the DAQ system would scale the current into different values using the DAQ assistant module. Four signals were separated and shown in different ways. Also, these signals were written into the excel file every time using files with different names.

When coding the DAQ system, the DAQ assistant module was selected to set the data channel. Each parameter had to be scaled at first (see figures in Appendix D). Other parameters

were scaled using the same method. Due to the limitation of the computer configuration, the continuous samples mode with 1000 samples at 1000 Hz sample rate was chosen when performing experiments of the head-capacity curves of the pump, but for the wear testing, the one sample on the demand acquisition mode was chosen (see figures in Appendix D).



Figure 2.8. LabView block program (front interface)

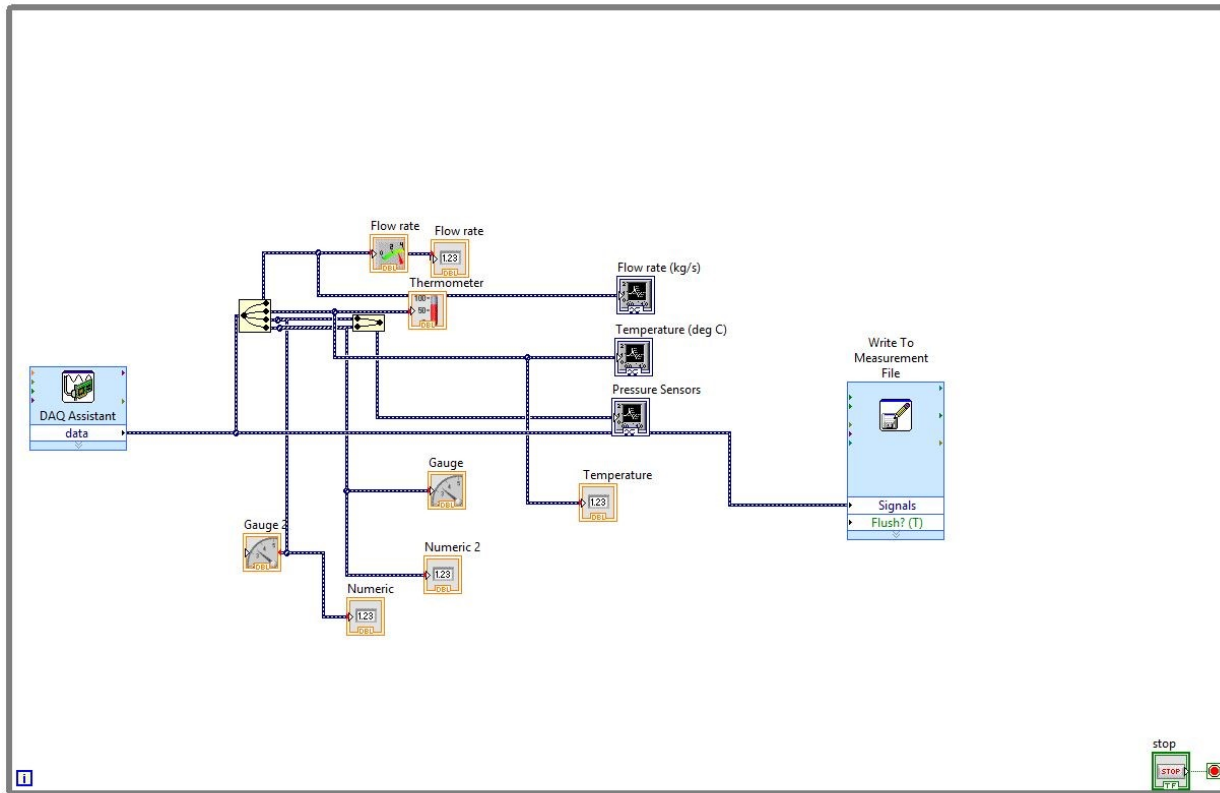


Figure 2.9. LabView block program (back interface)

## 2.6 Calibration

Calibration is essential before starting an experiment. In performance experiments for the pump, the pressure difference between the suction and discharge sides needed to be carefully treated. Thus, it was valuable to calibrate the two pressure sensors.

The calibrator used was from OMEGA (See Figure 2.15). It was suitable for pressure under 30psi, which was appropriate for the pressure transducers in the experiment. The pressure sensor was connected using different bushings to fit the calibrator. The software used was NI-MAX. With the NI-max module, the current could be scaled into pressure with a unit of psi. There is an

individual calibration part in NI-max software to calibrate the different sensors. The value of the calibrator defaults as the reference value. The procedure for calibration is:

1. Input the reference of the pressure value every five psi from 0psi to 29psi in the NI-max calibration wizard.
2. Use the built-in pump to increase the pressure to the maximum value of the sensor (29psi).
3. Press the “Commit Calibration Value” button when the OMEGA calibrator is showing the max value.
4. Every time the pressure decreases 5psi, press the “Commit Calibration Value” button.
5. In the end, a series of data can be obtained, which is reference data, uncalibrated data and calibrated data.
6. Keep repeating Step 1-5 until the mean square error of the uncalibrated and calibrated data is lower than 0.05.



Figure 2.10. OMEGA calibrator

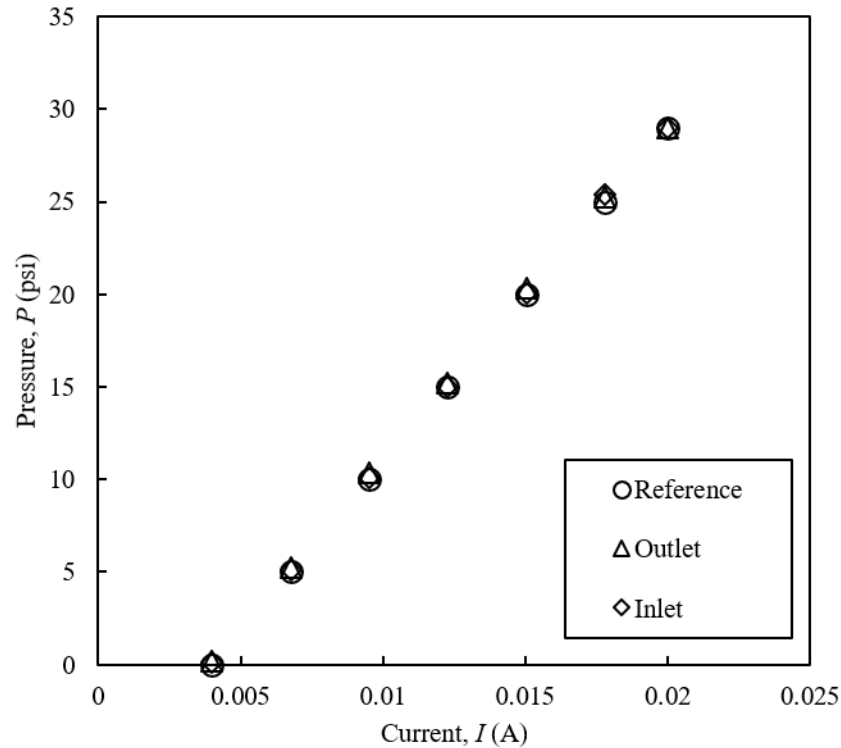


Figure 2.11. Calibration results

Figure 2.16 shows the calibration results. After two or three calibrations, the data of the outlet pressure sensor and inlet pressure sensor are very consistent with the reference data. The relationship between current and pressure is linear. Thus, after the calibration, the pressure transducers are ready to be used in the experiments.

## 2.7 The principle of performance experiment

Performance curves include head-capacity relationship ( $H-Q$ ), power-capacity relationship ( $P-Q$ ) and efficiency-capacity relationship ( $\eta-Q$ ). Pumps give energy to the fluids to move through the pipe and overcome the friction and the effect of any changes in elevation (Wilson, 2006). This energy is composed of pressure energy, potential energy and kinetic energy (Wilson, 2006). Bernoulli's equation is often used to express the three energy terms as the head of the liquid. Head

is the measure of mechanical energy of a flowing fluid per unit mass and indicates that the height of the fluid would rise if the energy converts into potential energy (Wilson, 2006). The unit of the head is metric. The total dynamic head (TDH) of the pump can be calculated by the following equation (Wilson, 2006):

$$\text{TDH} = \frac{V_B^2 - V_A^2}{2g} + \frac{P_B - P_A}{\rho_f g} + (Z_B - Z_A) \quad (2.1)$$

Where TDH is the total dynamic head;  $V_A$  is velocity at the suction side;  $V_B$  is velocity at the discharge side;  $P_A$  is pressure at the suction side;  $P_B$  is pressure at the discharge side;  $\rho_f$  is the density of the liquid;  $g$  is gravity acceleration;  $Z_A$  is the elevation of the reference level at the suction side;  $Z_B$  is the elevation of the reference level at the discharge side;  $(Z_B - Z_A)$  is the static head.

The output power of the pump can be calculated by (Wilson, 2006):

$$P_{out} = \rho_f g Q H \quad (2.2)$$

Where  $P_{out}$  is the output power;  $\rho_f$  is the density of the liquid;  $Q$  is the flow capacity;  $H$  is the total dynamic head of the pump.

The torque on the shaft gives the driving force of the pump, and it can be determined by the angular velocity. The angular velocity of the pump can be known by:

$$\omega = 2\pi n = 2\pi N/60 \quad (2.3)$$

Where  $\omega$  is the angular velocity;  $n$  is the rotational speed measured in revolutions per second;  $N$  is rotational speed measured in revolutions per minute. The input power of the pump is given by:



$$P_{in} = 2\pi nT = 2\pi NT/60 \quad (2.4)$$

Where  $T$  is the torque of the shaft;  $P_{in}$  is the input power of the pump. The efficiency of the pump can be calculated by:

$$\eta = \frac{P_{out}}{P_{in}} \quad (2.5)$$

Where  $\eta$  is the efficiency of the pump.

## 2.8 Experiment procedure

### 2.8.1 Flow capacity /Head ( $Q/H$ ) experiment

The  $Q/H$  experiments should be conducted before wearing and after wearing. With these experimental data, the head loss due to a damaged impeller can be noticed.

In the performance experiment, the variables are:

- The controlled variables: carrier fluid properties (tap water).
- The independent variables: rotational speed of the pump.
- The dependent variables: flow rate, inlet and outlet pressures.

For the performance experiment of the pump, the closed loop was chosen, which means the fluid would not go into the waste tank and instead circulated until enough data was obtained.

The process of the experiment was:

1. Add tap water into the loop
2. Set frequency on VFD panel
3. Set the control valve fully open using the hand wheel

4. Change the loop into a closed loop
5. Turn on the pump
6. Open the DAQ system to record the data
7. Close the control valve slowly until nearly closed
8. Set a different rotational speed
9. Repeat Steps 1-8
10. After enough data has been obtained, close the DAQ system and turn off the pump

The important thing is that the control valve should be adjusted at a constant speed to obtain the most data about the pressure difference. To be agreed with the manufacturer's reference data, the rotational speeds (850, 950, 1050, 1150, 1250, 1350, 1450, 1550, 1650 and 1750 rpm) are set and each corresponds to the frequency on the VFD (28.5, 31.9, 35.3, 38.6, 42, 45.4, 48.8, 52.1, 55.6 and 59 Hz). Each rotational speed was checked using the tachometer.

## **2.8.2 Wear experiment**

In the wear testing experiment, the variables were:

- The controlled variables: the carrier fluid properties.
- The independent variables: rotational speed of the pump.
- The dependent variables: the wear rate, inlet and outlet pressures, flow rate, and particle velocity.

The wear experiment used the same loop described in Figure 2.1. Due to budget limitations, the tested solids were circulated in the loop for 24 hours. A repeated experiment cannot be applied to every experimental condition. The closed loop mode was applied until the one test was completed. Also, a closed loop can reduce the pump cavitation effectively, because the net positive

suction head (NPSH) is around 13 feet from the manufacturer's reference data. The conditions of the wear testing are listed in Table 2.6. The weight concentration, which were chosen arbitrarily, were 5%, 10% and 15%. Some water levels were marked on the tank to show the volume of the fluid including the fluid in the pipeline. In every test, the city water added up to 200 liters. Ten kilograms, 20 kilograms and 30 kilograms of the solids were weighed for 5wt.%, 10wt.% and 15wt.%, respectively. The sample was run for 110 hours at a rotational speed of 1200 rpm and 5wt.% of solids, and changed erodent every 24 hours. The sample was also taken out of the pump and cleaned and dried for four to five hours. Mass loss per second was chosen to describe the wear rate in the experiment. The test specimens should be weighed before and after testing. The procedures for wear testing are:

1. Clean and weigh the sample impeller.
2. Install the sample impeller in the pump (See Figure 2.17).
3. Add the tap water up to 200 liters in the mixing tank (water level marks on the tank can be the reference).
4. Weigh the required amount of garnets and add to the mixing tank.
5. Set the rotational speed on the VFD panel and turn on the pump.
6. Open the DAQ system.
7. Circulate the garnets for a required number of hours.
8. Stop the pump.
9. Switch Ball valve 2 to the open position and switch Ball valve 1 to the closed position. Change the loop to an open-mode loop.
10. Start the pump again and clean the loop several times until there are no solids left in the loop.

11. Disassemble the testing pump and take out the impeller.
12. Clean and weigh the sample

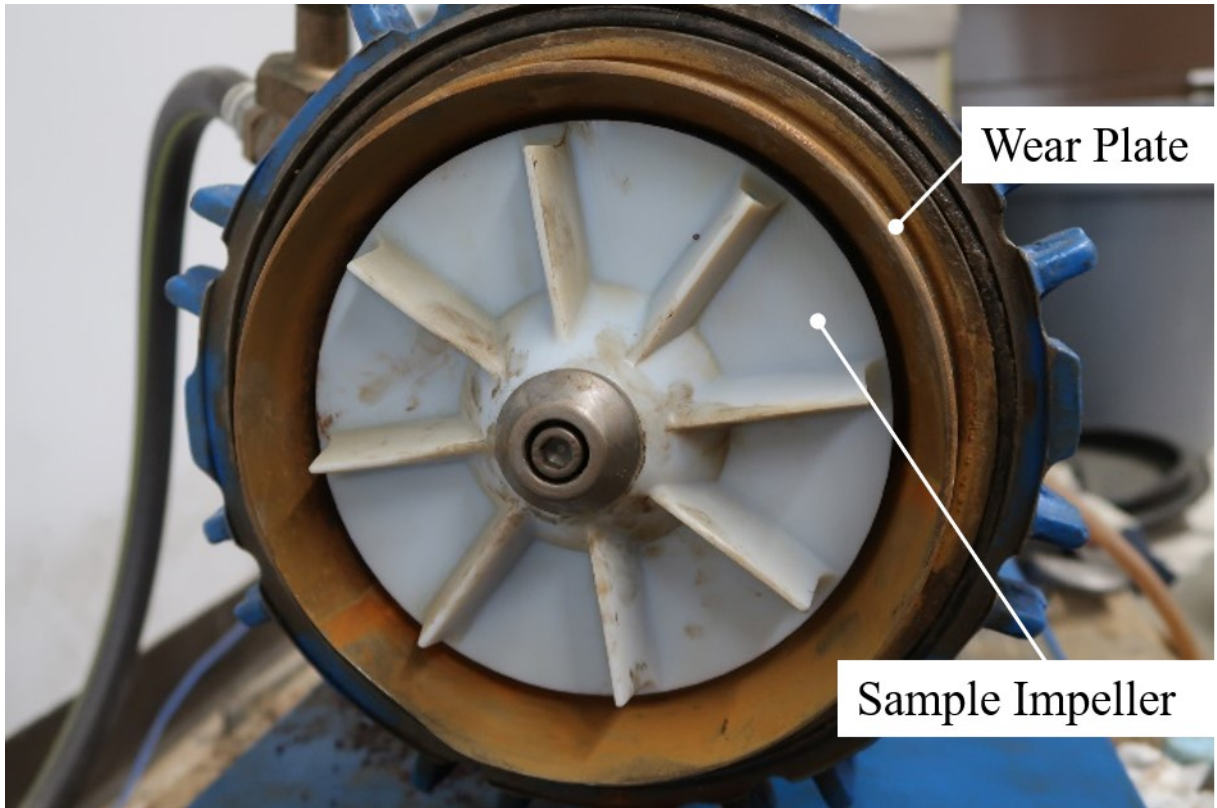


Figure 2.12. Sample impeller in the pump chamber

The samples were cleaned by ethanol. To reduce the water left in the samples, the samples were dehydrated in an oven for around four hours at 50°C, The time and temperature were adjusted, depending on how much water was left in the samples. Also, the pipe loop had to be cleaned carefully. With these operations, the pipe loop can be used for the next  $H/Q$  experiments. Under these experimental conditions, the rotational speeds are from low to high, and concentration from low to relatively high are also covered. Due to cost limitations, the repeated experiment was conducted only at 1200 rpm and a 5wt.% concentration for 24 hours.

Table 2.6. Experimental conditions

Rotational speed (Hz)	Rotational speed (rpm)	Weight Concentration
		5%
35	1050	10%
		15%
		5%
40	1200	10%
		15%
45	1350	10%
50	1500	5%
59	1765	5%

In conclusion, the main part investigated in this study was the slurry pump impeller. The soft materials were used to manufacture the samples to provide reasonable acceleration. To reduce the sample preparation time, it is convenient to use 3D printing technology to build the trail parts. The parameters that should be measured are flow rate, temperature and inlet and outlet pressure. Different instruments were used and wired into the DAQ system. LabView was used to set up the DAQ system. Wear tests and head-capacity tests were conducted using the laboratory pipe loop. Different experimental conditions or operations were performed on the samples to study the possible parameters that affected the pump's abrasive wear behavior and performance.

## **3. Experimental Results**

### **3.1 Preliminary experimental results**

Before deciding which material was suitable for wear testing, preliminary experiments were performed. The impeller built using Polylactic Acid (PLA) was first excluded because the prototype could not show all the details of the model. The Acrylonitrile Butadiene Styrene (ABS) impeller was put into the pump. For the next 24 hours wear-testing was conducted using garnets as the erodent. The experimental condition was 1200 rpm and 5wt.% solid concentration. Figure 3.1 shows the damaged surface. The sample exposed the locations that underwent the most abrasion. Because of how the FDM 3D printer works, it was possible to observe the filaments; even broken sections of the filaments could be seen even by the naked eye. Although the sample using ABS materials was geometrically stable despite undergoing wear and displaying worn surfaces, it was easy for dust in the carried slurry to remain in the air gaps. Dust that remains in the samples may increase the post-processing time. The ultrasonic bath was used to remove the dust in the air gaps. The samples were dehydrated in the oven for several hours, but the final weight was still higher than that of the original samples, which meant that there was still dust in the samples. Thus, the ABS samples were not suitable for wear testing; however, samples using Verogray materials from the Polyjet 3D printer were better than the ABS samples, because the Verogray samples had a more homogeneous texture and a smooth surface without air gaps. The Verogray samples may yield more accurate results than ABS samples.

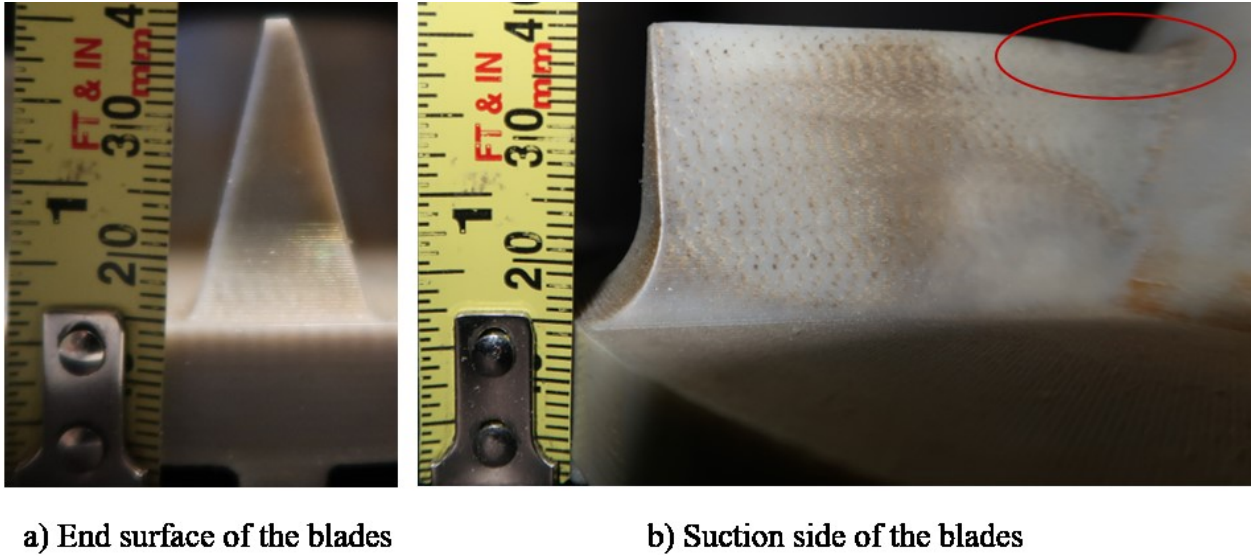


Figure 3.1. ABS samples after 1200 rpm and 5wt.% solid concentration and a wear time 24 hours

### 3.2 Wear pattern observation

Figures 3.2 to 3.10 display wear patterns on the Verogray impellers. Eight blades have the same wear pattern. The greatest number of wear spots is on the blades of the impellers, especially near the hub and the trailing edge and the intersection between the blades and the hub. Based on the description of Kruger et al., the wear pattern at the trailing edge is a friction-like process (See Figure 3.2). The locations that have obvious abrasion are marked in Figures 3.2-3.10. The suction side of the blades has more abrasion than the pressure side (See Figures 3.3 and 3.4) When the impeller is running at a high rotational speed, the garnets have high velocity at local areas and cause more severe abrasion. Unlike the metal impellers, the worn surfaces on the samples are very smooth, and pits or visible fatigue patterns are not found. This phenomenon happens because the rapid impingement causes local deformation on the impeller, which also happens in metal, but the area is small and cannot be easily observed. The samples in this project are made of polymer which

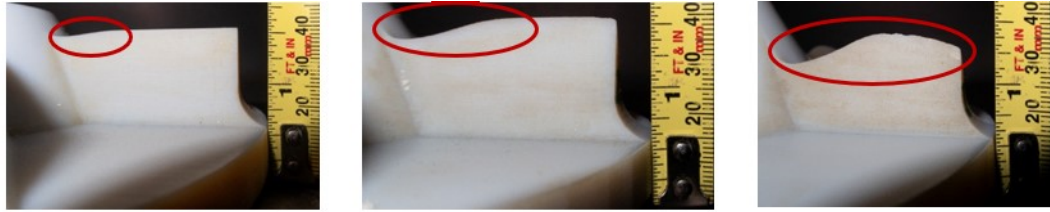
enlarges the deformation effect. As the rotational speed increases, the height of the blades decreases. Similarly, the height of the blades decreases when the concentration of the erodent increases. The effect of the solid concentration is smaller than that of impeller rotational speed (Figure 3.8 to 3.10). From Figure 3.5 to 3.7, the wear on the impeller occurs gradually: i.e., the leading edge of the blades are the first to be worn and the trailing edge begins to wear after a few hours.



a) 1200RPM-5wt.%-24hours    b) 1500RPM-5wt.%-24hours    c) 1750RPM-5wt.%-24hours

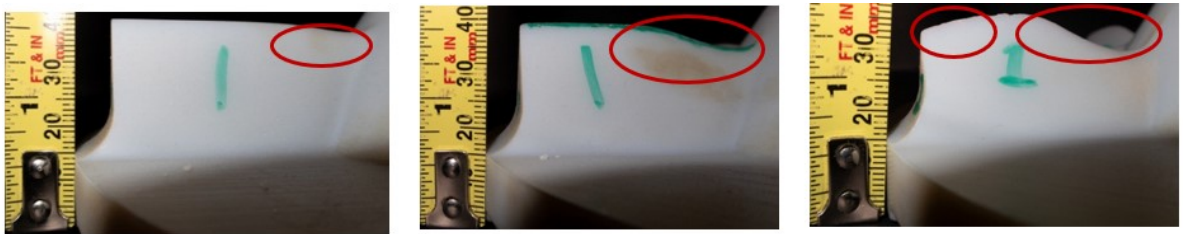
Figure 3.2. Worn surfaces at the end of the blades after different rotational speeds (1200 rpm, 1500 rpm, 1750 rpm), same concentration (5% weight concentration) and wearing time (24 hours)





a) 1200RPM-5wt.%-24hours    b) 1500RPM-5wt.%-24hours    c) 1750RPM-5wt.%-24hours

Figure 3.3. Pressure sides of the blades after different rotational speeds (1200 rpm, 1500 rpm, 1750 rpm), same concentration (5% weight concentration) and wearing time (24 hours)

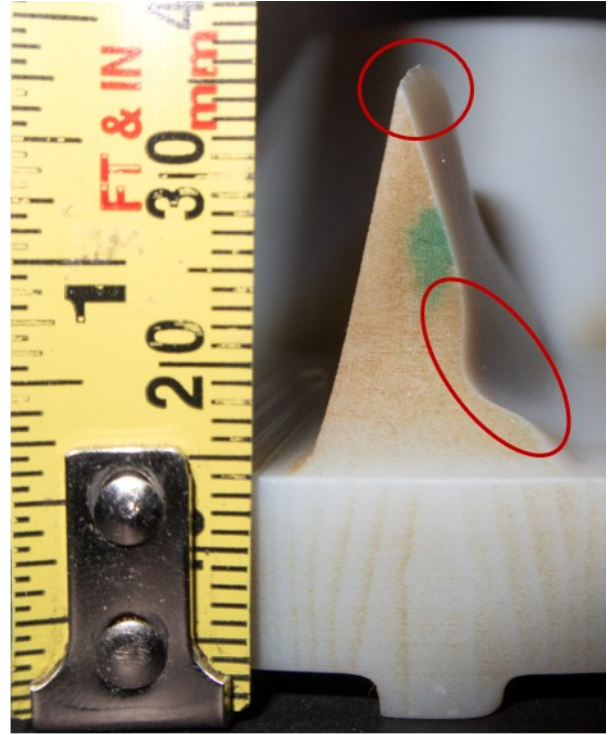


a) 1200RPM-5wt.%-24hours    b) 1500RPM-5wt.%-24hours    c) 1750RPM-5wt.%-24hours

Figure 3.4. Suction sides of the blades at different rotational speeds (1200 rpm, 1500 rpm, 1750 rpm), same concentration (5% weight concentration) and wearing time (24 hours)

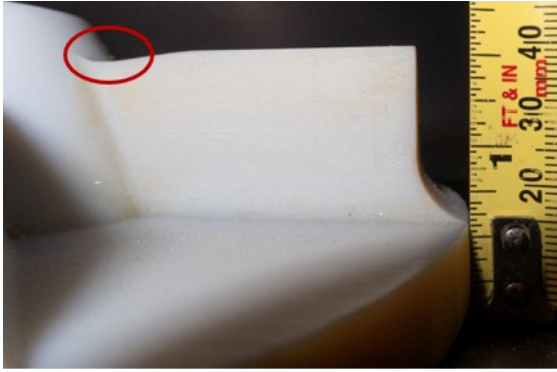


a) 1200RPM-5wt.%-24hours

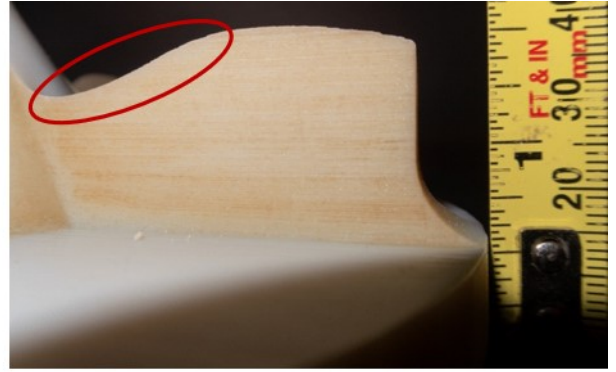


b) 1200RPM-5wt.%-110hours

Figure 3.5. Worn surfaces at the end of the blades after different wearing time (24 and 110 hours) at the same rotational speed (1200 rpm) and concentration of solids (5% weight concentration)



a) 1200RPM-5wt.%-24hours

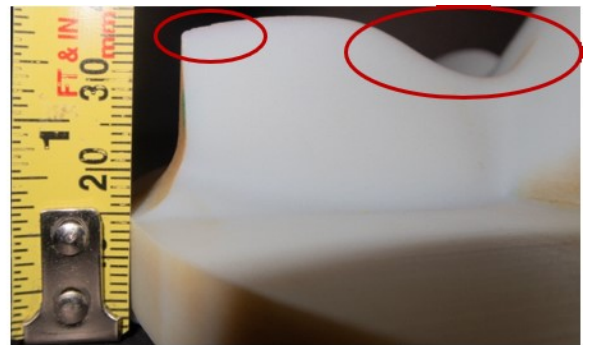


b) 1200RPM-5wt.%-110hours

Figure 3.6. Pressure sides of the blades after different wearing time (24 and 110 hours) at the same rotational speed (1200 rpm) and concentration of solids (5% weight concentration)



a) 1200RPM-5wt.%-24hours

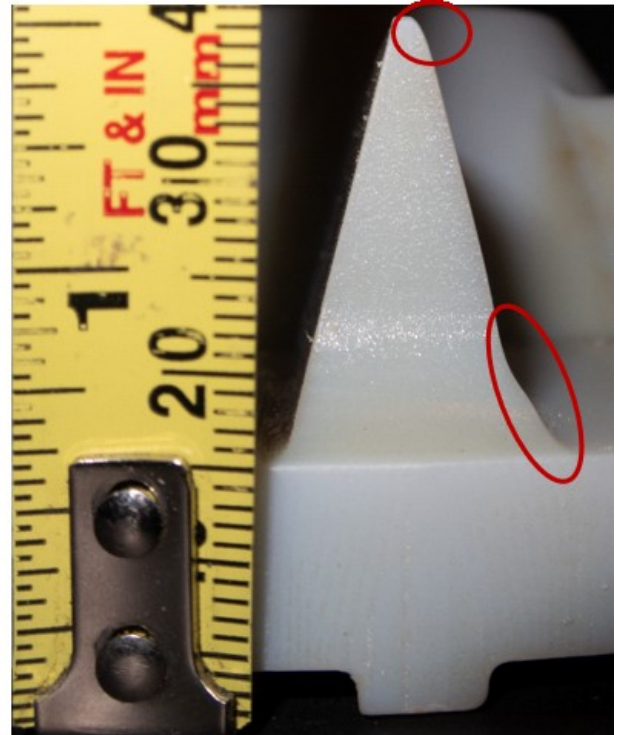


b) 1200RPM-5wt.%-110hours

Figure 3.7. Suction sides of the blades after different wearing time (24 and 110 hours) at the same rotational speed (1200 rpm) and concentration of solids (5% weight concentration)

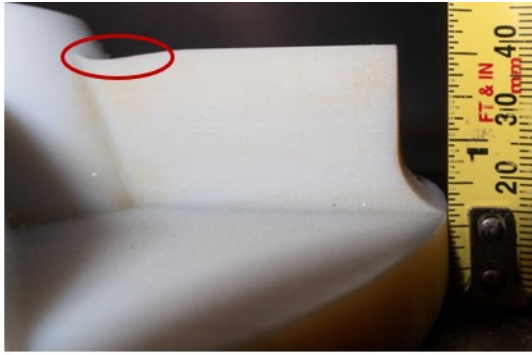


a) 1200RPM-5wt.%-24hours

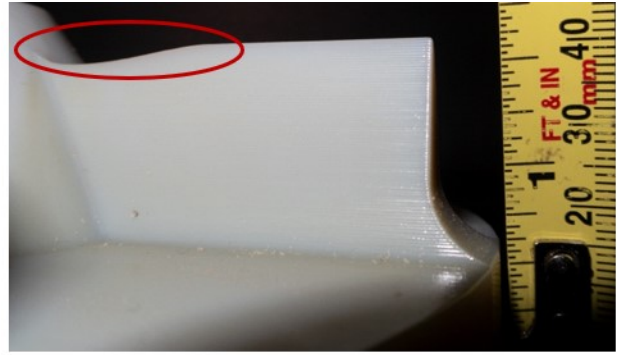


b) 1200RPM-10wt.%-24hours

Figure 3.8. Worn surfaces at the end of the blades after different concentrations of solids (5% and 10% weight concentration), same rotational speed (1200 rpm) and wearing time (24 hours)

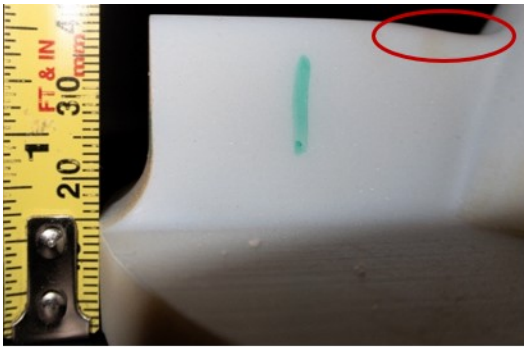


a) 1200RPM-5wt.%-24hours



b) 1200RPM-10wt.%-24hours

Figure 3.9. Pressure sides of the blades after different concentrations of solids (5% and 10% weight concentration), same rotational speed (1200 rpm) and wearing time (24 hours)



a) 1200RPM-5wt.%-24hours



b) 1200RPM-10wt.%-24hours

Figure 3.10. Suction sides of the blades after different concentrations of solids (5% and 10% weight concentration), same rotational speed (1200 rpm) and wearing time (24 hours)

### 3.3 Degradation of solid particles

The solid particles degraded as the time went on. The degree of degradation differed based on the experimental conditions. Figure 3.11 shows the erodent after 24 hours of wear at different rotational speeds with 5wt.% of solids. The garnets still had sharp edges at the 1200 rpm rotational

speed while they had the almost round edge at the 1750 rpm rotational speed. A slurry replacement interval should be considered when pumps run at high speed.

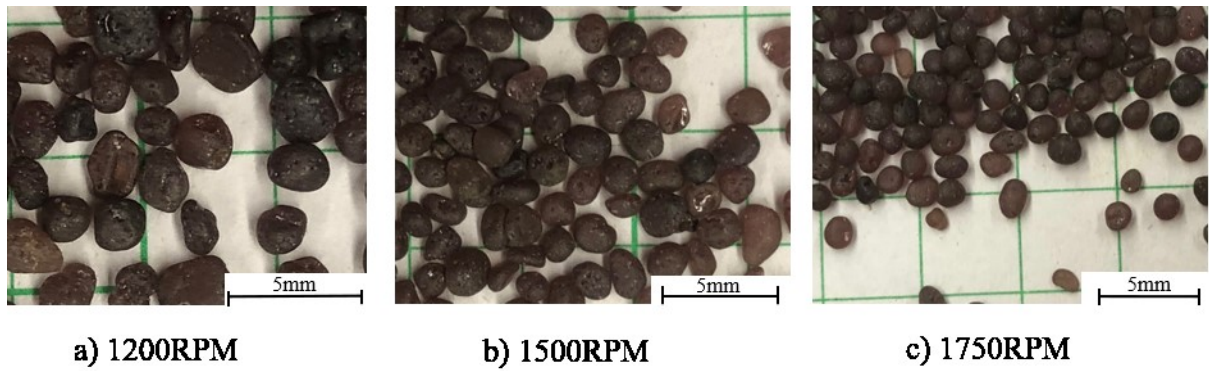


Figure 3.11. Particle degradation

### 3.4 Relationship of mass loss and wear time

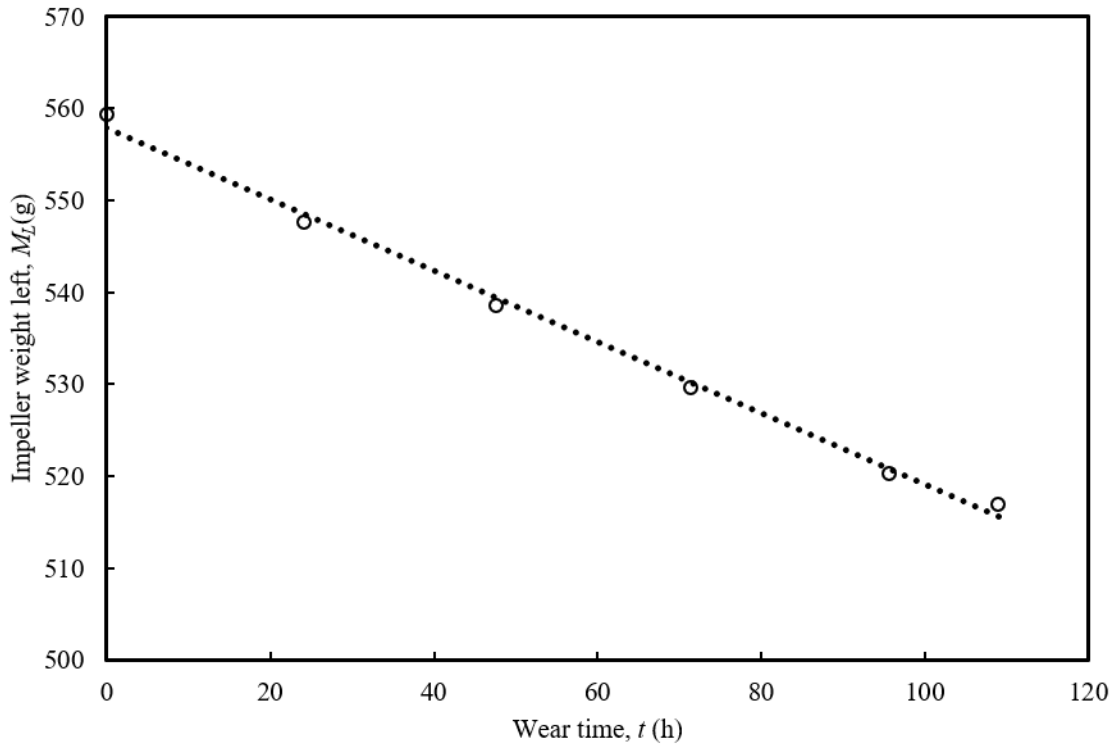


Figure 3.12. Mass loss vs. wearing time (1200 rpm and 5wt.% solid concentration)

Figure 3.12 shows the relationship between mass loss and wear time. The curve fitting line is described as:

$$m_L = -0.4t + 557.9 \tag{3.1}$$

The  $R^2$  value of this fitting is 0.9955. The sample was run for 110 hours and the slurry was changed around every 24 hours. The properties of the slurry were kept the same every time. The linear relationship curve fitting was performed on the data point. The data points lie almost in a straight line. Some points slightly deviate, which means that the relationship between mass and time is exponential. The slopes between the two points became smaller throughout the experiment. The wear rate is the physical manifestation of the slope between two points. Studies have shown

that wear rate decreases with time. To simplify the calculation of the wear rate, the relationship between mass loss and time is regarded as linear. This makes it possible to calculate the wear rate as mass loss divided by wear time.

### **3.5 Effects of bulk velocity on wear**

Each wear test in this part of the study was performed for 24 hours with the same size distribution of the garnets. Two different particle concentrations were used: 5% and 10% (by weight). Different rotational speeds (i.e., 1050 rpm, 1200 rpm, 1350 rpm, and 1750 rpm) were used. From Figure 3.13, it is clear that at two different concentrations, the wear rate increased with an increase in the flow rate. In these two cases, the results had a power law relationship. The exponents of the two cases were 2.9403 and 2.5152 for the solid concentration of 5% and 10% (by weight), respectively.



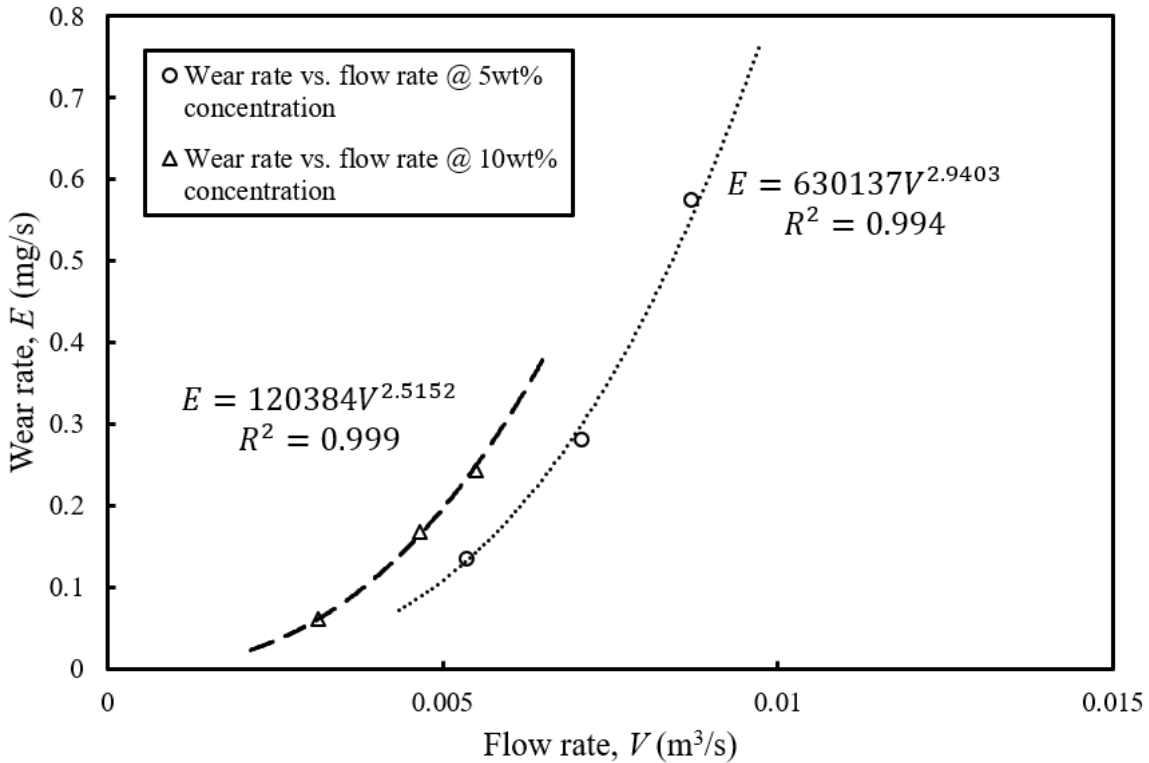


Figure 3.13. Wear rate vs. flow rate with different concentrations (5wt.% and 10wt.% concentration)

### 3.6 Effects of flow concentration on wear

The experiments were also conducted for 24 hours for two different rotational speeds (1050 rpm & 1200 rpm) for the erodent with the same size distribution. Three different weight concentrations (5%, 10% and 15%) were applied in the experiment. From Figure 3.14, it is obvious that the wear rate increased as the solid concentration increased. A power relationship curve fitting was also performed on the data series. The exponents of 1200 rpm and 1050 rpm were 0.5168 and 1.4567, respectively.

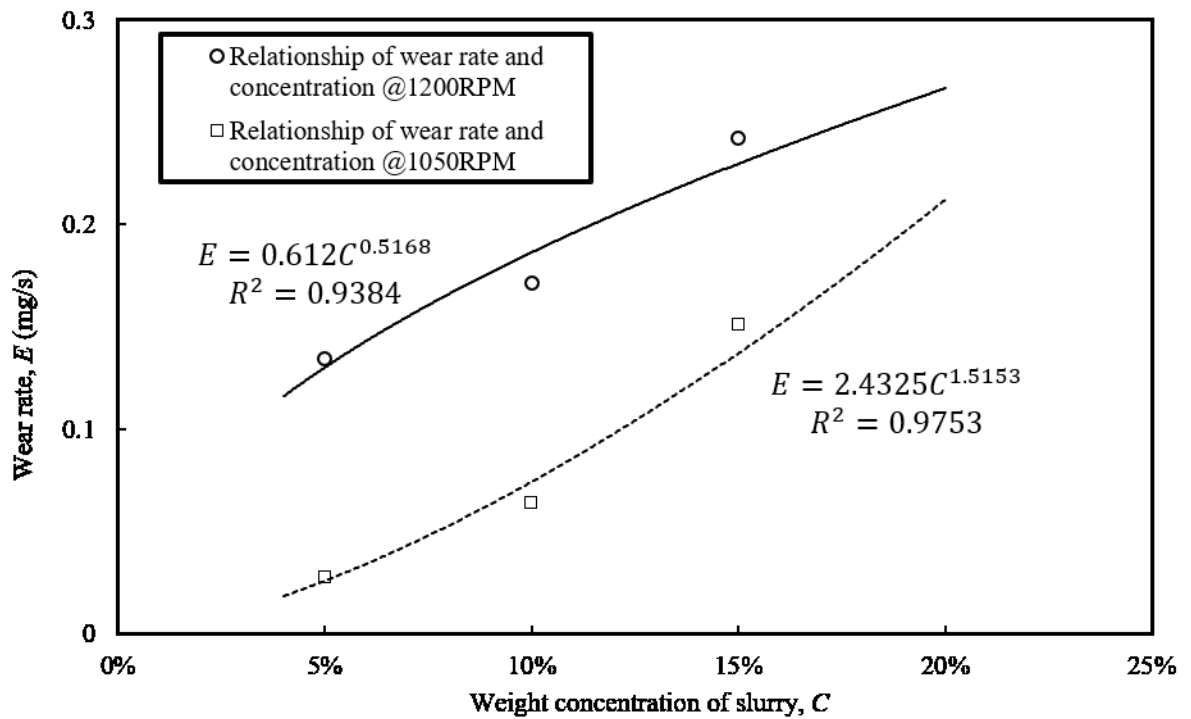


Figure 3.14. Wear rate vs. concentration with different rotational speeds (1050 rpm and 1200 rpm)

### 3.7 Head of pump affected by a worn impeller

The head flow capacity relationship is one of the important indicators of pump performance. Due to the limitation of the instrument, the pressure at the inlet and outlet sides of the pump was measured during the experiment. As mentioned in Chapter 2, the flow capacity/head experiments were performed before and after the wear testing.

Because there was too much head loss in the system, the maximum flow capacity for the loop in the lab could not achieve the maximum flow capacity provided by the manufacturer. Figures 3.15 to 3.24 show the head and flow rate relationship of different percentages of the samples' mass loss at different rotational speeds. The erodent was changed around every 24 hours.

The head of the pump reduced due to the increase in flow capacity. The maximum head often occurred at the low flow rate. The higher rotational speed had a higher head. The worn part of the impeller caused a decrease in the head. After comparing Figures 3.15 to 3.24, it should be noted that a higher percentage of mass loss did not cause the larger head loss. The original samples without damage often had the best curve fitting, but data about the other samples that sustained damage are chaotic. When the rotational speeds were relatively low (i.e., 850 rpm, 950 rpm and 1050 rpm), the 5.31% mass loss of the samples had the greatest head loss. When the rotational speeds were over 1050 rpm, the 7.617% mass loss of the samples had the most head loss. At these 10 different rotational speeds, 2.092% and 3.701% mass loss samples had less head loss.

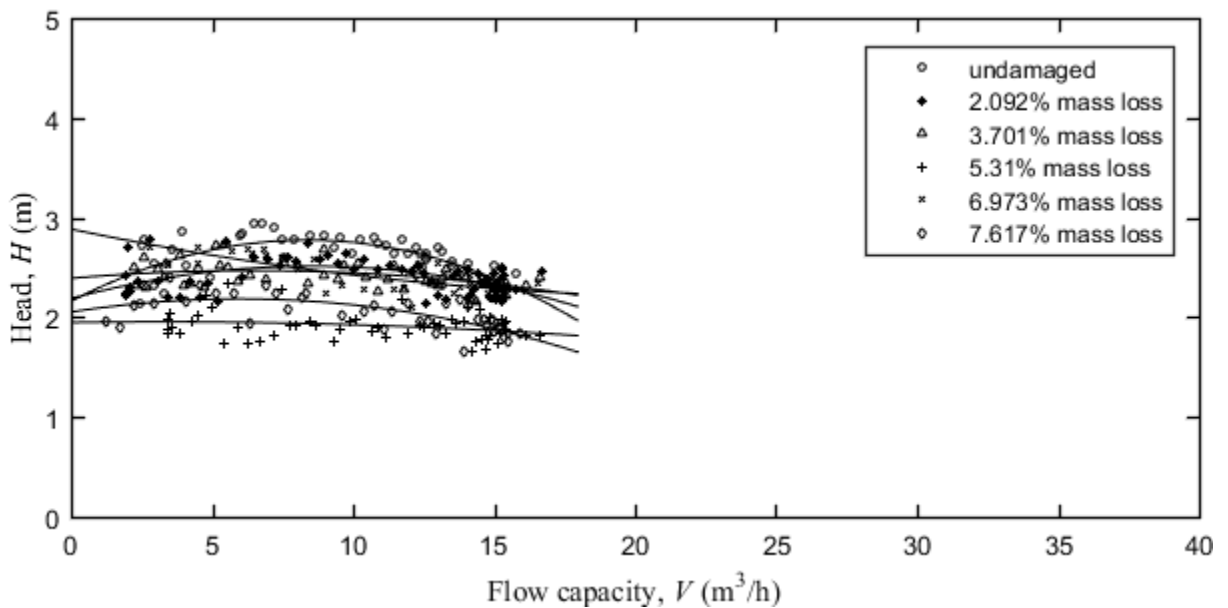


Figure 3.15. Head-flow rate relationship at 850 rpm with carried fluid (water) and different degrees of damage to the impeller

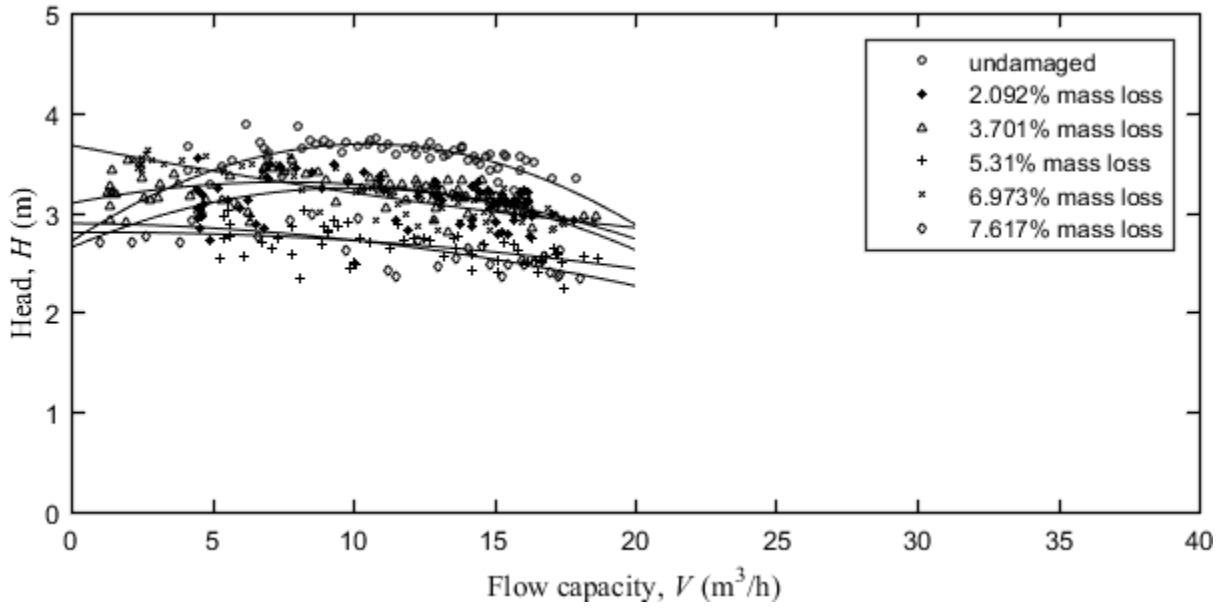


Figure 3.16. Head-flow rate relationship at 950 rpm with carried fluid (water) and different degrees of damage to the impeller

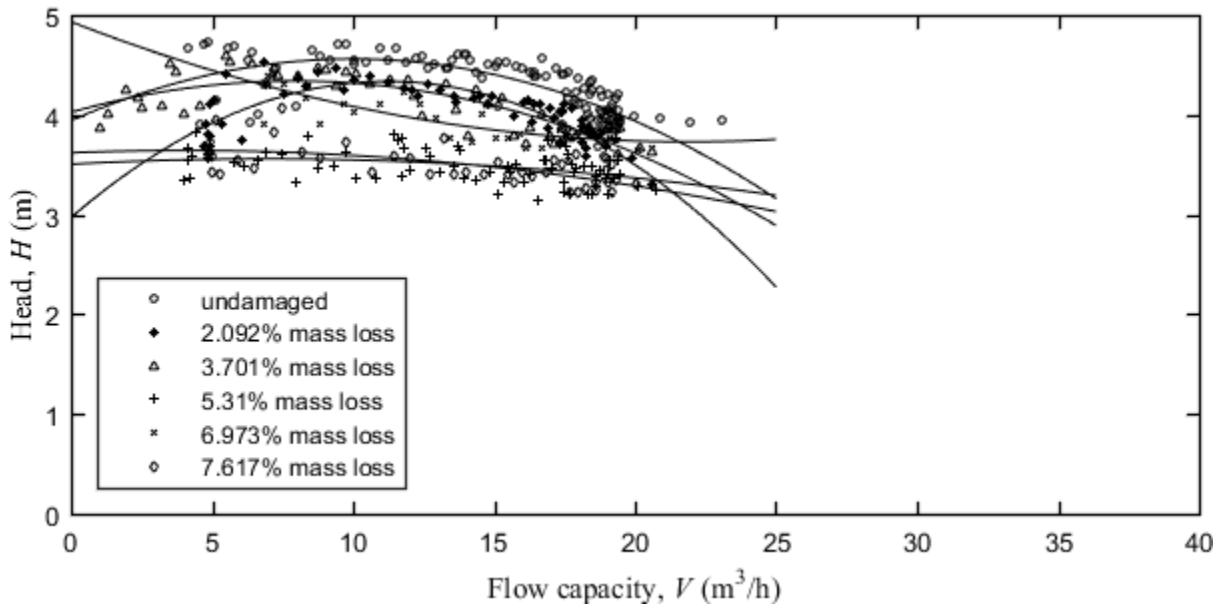


Figure 3.17. Head-flow rate relationship at 1050 rpm with carried fluid (water) and different degrees of damage to the impeller

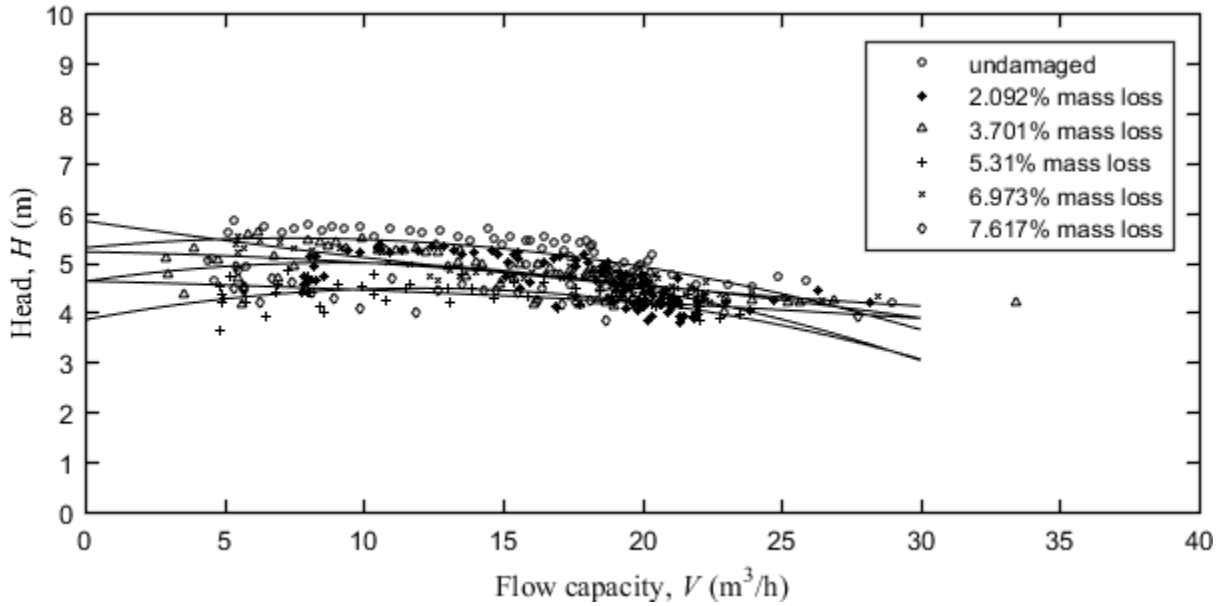


Figure 3.18. Head-flow rate relationship at 1150 rpm with carried fluid (water) and different degrees of damage to the impeller

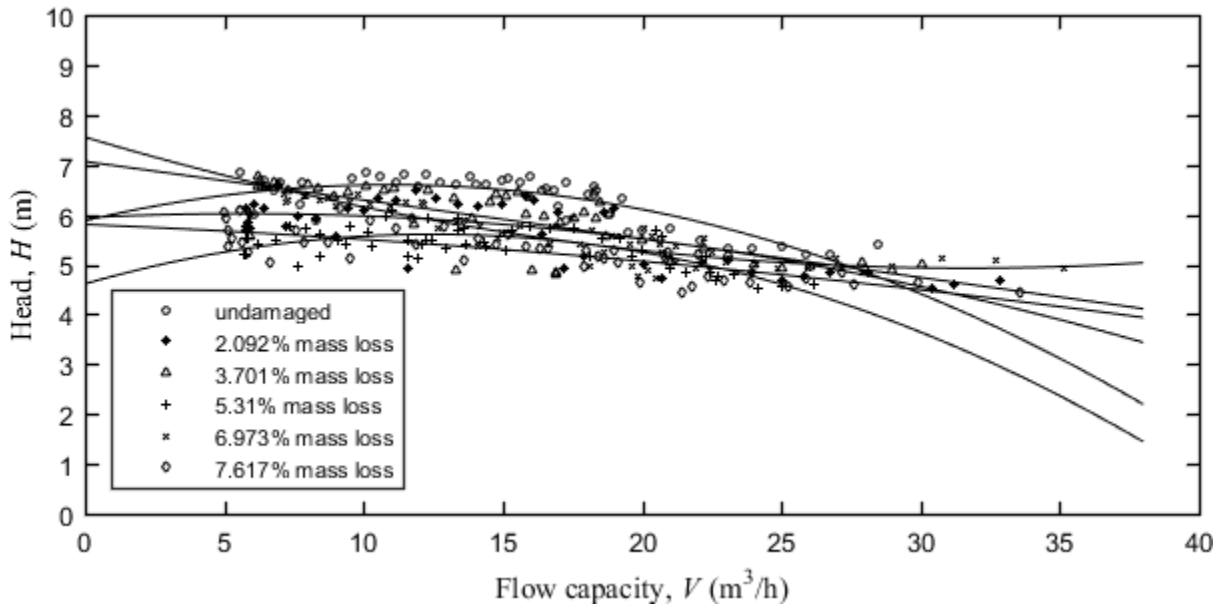


Figure 3.19. Head-flow rate relationship at 1250 rpm with carried fluid (water) and different degrees of damage to the impeller

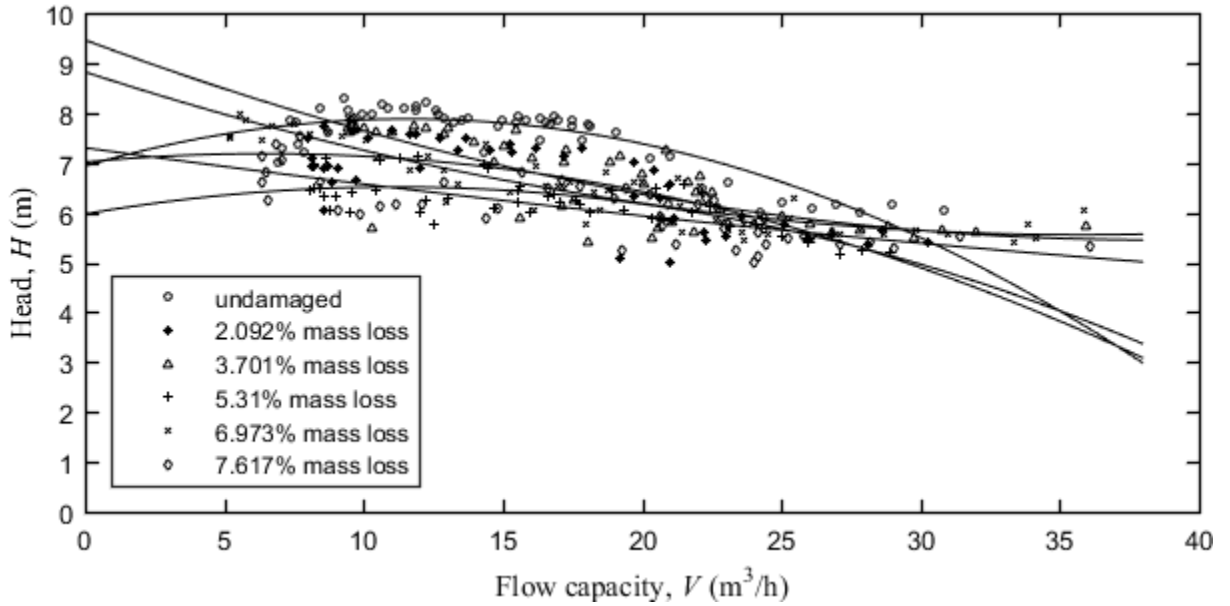


Figure 3.20. Head-flow rate relationship at 1350 rpm with carried fluid (water) and different degrees of damage to the impeller

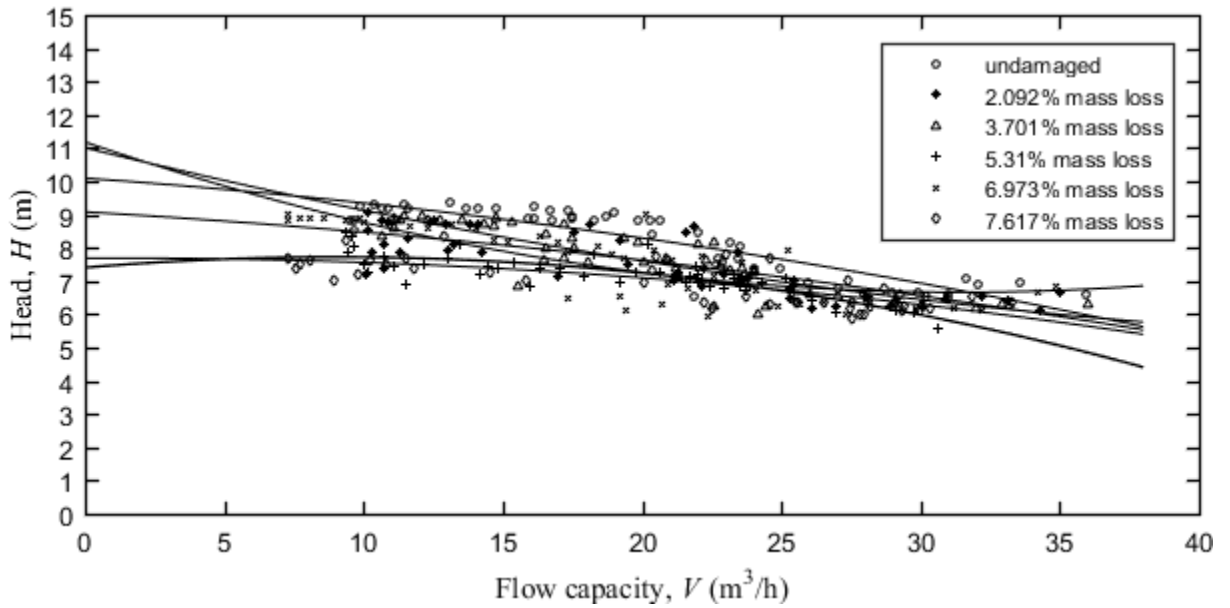


Figure 3.21. Head-flow rate relationship at 1450 rpm with carried fluid (water) and different degrees of damage to the impeller

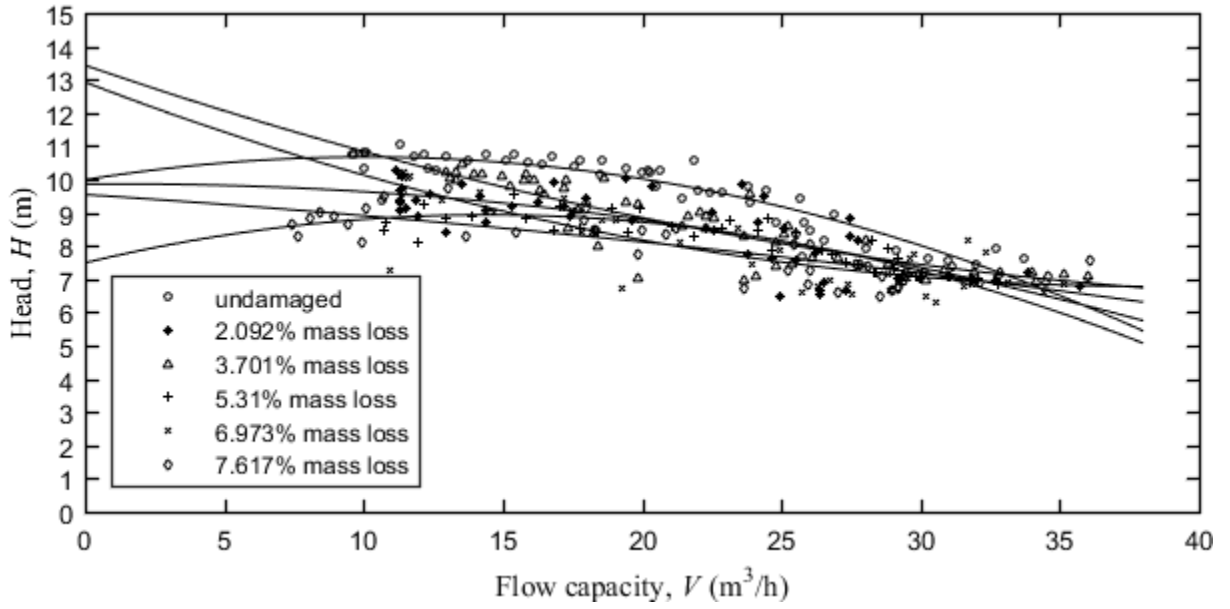


Figure 3.22. Head-flow rate relationship at 1550 rpm with carried fluid (water) and different degrees of damage to the impeller

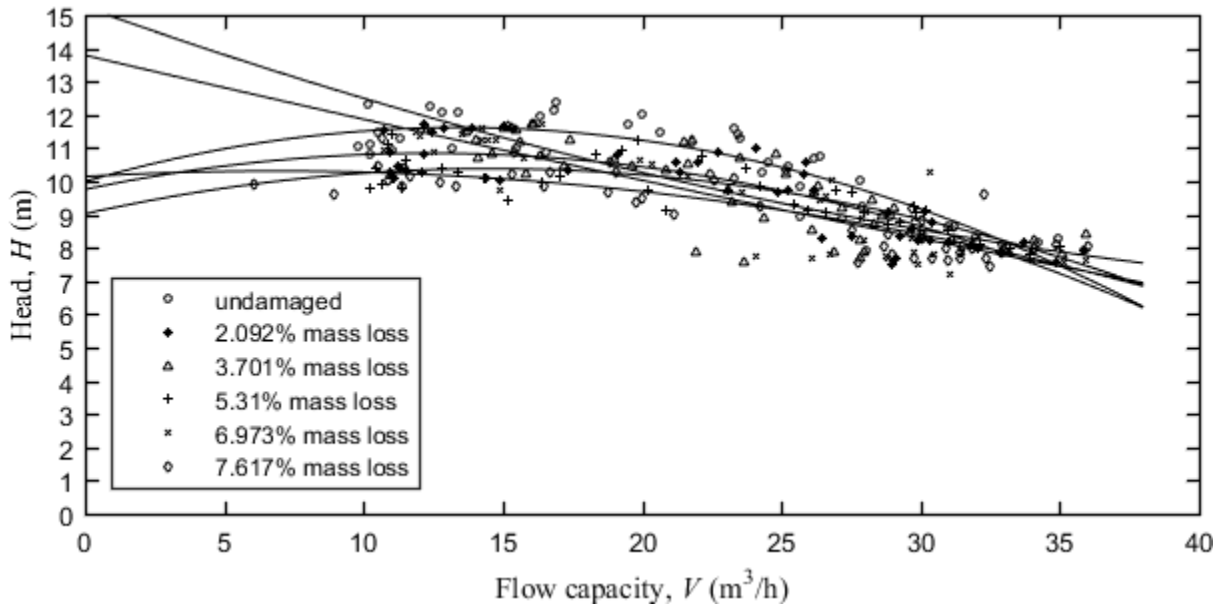


Figure 3.23. Head-flow rate relationship at 1650 rpm with carried fluid (water) and different degrees of damage to the impeller

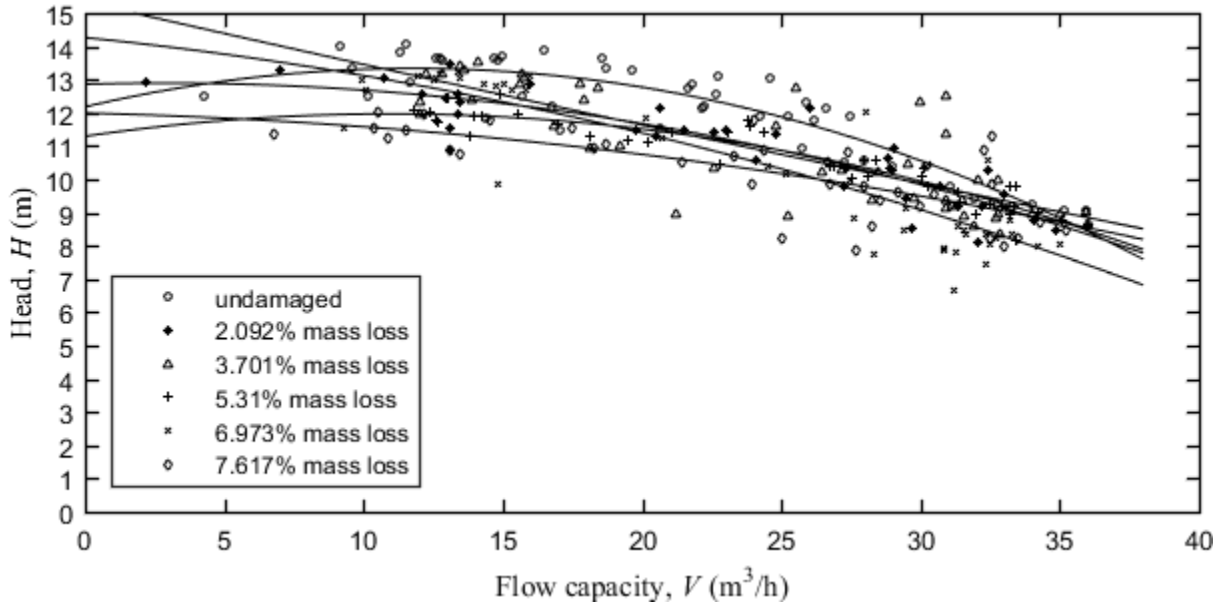


Figure 3.24. Head-flow rate relationship at 1750 rpm with carried fluid (water) and different degrees of damage to the impeller

In conclusion, this chapter presents experimental results obtained. Abrasion areas on the impeller are shown in the figures. Parametric studies on the flow rate and solid concentration were performed. The relationship between the head and capacity in the damaged impellers is also displayed. A detailed analysis of and discussion about the results will be presented in the next chapter.



## 4. Discussion

Chapter 3 showed the detailed results from this project. In this chapter, the discussions about the method and results will be presented.

### 4.1 Discussion about the method

The most novel idea in this project is that soft materials were used to build samples to give the experiments reasonable accelerations. In this project, the Verogray materials, which were often used in the Polyjet 3D printer in Stratasys Company, were finally used in the project. The manufacturing method was chosen for following reasons:

- 3D printing is highly developed, it is fast manufacturing, which can save the time to prepare the samples.
- Most 3D printers can use most 3D computer aided design (CAD) software directly, The printers are easy to build and convenient to modify. In some cases, it may be possible to skip the step of preparing 2D drawings for prototypes.

The materials should also be considered based on the materials normally used and the cost for sample materials. At first, we decided to use soft metal materials such as brass and aluminum, but the price for these metal materials are prohibitive, so the polymer was chosen. Verogray was selected because:

- Verogray materials are suitable for Polyjet technology. This type of printer has advantages including a high resolution and a homogeneous texture.
- The cost of Verogray materials is relatively cheap.

- The parts built using Polyjet technology do not have air gaps. No air gaps means that there is likely to be little error in mass loss.

There have been many investigations on wear behavior in a pump. Most methods used equipment to simulate the movement in the pump chamber. The results obtained using other methods will be compared with the results using the method in this project in Section 4.2. Unlike the Coriolis slurry erosion tester and pot tester, the method used in this thesis puts the impeller in a real heavy-duty pump, that is connected to the laboratory pipeline, The Coriolis slurry erosion tester and pot tester only simulate the movement of the slurry hitting the blades randomly. The effect of the properties of the slurry can be studied using the Coriolis slurry erosion tester and pot tester, but the samples in those methods were shaped as cuboids, which means the geometries of the impellers were ignored. A jet impingement tester was often applied in studies that looked at the effect of blade angles and other properties of the slurry. One of the limitations for the jet impingement tester is the same as that of the Coriolis erosion tester and pot tester, which is that factors of the geometry were not considered. In addition, the jet impingement tester did not show the particle motion in the pump well; the Coriolis erosion tester and pot tester did. A toriod wheel tester and pin-on-disc are often used to study the sliding erosion. They are suitable for studying erosion in a pipeline instead of the erosion of the impeller.

In conclusion, it is cost-efficient and time-efficient to use the sample made of polymer and replace the original metal impeller in the pump. This method is more accurate than others at predicting the wear behavior of the impeller because it used the same geometry model used in the manufacturer's impeller. Section 4.2 provides a discussion about the results obtained from this method along with results from previous studies performed by other researchers using other methods.

## **4.2 Discussion about the results**

### **4.2.1 Discussion about the wear pattern**

In this project, the most worn spot is on the upper sides of the blades near the hub. The width of the front blades drastically decreases during the wearing process, while the hub and back blades do not have noticeable damage. Li (2011) had similar results because the region near the hub had maximum shear stress and particle impact. The blades underwent different degrees of damage as the wear process continued, depending on their location. In the beginning, the upper edges of the blades near the hub experienced abrasion. Then the upper edges at the end of the blades began to experience abrasion. Eventually, the width of the lower edges at the end of the blades decreased apparently. According to Kruger (2010), a shock-like pattern often occurs at the leading edge, and a friction-like pattern occurs at the trailing edge. The patterns on our samples were similar to what Kruger described. Also, comparing Figures 3.2-3.4 and 3.8-3.10, when the rotational speed increased from 1200 rpm to 1750 rpm, the height reduced around 5mm; however, when solids concentration increased from 5wt.% to 10wt.%, the height slightly decreased. Therefore, the effect of the flow rate was more significant than the effect of the concentration. The suction sides of the blades had more abrasion than the pressure sides. More specifically, the pressure sides of the blades did not have visible wear patterns. This phenomenon is consistent with the results of studies by Metha (2007) Zhang (2016) and Li (2011). From Mehta (2007) the explanation is that the suction sides of the blades have maximum fluctuation in kinetic energy and random impingement. Ojala et al. (2015) tested rubber materials using 8-10mm granite gravel. Comparing Ojala's results on wear surface of rubber to my results, it is found that wear surface of samples in this project is similar with those in their results, which are both smooth and no lips

peeling off. Besides, Noon et al. (2016) found that large particles tend to be susceptible to sliding wear not impact wear. Zhong et al. (1996) also have a similar conclusion, which is that smaller particles tend to have more cutting wear and larger particles tend to have deformation wear.

In conclusion, the abraded regions on the impellers are similar to those seen in previous studies. However, due to the different properties between metals and polymers, the worn surfaces in this project (polymer) are relatively smooth. The reason why this phenomenon happened is that the polymer enlarged the effect of local deformation and new surfaces continuously are created on the other side where are not abraded. Large particles will cause more sliding wear than impact wear. Metal materials also experience this effect, but it is hard to observe that because of high hardness. Metal impellers from manufacturers used for a long time exhibited pits and fatigue on the surface, which was not observed using the present polymer impeller.

#### **4.2.2 Discussion about parametric studies**

Parametric studies were performed on the effect of concentration and flow rate. Based on the wear model proposed by Roco (1984), Gupta (1995), Elkholy (1983) and Ravichandra (2004), flow velocity and concentration have a power law relationship with the wear rate. One of the differences between these wear models is the exponents of the factors that affect the wear rate.

Recalling the parametric studies performed in Section 3.5 and 3.6, Table 4.1 shows the relationship between flow rate and wear rate at different concentrations. Table 4.2 shows the relationship between concentration and wear rate at different rotational speeds are presented.

Table 4.1. Relationships between flow rate and wear rate at solids concentration 5wt.% and 10wt.%

Conditions	Relationship
5wt.% solids concentration	$E = 630137V^{2.9403}$
10wt.% solids concentration	$E = 120384V^{2.5152}$

Table 4.2. Relationships between solid concentration and wear rate at rotational speed 1200 rpm and 1050 rpm

Conditions	Relationship
1200 rpm	$E = 0.612C^{0.5168}$
1050 rpm	$E = 2.4325C^{1.5153}$

Table 4.3 shows the comparison between exponents in my study and those in previous studies. From Table 4.1, the exponents of flow velocity in this project are 2.5152 and 2.9403, which are larger than the exponents of the wear models for brass and mild steel (2.4882 and 2.148 respectively) (Gupta, 1995). The exponents in this project are also larger than the wear model for hard materials (Elkholy, 1983). The explanation for these results is that the polymer is softer than the metal. Pool (1986) found that for the exponent of a ductile polymer in the velocity is two to three and for a brittle polymer it is three to five Roy et al. (1993) also claimed that the wear rate of the polymer composites had a higher order of magnitude than that for metallic materials. Based on this evidence, the results are reasonable and follow similar trends compared to harder, more typical, pump material. In this project, six groups of data were obtained; obviously more tests would result in more conclusive results, but the number of tests performed is enough to demonstrate the similarity and the value of this testing approach. In conclusion, the exponents of

velocity show reasonable agreement with Gupta et al. (1995), Elkholy et al. (1983), Pool (1986) and Roy et al. (1993).

From Table 4.2, the exponents of the concentration are 0.5168 and 1.4567. In Table 4.3, one of the exponents in my study is a little smaller than the exponents for concentration in Gupta's wear models for brass and mild steel while another is larger. Similarly, one of the exponents in our project is larger than the exponent in Elkholy's model (1983) while another is smaller. Theoretically, the exponents for the concentration of the polymer should be larger than the metal. One of the reasons for this problem is an error in the experiment. In this work, the solid concentration was deemed as uniform everywhere in the whole pipe loop, however, the concentration in the loop is fluctuate all the time. Besides, the aggregation of solid particles may have influence on the true solid concentration.

The results in this project also show that the velocity dominates the wear rate. When the flow velocity changes a little, the width and height of the blades change significantly. From the quantified aspect, the exponents of velocity are three or four times as great as the exponents of concentration in the wear rate math model.

Table 4.3. Comparing the exponents in this work to those in previous studies

Authors of previous studies & materials they used	Exponents of velocity	Exponents of concentration
Gupta et al. (1995):		
Brass	2.4882	0.516
Mild steel	2.148	0.556
Elkholy (1983):		
Cast iron	2.39	0.682
Pool et al. (1986):		
Ductile polymer	2-3	---
Brittle polymer	3-5	
This work:		
Verogary	5wt. %: 2.5152 10wt. %: 2.9403	1200rpm: 0.5168 1050rpm: 1.5153

The unit of the wear rate is mg/s. The reason why I did not use volume loss is that it is difficult to accurately measure volume loss due to the irregular shape of the impeller. If the instrument allowed, the volume loss could measure the volume using a high precision instrument such as a laser scanning arm. Mass loss was calculated by mass before wear minus mass after wear. The duration of the experiments was used as the wear time. This method may add errors because mass loss did not change in a linear relationship. Detailed information was given in Section 3.4. As shown in Figure 3.12, the wear rate decreased as time went on. This occurred due to the change

in the shape of the impeller and the particle degradation effect. However, to simplify the calculation of the wear rate, the wear rate was deemed as linear.

In parametric study, solid concentration was regarded as uniform in the whole pipeline and flow rate is average of the flow rate in a period of time, which is not accurate. Actually, there is significant fluctuation in flow rate and solids concentration. More data should be collected in different location of the pipe line. Tomography is an easy way that can accurately obtain the properties of the slurry flow. Densitometer is a common device. With these devices, the change of particles' movements should be considered.

The effects of particle size distribution and hardness of the target material and erodent material were not investigated. These factors also have an important influence on the wear rate. If exponents of particle size can be obtained, it is possible to correct coefficient  $K$  using Elkholy (1983)'s functional relationship. In future research, the parametric studies on these factors should be considered.

### **4.2.3 Discussion about results of H/Q experiments**

The damaged impellers will affect pump performance. In this project, the change in the head of the pump was discussed. The change in efficiency is not discussed. Figures 3.15-3.24 tend to show that the head of the pump decreased with an increase in the flow rate over the peak value. This phenomenon occurred because there was probably circulation in the suction side, which may have lowered the efficiency. In addition, circulation in the volute or near the impeller will affect the head at the discharge side (Karassik, 1987). Therefore, it is good to operate this kind of pump at a relatively high rotational speed because that way of circulation at the suction side or in the volute of the pump can be avoided. Looking at the head-capacity curves at different rotational



speed of the pump, it is noted that the head increases when the rotational speed increases. The data points can be fit by a parabolic relationship given by:

$$H = AQ^2 + BQ + C \quad (4.1)$$

Where  $A$ ,  $B$  and  $C$  are the coefficients that depend on the rotational speed and mass loss of the impeller. Of course, not all of the measured data resulted in obvious families of parabolic curves, but this chosen function is simple and is a typical shape for pump performance maps.

Imposing the parabolic fit on the data, the values of the  $A$ ,  $B$  and  $C$  were calculated (using least squares) and listed in Table 4.3. Without fixing any coefficients, there is not obvious law that can be concluded. The only thing noted is that the curve fitting for the data points of the undamaged impeller is the best, while the points of other damage conditions were not fit curves as well as those of undamaged condition.

Table 4.4. The values of  $A$ ,  $B$  and  $C$  for different rotational speeds and damage conditions without fixing any coefficients

Rotational speed	Percentage of mass loss	A	B	C	R-square
850 rpm	0	-0.0088	0.1468	2.1616	0.9959
	2.092	-0.0045	0.0766	2.1882	0.9785
	3.701	-0.0019	0.0239	2.3920	0.9703
	5.31	-0.0006	0.0041	1.9481	0.9900
	6.973	0.0013	-0.0587	2.8845	0.9869
	7.617	-0.0037	0.0442	2.0537	0.9925
950 rpm	0	-0.0089	0.1868	2.7086	0.9967
	2.092	-0.0061	0.1207	2.6481	0.9834
	3.701	-0.0037	0.0561	3.0923	0.9935

	5.31	-0.0010	0.0021	2.8003	0.9889
	6.973	0.0006	-0.0541	3.6744	0.9744
	7.617	-0.0014	-0.0023	2.8918	0.9864
	0	-0.0062	0.1239	3.9416	0.9994
1050 rpm	2.092	-0.0108	0.2434	2.9696	0.9823
	3.701	-0.0050	0.0791	4.0254	0.9838
	5.31	-0.0011	0.0155	3.5050	0.9949
	6.973	0.0025	-0.1101	4.9327	0.9629
	7.617	-0.0014	0.0113	3.6195	0.9790
	0	-0.0036	0.0523	5.2946	0.9821
1150 rpm	2.092	-0.0045	0.0819	4.6197	0.9931
	3.701	-0.0011	-0.0105	5.2141	0.9981
	5.31	-0.0044	0.1051	3.8509	0.9817
	6.973	0.0008	-0.0813	5.8307	0.9848
	7.617	-0.0004	-0.0144	4.6286	0.9900
	0	-0.0060	0.1317	5.8767	0.9866
1250 rpm	2.092	-0.0025	0.0281	5.9380	0.9878
	3.701	-0.00002	-0.0769	7.0630	0.9943
	5.31	-0.0064	0.1593	4.6109	0.9867
	6.973	0.0026	-0.1661	7.5514	0.9902
	7.617	-0.0007	-0.0233	5.8020	0.9858
	0	-0.0070	0.1630	6.9321	0.9920
1350 rpm	2.092	-0.0041	0.0529	7.0111	0.9906
	3.701	0.0027	-0.2091	9.4604	0.9950
	5.31	-0.0044	0.0974	5.9697	0.9960
	6.973	0.0026	-0.1827	8.8199	0.9892
	7.617	0.0004	-0.0770	7.2975	0.9882
	0	-0.0015	-0.0594	10.0934	0.9833
1450 rpm	2.092	-0.0012	-0.0493	9.0797	0.9777

	3.701	0.0018	-0.2061	11.0109	0.9874
	5.31	-0.0039	0.0705	7.4056	0.9944
	6.973	0.0046	-0.2873	11.1824	0.9933
	7.617	-0.0017	0.0046	7.6861	0.9988
	0	-0.0067	0.1359	9.9847	0.9952
	2.092	-0.0030	0.0079	9.8551	0.9673
1550 rpm	3.701	0.0029	-0.2879	13.4275	0.9910
	5.31	-0.0069	0.2002	7.4881	0.9950
	6.973	0.0042	-0.3215	12.9227	0.9890
	7.617	-0.0008	-0.0558	9.5411	0.9998
	0	-0.0090	0.2410	9.9950	0.9825
	2.092	-0.0071	0.1754	9.7585	0.9920
1650 rpm	3.701	0.0026	-0.3001	15.2426	0.9785
	5.31	-0.0064	0.1862	9.0226	0.9829
	6.973	0.0004	-0.1967	13.7897	0.9856
	7.617	-0.0036	0.0489	10.1421	0.9945
	0	-0.0083	0.1965	12.1782	0.9799
	2.092	-0.0041	0.0235	12.8596	0.9846
1750 rpm	3.701	0.0003	-0.1906	15.3319	0.9905
	5.31	-0.0056	0.1226	11.2943	0.9790
	6.973	-0.0029	-0.0851	14.2611	0.9834
	7.617	-0.0021	-0.0201	11.9913	0.9829

To clearly show the effect of the damaged impeller on the pump performance, refitting for the data points was performed by fixing the coefficient  $A$  and  $B$ . The fixed coefficient  $A$  and  $B$  was determined from the fitting function for the undamaged impeller. Coefficient  $C$  was allowed to vary depending on the impellers with different percentage of mass loss due to abrasion. Figures 4.2-4.11 show the refitting curves and comparing performance data in this project with those from

manufacturer. The pump head curves from manufacturer are higher than those in this work. For pumps with undamaged samples, head is lower than manufacturer's data. The drop in head at low flow rate is around 0.5m in each rotational speed when using polymer undamaged impeller. Head drop at maximum flow rate in high rotational speed (around 5m for 1750 rpm) is larger than that in low rotational speed (around 1m for 850 rpm). Increasing flow rate cause more head drop between manufacturer's data and this project's data. Damage conditions can also affect head drop. One possible reason for this phenomenon is that samples built by polymers may affect pump performance. Also, pipeline in this project have some head loss, which will cause the head in this project is lower than manufacturer's data. Other worn parts in the pump, such as pump casing and wear plate, may have influence on head drop.

Figure 4.1 shows the change in coefficient  $C$ . When refitting the head-capacity data points using the fixed coefficients  $A$  and  $B$ , the coefficients  $C$  of the undamaged impellers at different rotational speeds are larger than the coefficients  $C$  of the damaged impellers. The relationship between coefficient  $C$  and percentage of mass loss tends to be consistent except for the high rotational speeds (1650 rpm and 1750 rpm). Using the least squares regression method to combine two factors (the percentage of mass loss and rotational speed), the mathematical model of coefficient  $C$  was assumed, which is

$$C = aw + be^{cM_{percent}} \quad (4.1.)$$

Where  $a$ ,  $b$  and  $c$  are the coefficient depends on the impeller properties,  $w$  is the rotational speed with unit of rpm, and  $M_{percent}$  is the percentage of mass loss.

The value of coefficient  $C$  that used fixed coefficient  $A$  and  $B$  at each rotational speed case was listed in Table 4.4. Using the least squares regression method and combining two factors (percentage of mass loss and rotational speed), the math model was given by:

$$C = 0.01w - 7.23e^{1.30M_{percent}} \quad (4.2.)$$

The  $R$  square value is 0.9593, which is acceptable using this model.

Table 4.5. Coefficient  $C$  for different percentages of mass loss at different rotational speeds

	0	2.092%	3.701%	5.31%	6.973%	7.617%
850 rpm	2.1616	2.021	1.999	1.498	2.012	1.649
950 rpm	2.7086	2.313	2.423	1.852	2.448	1.917
1050 rpm	3.9416	3.62	3.707	3.102	3.558	3.1
1150 rpm	5.2946	4.844	4.925	4.417	4.987	4.454
1250 rpm	5.8767	5.405	5.541	4.915	5.353	4.985
1350 rpm	6.9321	6.105	6.339	5.691	6.326	5.835
1450 rpm	10.0934	9.421	9.529	8.918	9.423	8.969
1550 rpm	9.9847	8.965	9.168	8.786	8.859	8.622
1650 rpm	9.995	9.371	9.373	9.218	9.298	9.025
1750 rpm	12.1782	11.4	11.52	11.29	11.01	10.81

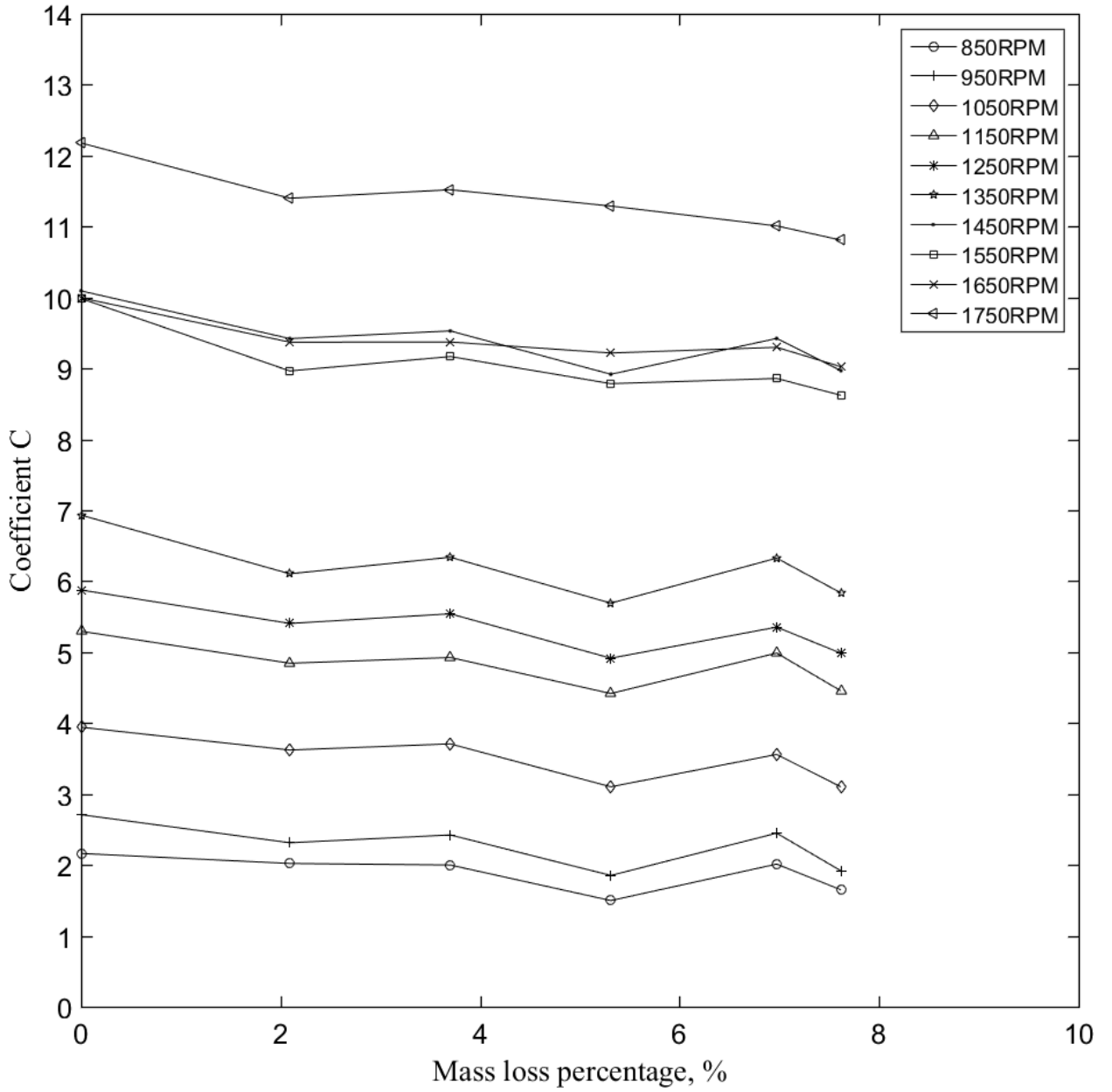


Figure 4.1. Coefficient  $C$  after refitting using fixed  $A$  and  $B$  that varied with different rotational speeds

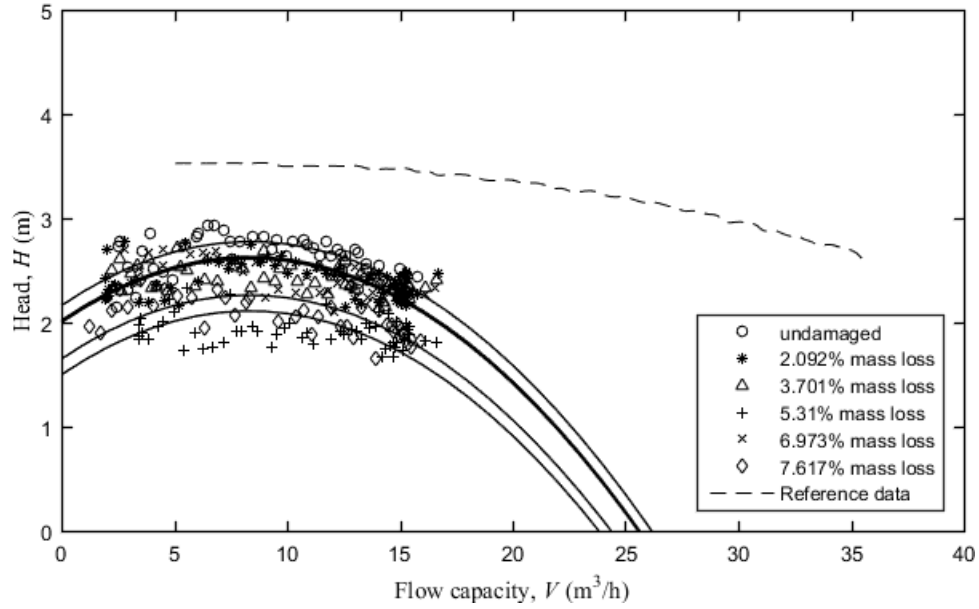


Figure 4.2. Head-flow rate relationship at 850 rpm with carried fluid (water) and different damage conditions after refitting using fixed  $A$  and  $B$  ( $A=-0.0088$ ,  $B=0.1468$ )

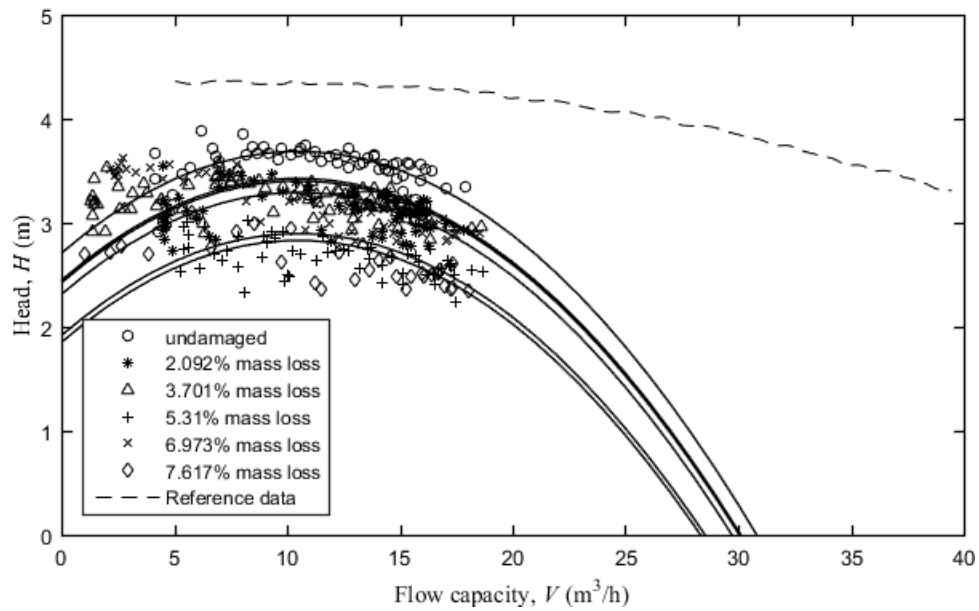


Figure 4.3. Head-flow rate relationship at 950 rpm with carried fluid (water) and different damage conditions after refitting using fixed  $A$  and  $B$  ( $A=-0.0089$ ,  $B=0.1868$ )

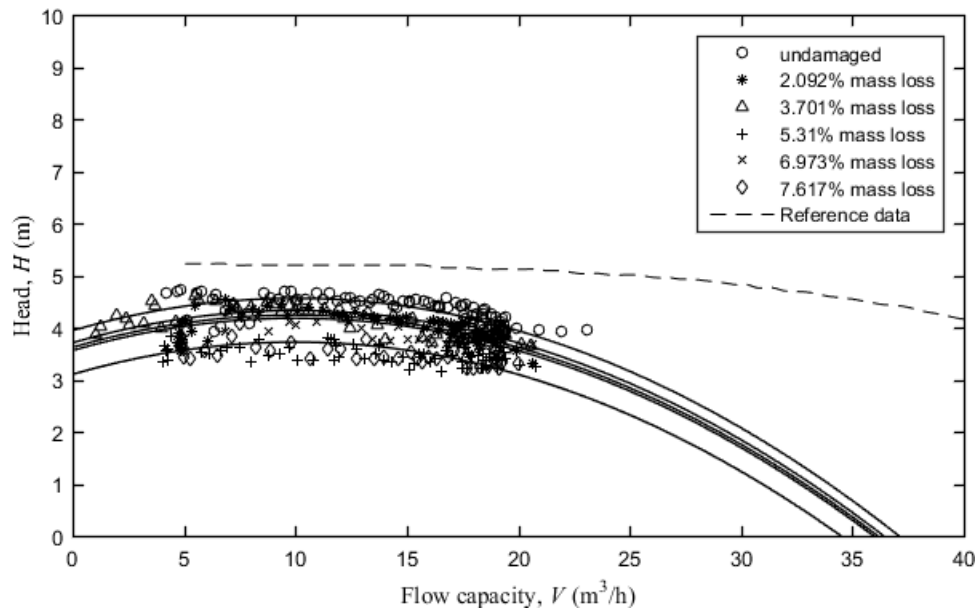


Figure 4.4. Head-flow rate relationship at 1050 rpm with carried fluid (water) and different damage conditions after refitting using fixed  $A$  and  $B$  ( $A=-0.0062$ ,  $B=0.1239$ )

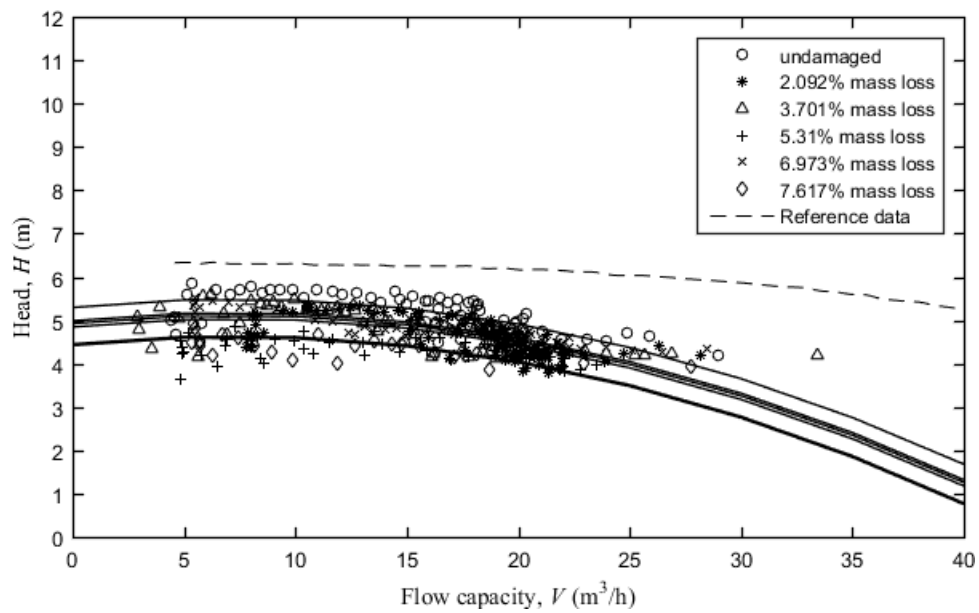


Figure 4.5. Head-flow rate relationship at 1150 rpm with carried fluid (water) and different damage conditions after refitting using fixed  $A$  and  $B$  ( $A=-0.0036$ ,  $B=0.0523$ )



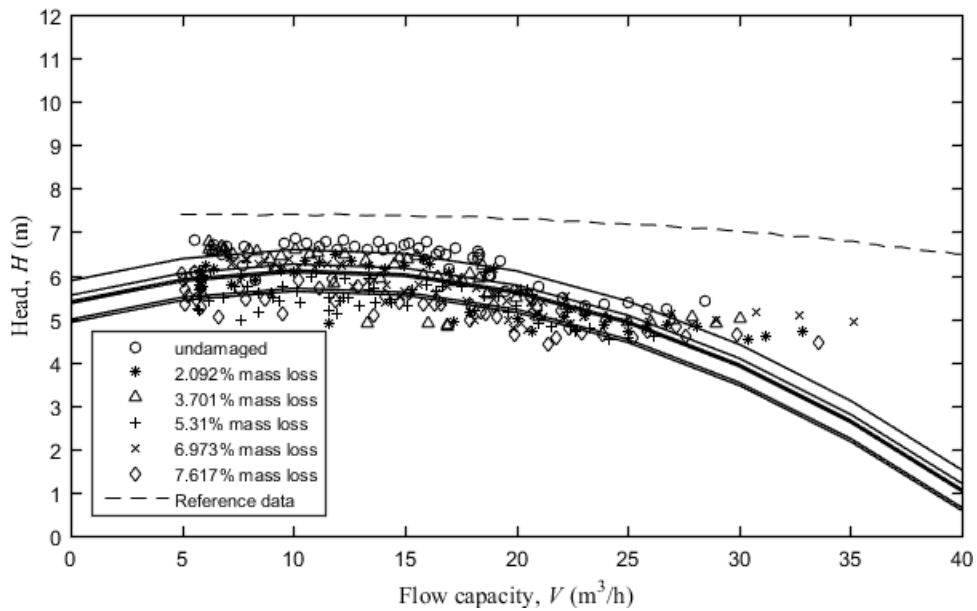


Figure 4.6. Head-flow rate relationship at 1250 rpm with carried fluid (water) and different damage conditions after refitting using fixed  $A$  and  $B$  ( $A=-0.006$ ,  $B=0.1317$ )

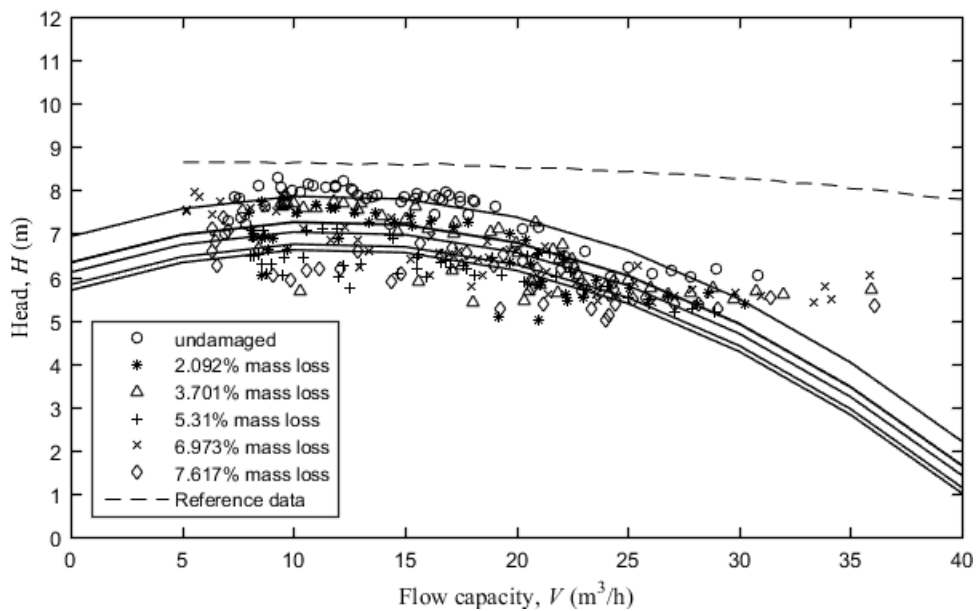


Figure 4.7. Head-flow rate relationship at 1350 rpm with carried fluid (water) and different damage conditions after refitting using fixed  $A$  and  $B$  ( $A=-0.007$ ,  $B=0.163$ )

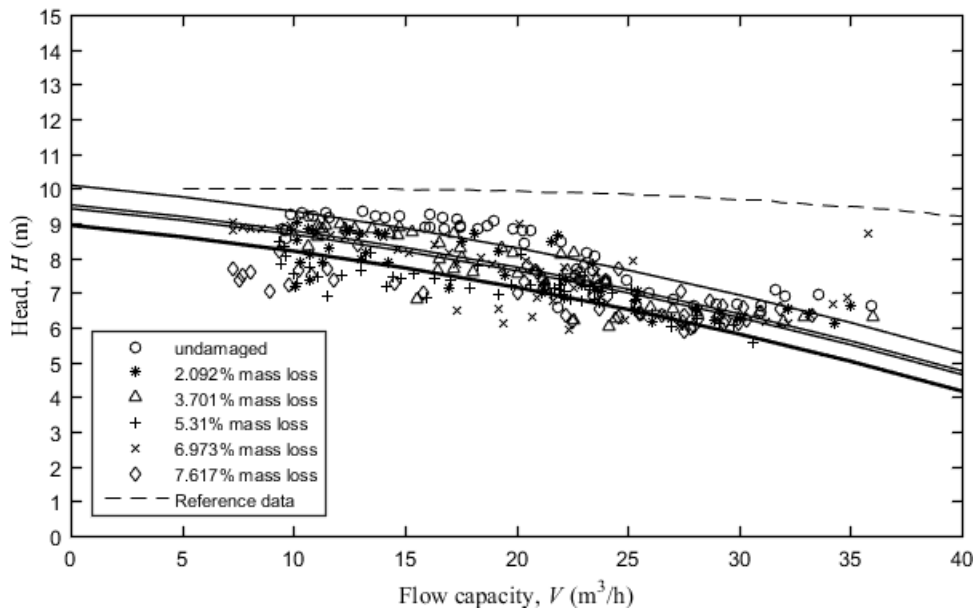


Figure 4.8. Head-flow rate relationship at 1450 rpm with carried fluid (water) and different damage conditions after refitting using fixed  $A$  and  $B$  ( $A=-0.0015$ ,  $B=-0.0594$ )

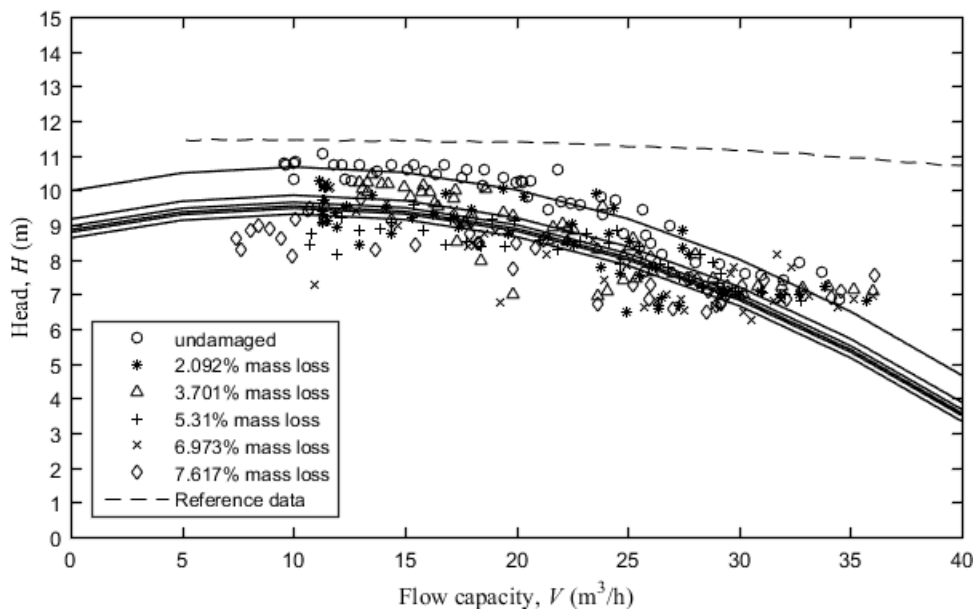


Figure 4.9. Head-flow rate relationship at 1550 rpm with carried fluid (water) and different damage conditions after refitting using fixed  $A$  and  $B$  ( $A=-0.0067$ ,  $B=0.1359$ )

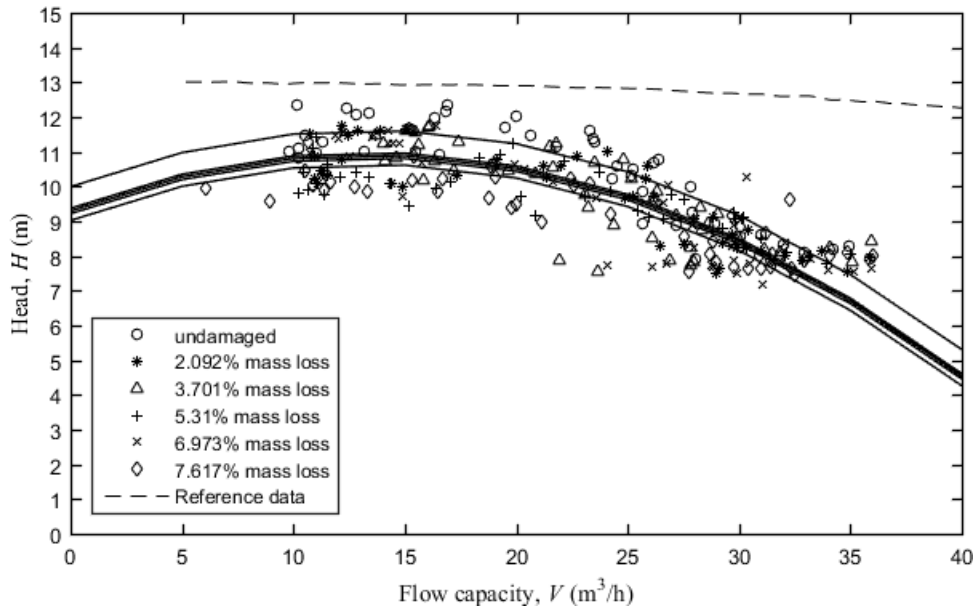


Figure 4.10. Head-flow rate relationship at 1650 rpm with carried fluid (water) and different damage conditions after refitting using fixed  $A$  and  $B$  ( $A=-0.009$ ,  $B=0.241$ )

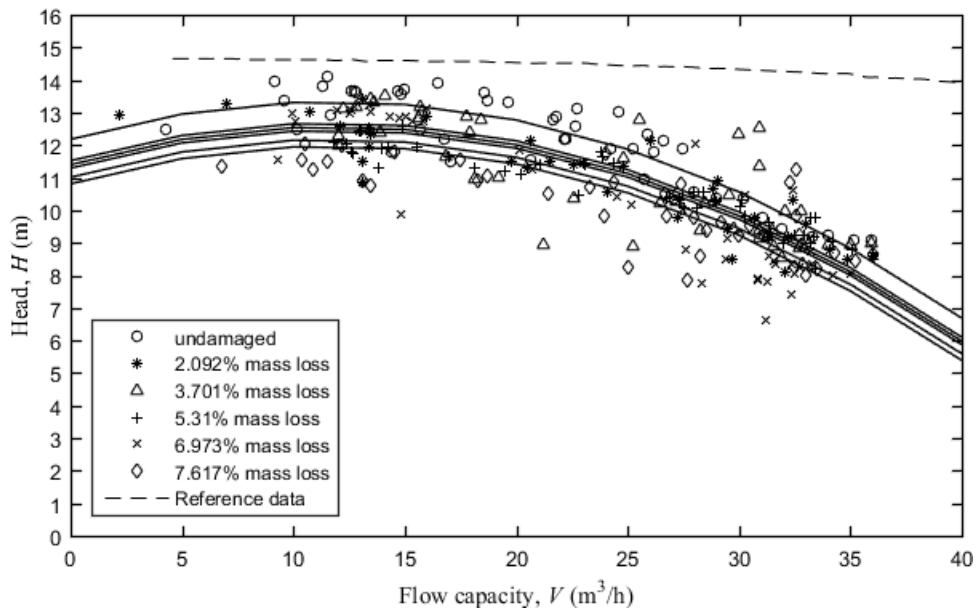


Figure 4.11. Head-flow rate relationship at 1750 rpm with carried fluid (water) and different damage conditions after refitting using fixed  $A$  and  $B$  ( $A=-0.0083$ ,  $B=0.1965$ )

To be more specific, instead of fitting a group of data of different rotational speed separately, it is better to fit all data points with the same  $A$  and  $B$  and allowing the coefficient  $C$  to vary by different damaged conditions and rotational speed. The coefficient  $A$  and  $B$  of 1350 rpm case was chosen, which is -0.007 for coefficient  $A$  and 0.163 for coefficient  $B$ . Figure 4.12 shows the change in the new coefficient  $C$  with the percentage of mass loss. Using the empirical model in Equation 4.1 to fit the new coefficient  $C$ , the mathematical model is:

$$C = 0.01w - 7.89e^{1.22M_{percent}} \quad (4.3.)$$

The  $R$  square value is 0.9872.

Both Figure 4.1 and 4.12 show the change in coefficient  $C$  with the different percentage of mass loss of impeller for different rotational speeds. When the mass loss less than 5.31%, the coefficient  $C$  decreases as mass loss increases, but when the mass loss is over 5.31%, for rotational speeds that lower 1550 rpm, the values of coefficient  $C$  larger than those for 5.31% mass loss, which is abnormal. Interestingly, the changes of these curves are similar. The reason for this anomaly is unknown for now. One possible reason is that high rotation speed may create more fluctuations in pressure, which will increase errors in results. More experiments related to different percentages of mass loss of impeller samples should be conducted in future study.

The relationship between coefficient  $C$  and the percentage of mass loss is clearer. In this case, the fitting lines tended to be parallel, which means that for the samples with the same percentage of mass loss, seemed to meet the affinity law for the same percentage of mass loss. The affinity law is assumed to be:

$$\frac{C_1}{C_2} = \left(\frac{w_1}{w_2}\right)^n \quad (4.4.)$$

$n$  is the exponent that depends on the different percentages of mass loss.

The average  $n$  was calculated for each case with a constant percentage of mass loss. The trend that shows the change in  $n$  with different percentages of mass loss is presented in Figure 4.13. The value of  $n$  tended to be in the range of 2.5-3. The  $n$  had a peak value at 5.31% mass loss. The values of  $n$  of undamaged, 2.092%, 3.701% and 6.973% were similar, at around 2.5. After comparing Figure 4.12 and 4.13, it is interesting to see that the trends for coefficient  $C$  and exponent  $n$  are opposite. The coefficient  $C$  decreased before reaching the peak point while the exponent  $n$  increased.

In conclusion, with the empirical model and affinity law of coefficient  $C$ , a method can be proposed to know the relationship of head and flow rate for different damage conditions. If performance curves of undamaged impeller are given, the coefficient  $A$  and  $B$  can be obtained with these data points. For a damaged impeller, the coefficient  $C$  can be determined by the empirical mathematical model (Equation 4.1) of a given impeller model. This method can be used to predict the relationship between head and flow rate for different damage conditions when designing the impeller model.

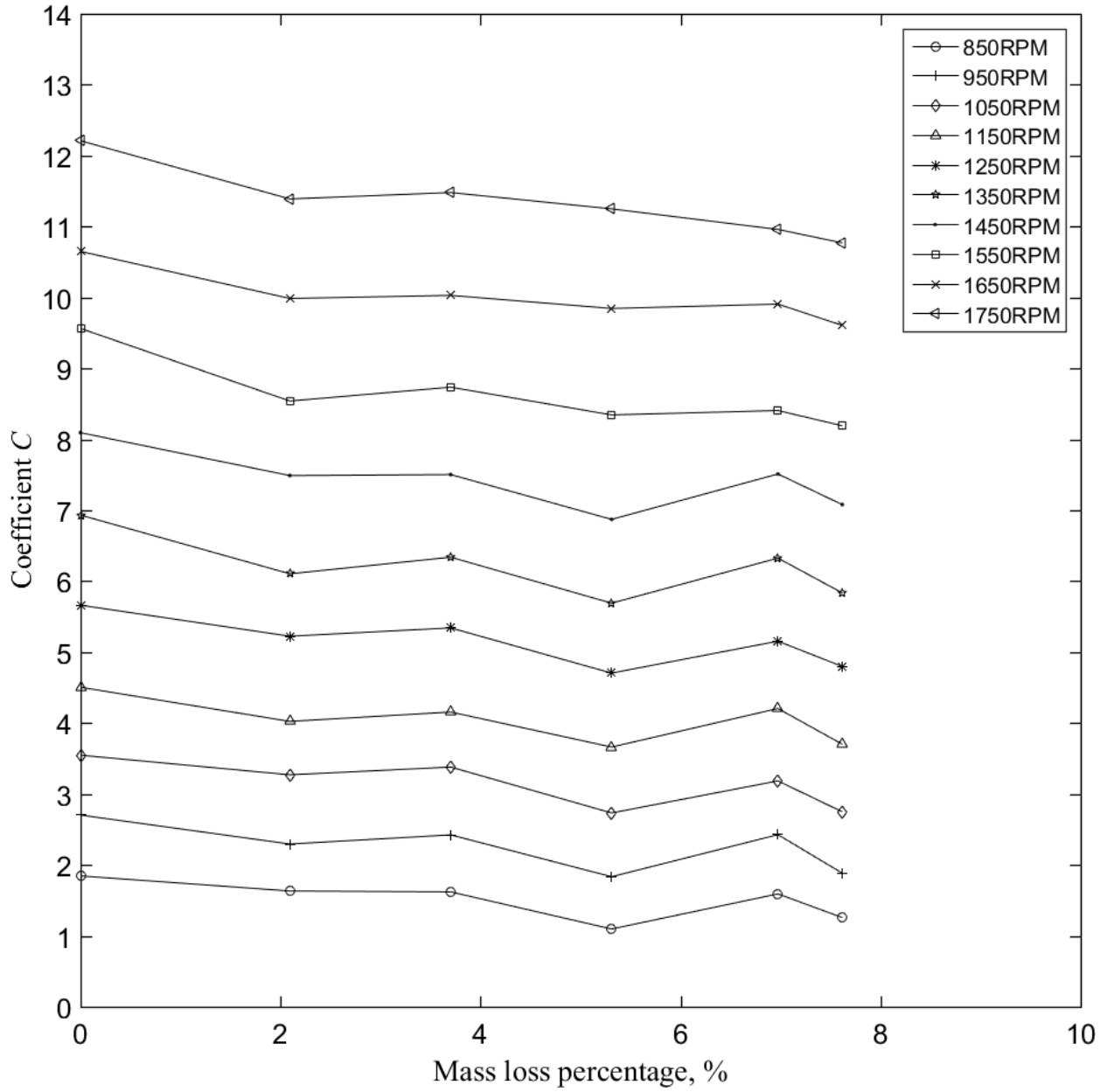


Figure 4.12. Coefficient  $C$  with the same coefficients  $A$  and  $B$  ( $A=-0.007$ ,  $B=0.163$ ) vs. percentage of mass loss

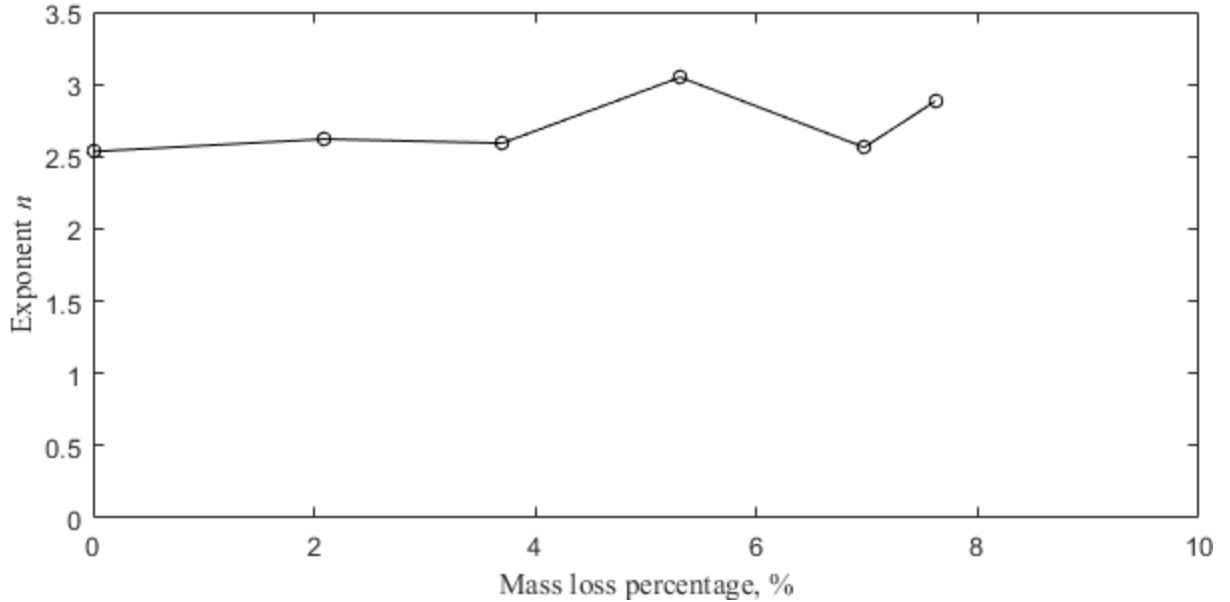


Figure 4.13. Value  $n$  vs. percentage of mass loss

To further analyze the effect of the different damage conditions, integrals of the refitting functions will be performed. It should be noted that the fluid power can be calculated by:

$$P = \rho_f g H Q \quad (4.5.)$$

Where  $P$  is the fluid power and the unit is  $\text{kgm}^2/\text{s}^2$ ;  $\rho_f$  is the density of fluid and the unit is  $\text{kg}/\text{m}^3$ ;  $g$  is gravitational acceleration and the unit is  $\text{m}/\text{s}^2$ ;  $H$  is the head and the unit is the meter;  $Q$  is the flow rate and the unit is  $\text{m}^3/\text{s}$ .

In this case, taking integrations of the head and flow capacity and multiplying them by the density of water and gravitational acceleration will give the fluid power. Figures 4.14-4.23 show the indefinite integrals for different rotational speeds and different damage conditions. From these figures, the power of undamaged impellers for each flow rate is the maximum among these six damaged conditions. Also, the largest mass loss of impellers did not always have the lowest power. When the rotational speeds were high (e.g., 1650 rpm and 1750 rpm), the differences in power

between the damaged impellers were small, but clearly still different from that of the undamaged impellers. The indefinite integrals were also conducted for different specific flow rate ranges that varied with different rotational speeds. Table 4.5 shows the flow rate ranges for different integration at different rotational speeds. The maximum flow rate for each integral was chosen based on maximum flow rate at that rotational speed. Figure 4.24 shows the change in fluid power for the specific flow rate with the percentage of mass loss. The trends that show the changes in power with different percentages of mass loss are almost the same as the trends for the changes in coefficient  $C$ . It seems that the relationships between fluid power and percentage of mass loss are similar especially when the rotational speeds are low, but the relationship at higher rotational speeds is not the same. Thus, this analysis shows that the fluid power of a specific flow rate highly depends on the coefficient  $C$ , and that coefficient  $C$  varies depending on the damage conditions.

Table 4.6. Flow rate ranges for definite integrals at different rotational speeds

Rotational speed (rpm)	Flow rate range (m <sup>3</sup> /h)
850	0-17
950	0-19
1050	0-23
1150	0-33
1250	0-35
1350	0-36
1450	0-36
1550	0-36
1650	0-36
1750	0-36



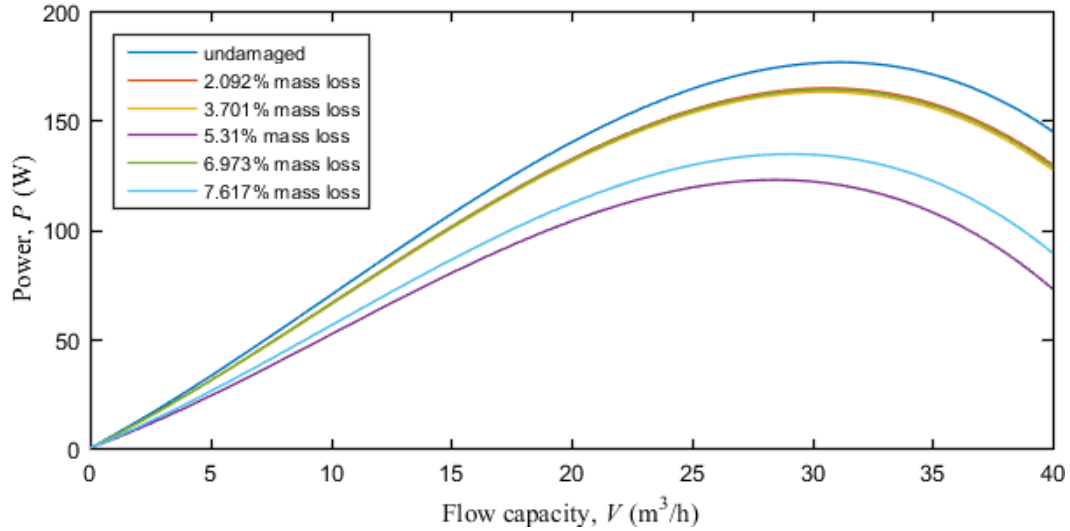


Figure 4.14. Power vs. flow capacity for different damage conditions (0%, 2.092%, 3.701%, 5.31%, 6.973% and 7.617% mass loss) at 850 rpm with carried fluid (water) ( $A=-0.0088, B=0.1468$ )

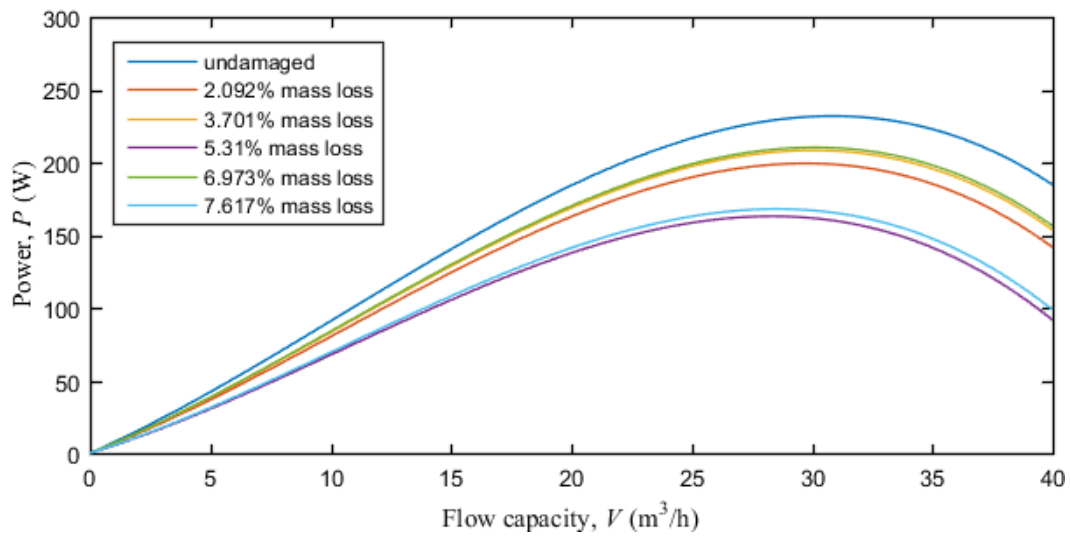


Figure 4.15. Power vs. flow capacity for different damage conditions (0%, 2.092%, 3.701%, 5.31%, 6.973% and 7.617% mass loss) at 950 rpm with carried fluid (water) ( $A=-0.0089, B=0.1868$ )

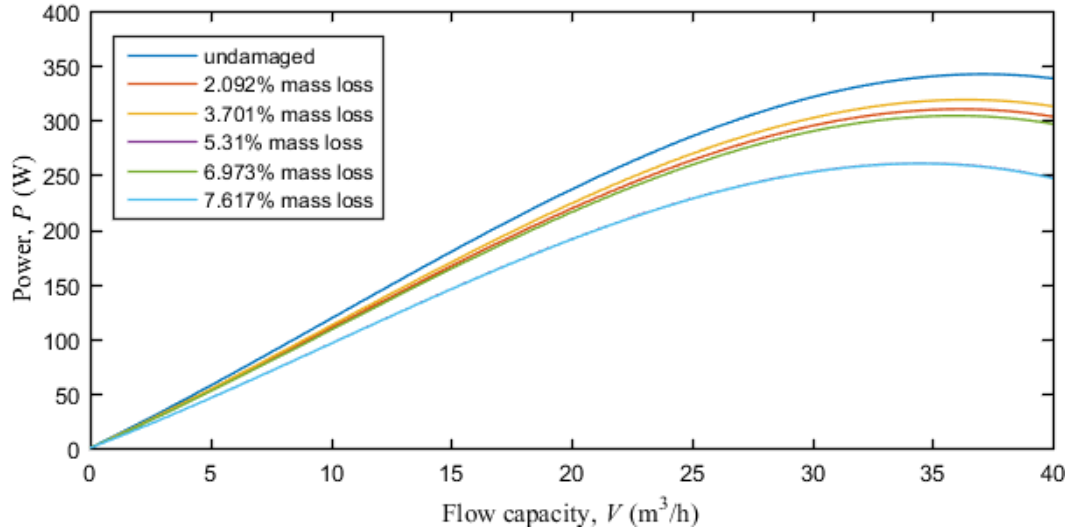


Figure 4.16. Power vs. flow capacity for different damage conditions (0%, 2.092%, 3.701%, 5.31%, 6.973% and 7.617% mass loss) at 1050 rpm with carried fluid (water) ( $A=-0.0036$ ,  $B=0.0523$ )

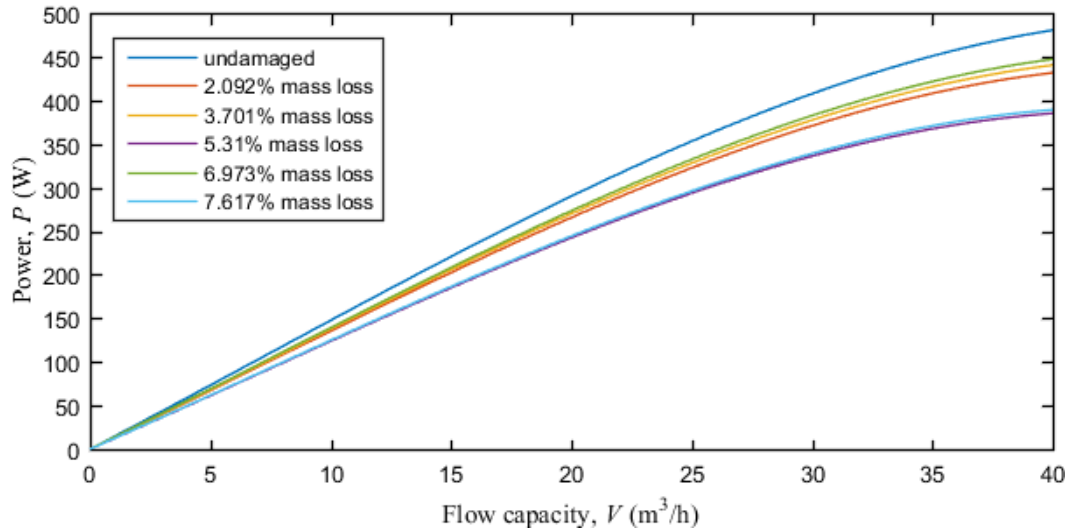


Figure 4.17. Power vs. flow capacity for different damage conditions (0%, 2.092%, 3.701%, 5.31%, 6.973% and 7.617% mass loss) at 1150 rpm with carried fluid (water) ( $A=-0.0036$ ,  $B=0.0523$ )

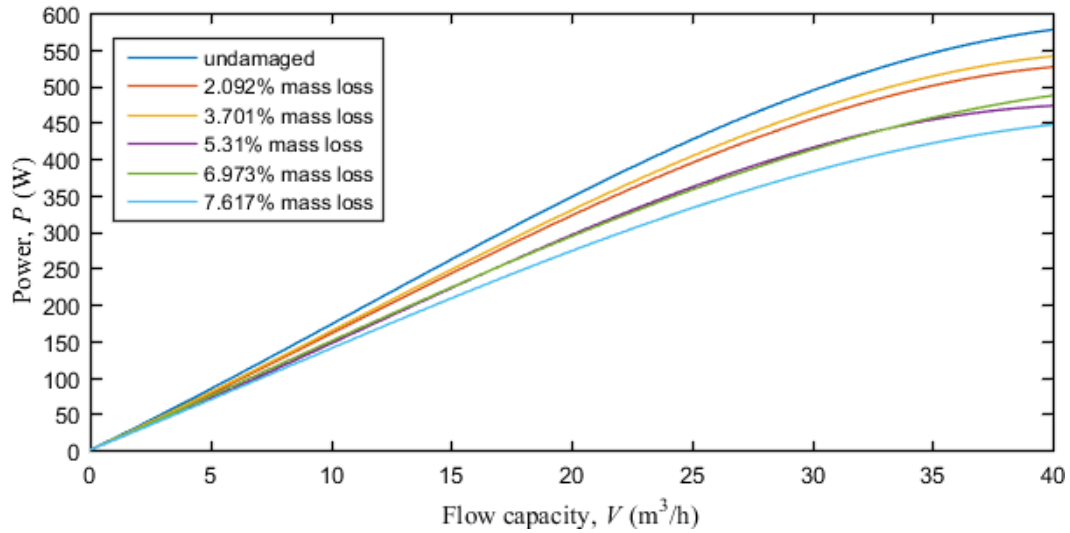


Figure 4.18. Power vs. flow capacity for different damage conditions (0%, 2.092%, 3.701%, 5.31%, 6.973% and 7.617% mass loss) at 1250 rpm with carried fluid (water) ( $A=-0.006, B=0.1317$ )

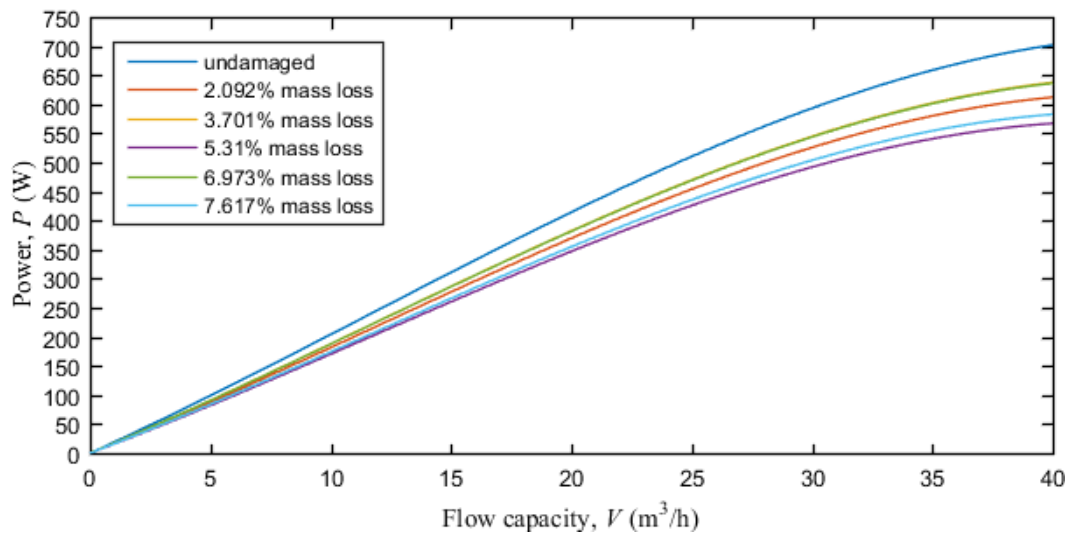


Figure 4.19. Power vs. flow capacity for different damage conditions (0%, 2.092%, 3.701%, 5.31%, 6.973% and 7.617% mass loss) at 1350 rpm with carried fluid (water) ( $A=-0.007, B=0.163$ )

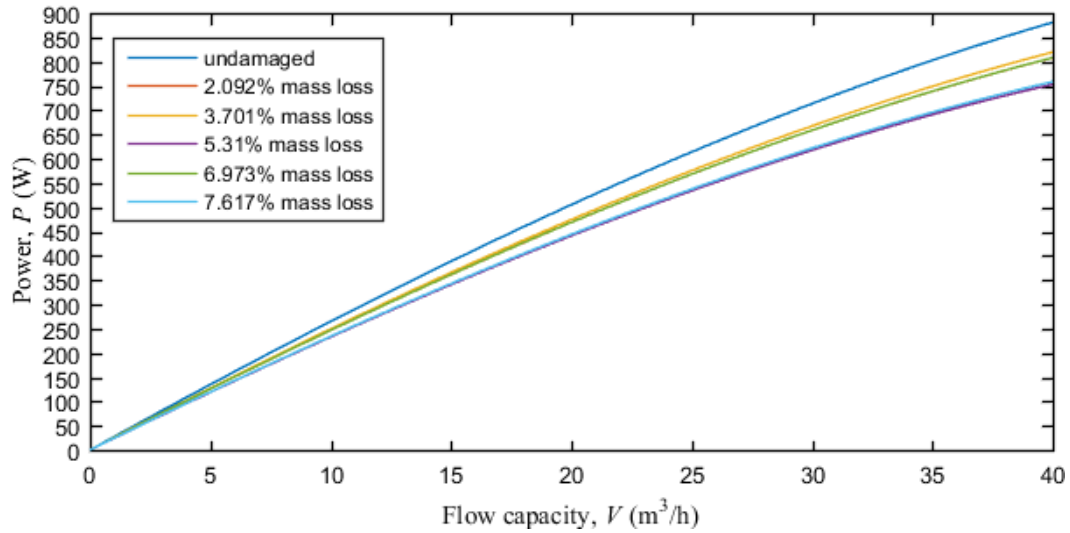


Figure 4.20. Power vs. flow capacity for different damage conditions (0%, 2.092%, 3.701%, 5.31%, 6.973% and 7.617% mass loss) at 1450 rpm with carried fluid (water) ( $A=-0.0015$ ,  $B=-0.0594$ )

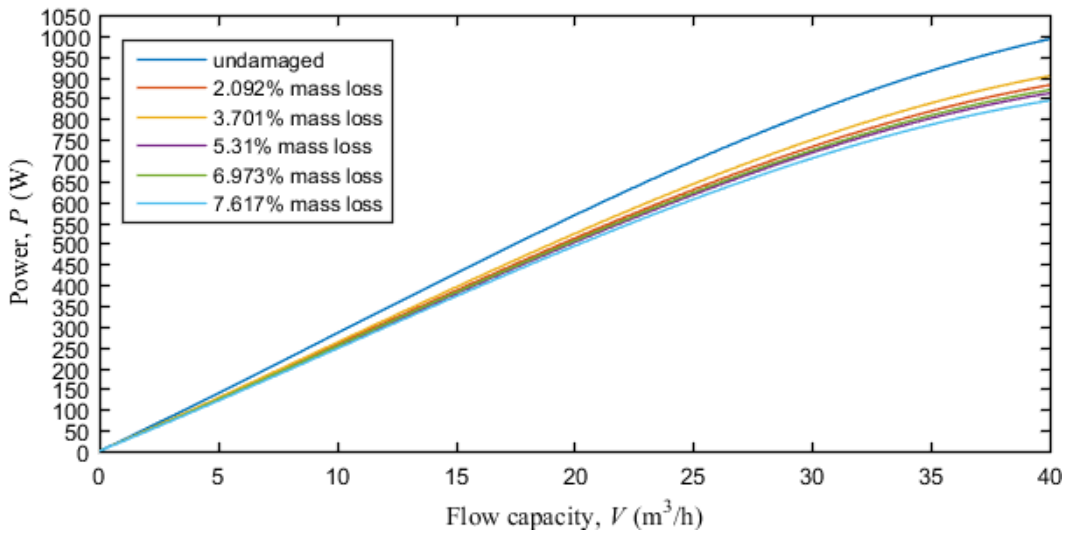


Figure 4.21. Power vs. flow capacity for different damage conditions (0%, 2.092%, 3.701%, 5.31%, 6.973% and 7.617% mass loss) at 1550 rpm with carried fluid (water) ( $A=-0.0067$ ,  $B=0.1359$ )

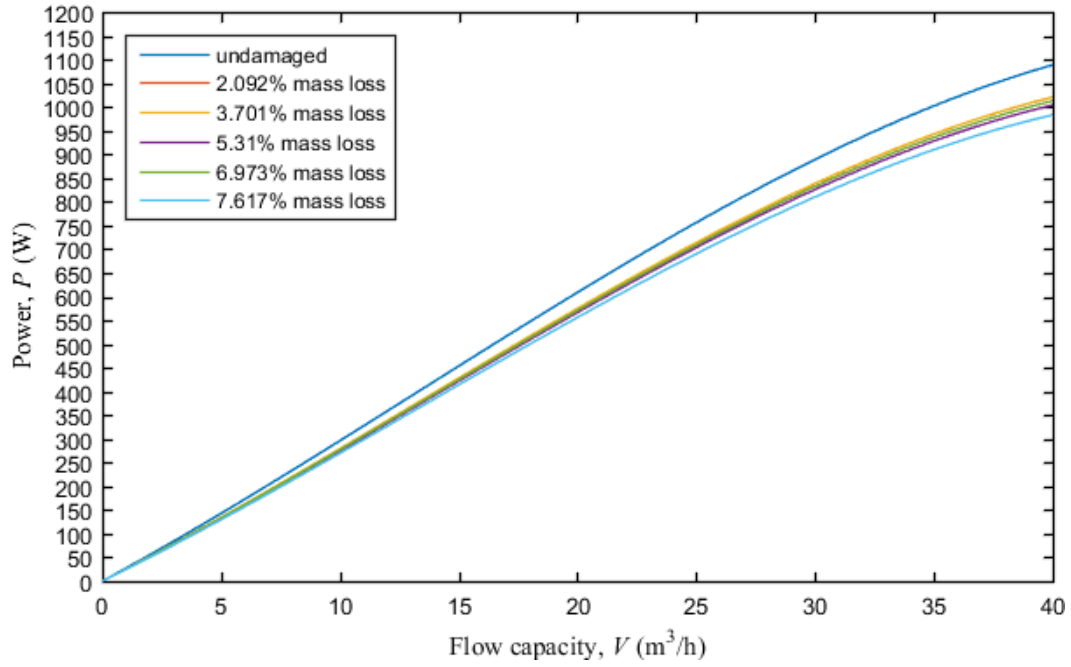


Figure 4.22. Power vs. flow capacity for different damage conditions (0%, 2.092%, 3.701%, 5.31%, 6.973%, and 7.617% mass loss) at 1650 rpm with carried fluid (water) ( $A=-0.009, B=0.241$ )

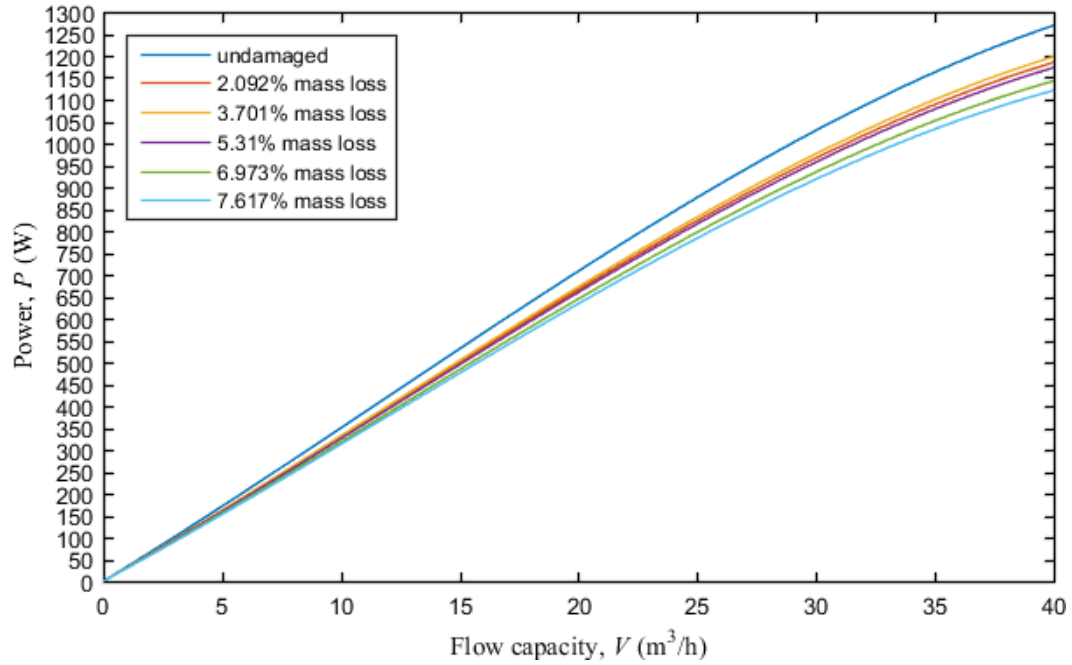


Figure 4.23. Power vs. flow capacity for different damage conditions (0%, 2.092%, 3.701%, 5.31%, 6.973%, and 7.617% mass loss) at 1750 rpm with carried fluid (water) ( $A=-0.0083$ ,  $B=0.1965$ )

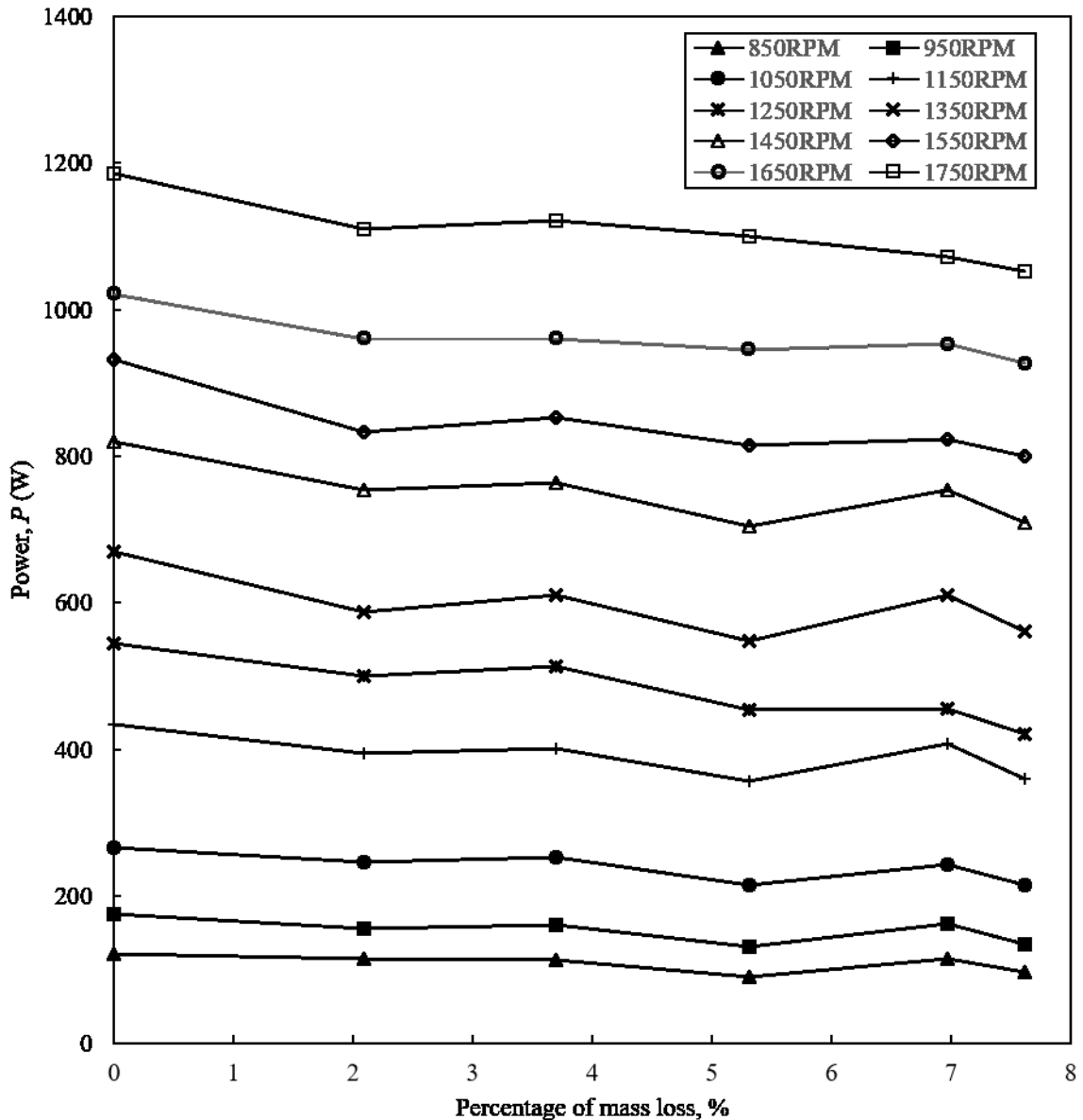


Figure 4.24. Power for a certain flow rate vs. percentage of mass loss for different rotational speeds (850 rpm, 950 rpm, 1050 rpm, 1150 rpm, 1250 rpm, 1350 rpm, 1450 rpm, 1550 rpm, 1650 rpm and 1750 rpm)

To sum up, the head losses generally increased as the mass loss of the impeller increased. It is clear that the head decreases with the increase in flow capacity over the peak value. Thus, one can conclude that the head of the pump increases with increasing rotational speed. The parabola

function can be used to fit the head and flow capacity relationship. It is hard to quantify the mathematical model for each value of  $A$ ,  $B$  and  $C$  if random fitting was performed for a good fitting; however, it is easier to find a math model for coefficient  $C$  by fixing coefficients  $A$  and  $B$ . An empirical model was derived for the relationship between coefficient  $C$ , the rotational speed and the percentage of mass loss. The empirical model describes the relationship better when the fixed coefficients  $A$  and  $B$  are applied for all the data points not the data points in each rotational speed. A special affinity law can also be used to predict the coefficient  $C$  in similar cases, but the exponents vary based on the percentage of mass loss. The range for the exponent  $n$  is 2.5 to 3. In other words, if the exponent of  $n$  is determined for the same damaged impeller, the coefficient  $C$  of the family curves can be obtained. If the manufacturer's performance curves can be given, the coefficients  $A$  and  $B$  can be obtained. With this method, the head and flow capacity relationship can be derived for the damaged impeller. Integrals are also conducted on the head and flow capacity function, which is also called the fluid power function. Fluid power and coefficient  $C$  have a similar trend of the change in percentage of mass loss. Also, when the rotational speed is high, the difference in fluid power for different damage conditions is not as large as when the rotational speed is low. In other words, damaged impellers have an impact on pump performance.

### **4.3 Limitations for the method**

To reduce the error and uncertainties in the experiments, calibrations were performed for the pressure transducers. Detailed information was presented in Chapter 2. The Coriolis flowmeter was calibrated by the manufacturer. A simple step was conducted to ensure that the Coriolis flowmeter was well-functioning. Clear tap water was added to the pipe system. The density of the water is  $998 \text{ kg/m}^3$ . The density that show in the Coriolis flowmeter was stable at  $996\text{-}998 \text{ kg/m}^3$ ,



which is acceptable. The temperature of water was measured using a thermometer and the results of thermometer were compared to the data obtained by Coriolis flowmeter. The difference in the results was less than 5%. The precision of the weigh scale was 0.1g. Every sample was weighed three times.

Due to cost and time limitations, the repeated experiments could not be performed for every experimental condition. The repeated experiment for the experiment at 5wt.% solid concentration of garnets and 1200 rpm of rotational speed was conducted. The wear locations were almost the same and the mass loss difference was 0.1g.

For the head/flow capacity results, it should be noted that the head loss occurred throughout the whole pipeline system. The pipeline in the lab was not initially designed to test the pump performance. As a result, the head loss in the pipeline was great and should not be ignored. However, it will require considerable calculations to obtain the head loss for every flow rate. In this thesis, the sources that produced head loss in the pipeline are simply listed. The head loss in the pipeline can be divided into a major loss and minor loss. The major loss, also called the frictional loss, was related to the diameter of the pipe, the friction coefficient of the material of the pipe and the flow velocity. The minor loss was produced by the components in the pipeline. The pipeline in this project contained one pipe exit, seven elbows, one knife-gate valve, and one ball valve. When looking for the coefficient of the valves, it is important to consider the open position of the valve. Calculating the head loss for each case would be a massive undertaking.

After discussions on the parametric studies of flow velocity and solid concentration, some modification can be conducted. The flow velocity used in the wear rate model was the flow rate in the pipeline because it was easy to obtain using the flow meter; however, the local velocity near the impeller also needed to be focused. In addition, the concentration used was not accurate enough;

the movement of the particles was random, and the suction in the pump may have changed the concentration at the local area. Also, it should be noted that there are fluctuations in flow rate and solids concentration. These fluctuations will cause error in flow rate and solids concentration that used in parametric studies.

In this project, almandite garnets were used as abrasives. Almandite garnets are the hardest one in all garnet types. Their Moh's hardness is in the range of 7-8 and specific gravity is 3.75-4.3g/cm<sup>3</sup> (Sil Industrial Minerals, 2017). Other small particles with different harness and specific gravities should also be used in slurries. Different types of particles can have different attacking angles. In this project, sliding wear often occurs in this project due to high hardness and high specific gravity. With different particles, various wear patterns may be created.

From Appendix F, it is obvious that flow in this pipeline is unsteady. Flow rate fluctuated drastically. This phenomenon occurs because of the presence of garnets. Due to the properties of garnets, garnets aggregated at the bottom of pipeline and sliding bed moved slowly. These factors can affect concentration and velocity that used in parametric studies.

Furthermore, because of head loss in the pipeline, operation points in this work are away from best efficiency point (BEP). If pump operates at BEP flow rate, random impingement mechanism will occur frequently (Roco, 1990). This may be cause decrease in relative velocity between particles and impellers. More particles may be aggregate around impeller and result in more abrasion on impellers.

In conclusion, head loss in the pipe loop may cause the operation points to be away the BEP, which will affect wear behavior of impellers. Particles should be selected from small size to

large size, which can create various wear patterns on impellers. If experimental budgets allowed, repetitive tests should be conducted.

## 5. Conclusions and Future Work

### 5.1 Conclusions

- The region with the most abrasion is the upper edge of the blades near the hub. The wear process of the impeller in the heavy-duty slurry pump used in this project will started from the area at the upper leading edge near the hub. The width of the upper trailing edge began to wear, and the lower edge of the trailing edge was worn by the end of abrasive process in the impeller blades. Changing the rotational speed had a more significant influence than changing the concentration of solids. Apparently, the height and width of the blades decreased drastically when changing the pump's rotational speed, however, the variation in the solid concentration has less of an impact on the change in the geometry of the impeller. Due to the characteristics of the polymer and garnet-water slurry, sliding wear occurs and the worn surfaces of the samples were smooth.
- Both flow velocity and solid concentration have a power law relationship with wear rate. The flow velocity had a dominant effect on the wear rate. The solid concentration had a less significant effect. A comparison of the results obtained from this project with results from other studies showed that the exponents of the flow velocity and concentration of polymer samples were both larger than those in metal samples. Based on the literature about the wear behavior of polymers, the exponents of the concentration and flow velocity in a polymer's wear rate model were larger than those in the metal's wear rate model, especially for hard metals. The exponents of concentration and velocity have reasonable agreement with previous studies (Gupta et al. (1995), Elkholy et al. (1983), Pool et al. (1986)). If different particle size of particles can be used in future study, it is possible to

correct the wear coefficient  $K$  and obtain a final equation which combined with velocity, concentration and diameter of particles.

- The wear rate of the same sample is decreased slightly over time. One reason was that the shape of blades changed. Another possible reason was particle degradation.
- The damaged impellers significantly affect the pump performance. In this work, it was found that damaged impellers could affect the head of the pump. In addition, the fluid power in the pump can be influenced. In other words, damaged impeller could cause the energy loss in the pump. It will be helpful for engineers to find a time to replace a damaged impeller.
- Comparing with manufacturer's data, undamaged impellers' head curves for each rotational speed are lower. Head drop increases as flow rate increases. The head drop for low flow rate at each rotational speed is around 0.5m.
- Parabolic function can be used to precisely describe the head and flow capacity relationship. By fixing coefficients  $A$  and  $B$ , it was possible to obtain a family of curve fitting lines. A special affinity law could be applied to predict coefficient  $C$  when undamaged impeller diameter is constant. Also, an empirical model could be concluded for coefficient  $C$  by considering the factors of rotational speed and percentage of mass loss.
- A method to predict the head and flow capacity relationship of damaged impellers was proposed based on the performance curves of pump with undamaged impeller. With undamaged impeller's performance data, it would be possible to determine the coefficients  $A$  and  $B$ . The coefficient  $C$  could be calculated using an empirical model when the percentage of mass and rotational speed could be known.

- The experimental method in this project was to use the impeller fabricated with soft material, in this case, a polymer (Verogray) commonly used in 3D printing technology can highly reduce the experimental time and cost. Using 3D printing technology also reduces the time needed to prepare experimental samples. On the other hand, the samples were put in the laboratory pipeline loop that simulated an actual industrial field loop, which could increase the accuracy of the results. The method in this project establish a foundation to correlate the polymer's wear model to the metal's wear model.
- The results of this project may be used to predict the wear rate and service life of impellers. The data generated can help engineers and manufacturers to find a suitable time to conduct pump maintenance, which can save energy and costs.

## **5.2 Recommendations for future work**

- The pipeline may be modified to make it more suitable for performing the experiments related to pump performance. In this project, the pipeline was not eligible to accurately conduct performance tests. Other instruments should also be added, for example, an instrument which can obtain the output power of the pump may be added to get the efficiency data of the pump. In addition, an instrument, for example a densitometer, that can measure the solid concentration in the pipeline should be considered.
- In this project, the flow rate in the pipe was measured using a Coriolis flowmeter; however, the wear rate of the impeller may have been affected by the velocity of the particles. It is hard to find an efficient way to obtain the velocity of the particles in an experiment. Computer simulations are the easiest and most economical way to obtain the velocity of particles. The velocity of particles is one of the most critical factors related to the wear

behavior of an impeller because the wear patterns are produced by the impingement of particles. If the movement of a particle can be simulated, this will give a microscopic view of the wear behavior on the impeller. In addition, the local velocity or motions of the bulk flow near the blades is worth to investigating

- The samples in this project used polymers to fabricate. Other alternative soft materials can be used if there is enough of a budget. Soft metal materials such as brass and aluminum can also be used. Future studies may uncover the link between soft metal materials and polymers.
- Actual field experiments can also be conducted. Data from the field experiments can be compared with data from the laboratory loop with polymers, soft metal materials and hard metal materials.
- More parametric studies need to be conducted if possible. In this project, only two factors, concentration and flow velocity, were investigated. Garnet is a type of large and heavy particle. Other abrasives with different size and specific gravity should be employed in future studies. More parametric studies, such as the effect of the particle size distribution and the hardness of the target materials and erodent materials, may be added in the future study.
- More performance tests may be performed using impellers with different damage conditions. Empirical model to predict pumps' head curves can be optimized and the errors in this project can be avoided.

# Bibliography

Arnell, R.D., Davies, P.B., Halling, J. and Whomes, T.L. (1991). *Tribology: Principles and Design Application*. New York, NY: Springer-Verlag.

Amarendra, H.J., Chaudhari, G.P. & Nath, S.K. (2012). Synergy of cavitation and slurry erosion in the slurry pot tester. *Wear*. Vol. 290-291, pp. 25-31.

Arabnejad, H., Mansouri, A., Shirazi, S., & McLaury, B. (2015). Development of mechanistic erosion equation for solid particles. *Wear*. Vol. 332-333, pp. 1044-1050.

Bitter, J.G.A. (1962). A study of erosion phenomena. Parts I and II. *Wear*. 6: 5-21.

Brauer, H. & Kriegel, E. (1963). Untersuchungen über den Verschleiss von Kunststoffen und Metallen, *Chem. Ing. Tech.* 35(10) 697-707.

Burgess, K.E. & Reizes, J.A. (1976). The effect of sizing, specific gravity and concentration on the performance of centrifugal slurry pumps. *Institution of Mechanical Engineers*. Vol. 190, pp. 391-399.

Baker, R.C. (2000). *Flow measurement handbook*. University of Cambridge.

Batalovic, V. (2010). Erosive wear model of slurry pump impeller. *Journal of Tribology*. Vol. 132.

Clark H.M., Wong, K.K. (1995) Impact angle, particle energy and mass loss in erosion by dilute slurries. *Wear*. Vol. 186-187, pp. 454-464

Clark, H.M., Tuzson, J., Wong, K.K. (2000). Measurements of specific energies for erosive wear using Coriolis erosion tester. *Wear*. Vol. 241, pp. 1-9.



Cooke, R., Johnson, G. & Goosen, P. (2000). Laboratory apparatus for evaluating slurry pipeline wear. *Economics of Wear Material*. No. March, pp. 1-17

Clark, H.M. & Hartwich R.B. (2001). A re-examination of the 'particle size' effect in slurry erosion. *Wear*. Vol. 248, pp. 147-161

Clark, H.M. (2002). Particle velocity and size effects in laboratory slurry erosion measurement OR... do you know what your particles are doing? *Tribology International* Vol. 35, pp. 617-624.

Chandel, S., Singh, S.N., & Seshadri, V. (2012). Experimental study of erosion wear in a centrifugal slurry pump using coriolis wear test rig. *Particulate Science & Technology*. Vol. 30(2), pp. 179-195.

Cellek, M. S. & Engin, T. (2016). Parametric investigation of a centrifugal slurry pump while handling clear water. *Journal of Thermal Science and Technology*. Vol. 36, pp. 19-28.

Dasgupta, R., Prasad, B.K., Jha, A.K. Modi, O.P. & Yegneswaran, A.H. (1997). Wear characteristics of a hardfaced steel in slurry. *Wear*. Vol. 209, pp. 255-262.

Elkholy A. (1983). Prediction of abrasion wear for slurry pump materials. *Wear*. Vol. 84, pp. 39-49.

ES-Said, O. S., Foyos, J., Noorani, R., Mendelson, M., Marloth, R & Pregger, B. A. (2000) Effect of layer orientation on mechanical properties of rapid prototyped samples. *Materials and Manufacturing Process*. 15: 1, 107-122.

EI-Sayed, S. (2010) Measuring wall forces in a slurry pipeline. Master of Science thesis, University of Alberta.

Finnie, I. Erosion of surfaces by solid particles. *Wear*. 3: 87-103

Feyzullahoglu, E. & Sakiroglu, N. (2010). The wear of aluminum-based journal bearing materials under lubrication. *Materials and Design*. 31: 2532-2539.

Evans, J. (2015). How lower efficiency can reduce overall cost. *Pump industry*. 13: 26-27.

Gandhi, B.K., Singh, S.N. & Seshadri, V. (1998). Prediction of performance characteristics of a centrifugal slurry pump handling clear liquid. *Indian Journal of Engineering and Materials Sciences*. Vol 5, pp. 91-96

Gandhi, B. K., Singh, S. N. & Seshadri, V. (2000), Improvements in the prediction of performance of centrifugal slurry pumps handling slurries. *Proceedings of the Institution of Mechanical Engineers, Part A: Journal of Power and Energy*. 214(5): 473-486

Gandhi, B.K., Singh, S.N. & Seshadri, V. (2001). Variation of wear along the volute casing of a centrifugal slurry pump. Vol. 44, pp. 231-237.

Gandhi, B. K., Singh, S. N., Seshadri, V. (2002), Effect of speed on the performance characteristics of a centrifugal slurry pump. *Journal of Hydraulic Engineering*, Vol. 128, pp. 225-233.

Gonzalez, J., Fernandez, J., Blanco, E. & Santolaria, C. (2002). Numerical simulation of the dynamic effects due to impeller-volute interaction in a centrifugal pump. *Journal of Fluids Engineering*. Vol. 124(2): 348-355.

Gupta, R., Singh, S.N. & Sehadri, V. (1995). Prediction of uneven wear in a slurry pipeline on the basis of measurements in a pot tester. *Wear*, Vol. 184, pp. 169-178

Gupta, M., Kumar, S. & Kumar, A. (2011). Numerical study of pressure and velocity distribution analysis of centrifugal pump. *International Journal of Thermal Technologies*. Vol.1. pp.114-118

GIW industries Inc. (2012) MDX technology cuts pump TCO by millions. *Coal Age*. 117(5): 47.

Garg, H., & Singh, R. (2017). Tribological Properties of Fe-Nylon6 Composite Parts Prepared Using Fused Deposition Modelling. *Transactions of the Indian Institute of Metals*. 70(5): 1241-1244.

Hashish, M. (1987). A model for abrasive-waterjet (AWJ) machining. *Journal of Engineering Materials and Technology*. 111:154-162

Hawthorne, H.M., Xie, Y., & Yick, S.K. (2003). A new Coriolis erosion tester design for improved slurry dynamics. *Wear*. 255: 170–180.

Hemanth, J. (2011). Abrasive and slurry wear behavior of chilled aluminum alloy (A356) reinforced with fused silica (SO<sub>2</sub>P) metal matrix composites. *Composites Part B: Engineering*. Vol. 42, pp. 1826-1833.

Iwai, Y. & Nambu, K. (1997). Slurry wear properties of pump lining materials. *Wear*. Vol. 210, pp. 211-219

Janssen, A., Pinedo, B. Igartua, A., Liiskmann, G. & Sexton, L. (2017). Study on friction and wear reducing surface micro-structures for a positive displacement pump handling highly abrasive shale oil. *Tribology International*. 107: 1-9.

Karassik, I. J. (1987). Centrifugal pump operation at off-design condition. *Chemical Engineering*.

Kadambi, J.R., Wernet, M.P., Sankovic, J.M. & Addie, G. (2004). Investigations of particle velocities in a slurry pump using PIV: Part 1, the tongue and adjacent channel flow. *ASME Journal of Energy Resources Technology*. 126:1-9

Khan, Z. A., Lee, B. H. & Abdullah, J. (2005). Optimization of rapid prototyping parameters for production of flexible ABS object. *Journal of Materials Processing Technology*. 169: 54-61

Khalid, Y.A. & Sapuan, S.M. (2007). Wear analysis of centrifugal slurry pump impeller. *Industrial Lubrication and Tribology*. Vol. 59, Iss 1. pp. 18-28

Kruger, S., Martin, N. & Dupont, P. (2010). Assessment of wear erosion in pump impellers. *Proceeding of The Twenty-Sixth International pump users symposium*.

Pagalthivarthi, K.V., Gupta, P.K., Tyagi, V. & Ravi, M.R. (2011). CFD predictions of dense slurry flow in centrifugal pump casing. *International Journal of Mechanical and Mechatronics Engineering*. Vol.5, No. 3, pp.538-550

Kumar, S., Gandhi, B.K. & Mohapatra, S.K. (2014). Performance characteristics of centrifugal slurry pump with multi-sized particulate bottom and fly ash mixtures. *Particulate science and technology*. 32: 466-476.

Lewis, R. B. (1964). Predicting the wear of sliding plastic surfaces. *Mechanical Engineering*. 86 (10), 32

Lobanoff, C. S. & Ross, R. R. (1992). *Centrifugal pumps design & application (second edition)*. Gulf Professional Publishing.

Liu, S., Tang, X., Wu, Y. & Nishi, M. (2004). Simulation of dense solid-liquid two-phase flow in a pump impeller. *ASME proceedings*. Vol. 2, pp. 461-467

Liu, J. & Zhu, M. (2010). Numerical simulation of solid-liquid two-phase flow in centrifugal sewerage pump. *Applied Mechanics and Materials*. Vol. 44-47, pp. 345-348.

Li, Y., Zhu, Z., He, Z., & He, W. (2011). Abrasion characteristic analyses of solid-liquid two-phase centrifugal pump. *Journal of Thermal Science*. 20(3): 283-287.

Lindgren, M. & Perolainen J. (2014). Slurry pot investigation of the influence of erodent characteristics on the erosion resistance of titanium. *Wear*. 321: 64-69

Lindgren, M. & Perolainen, J. (2014). Slurry pot investigation of the influence of erodent characteristics on the erosion resistance of austenitic and duplex stainless steel grades. *Wear*. 319: 38-48

Lindgren, M., Suihkonen, R., & Vuorinen, J. (2015). Erosive wear of various stainless steel grades used as impeller blade materials in high temperature aqueous slurry. *Wear*. 328-329: 391-400.

Meng, H. C. & Ludema, K. C. (1995). Wear models and predictive equations: their form and content. *Wear*. 181-183: 443-457.

Majidi, K. (2004) Numerical study of unsteady flow in a centrifugal pump. *ASME. Turbo Expo: Power for Land, Sea, and Air*. Vol. 5. pp. 805-814.

- Mehta, M., Kadambi, S. & Sastry, S. (2007). Particle velocities in the rotating impeller of a slurry pump. *Fluids Engineering Conference*. pp. 369-378
- Nguyen, V. B., Nguyen, Q. B., Zhang, Y. W., Lim, C. Y. H. & Khoo, B. C. (2016) Effect of particle size on erosion characteristics. *Wear*. 348-349: 126-137.
- Noon, A. A. & Kim, M. (2016). Erosion wear on centrifugal pump casing due to slurry flow. *Wear*, Vol 364-365, pp. 103-111
- Oka, Y.I., Okamura, K. & Yoshida, T. (2005). Practical estimation of erosion damage caused by solid particle impact Part 1: Effects of impact parameters on a predictive equation. *Wear*. 259:95-101
- Ojha, S., Acharya, S.K. Gujjala, R. (2014). Characterization and wear behavior of carbon black filled polymer composites. *Procedia Materials Science*. 6: 468-475
- Ojala, N., Valtonen, K., Kivikytö-Reponen, P., Vuorinen, P., & Kuokkala, V-T. (2015). High speed slurry-poterosion wear testing with large abrasive particles. *Tribologia - Finnish Journal of Tribology*, 33(1), 36-44.
- Pool, K. V., Dharan, C.K.H. & Finnie, I. (1986). Erosive wear of composite materials. *Wear*. Vol. 107, pp. 1-12
- Pagalthivarthi, K.V.; Helmly, F.W. (1992). Applications of material wear testing to solids transport via centrifugal slurry pumps. *Wear Testing of Advanced Materials*. pp. 114-126.
- Pagalthivarthi, K., & Gupta, P. (2009). Prediction of erosion wear in multi-size particulate flow through a rotating channel. *Fluid Dynamics and Materials Processing*. 5(1): 93-121.

- Roco, M., Nair, P., Addie, G., & Dennis, J. (1984). Erosion of concentrated slurries in turbulent flow. *Journal of Pipelines*. 4(3): 213-221.
- Roco, M.C., Marsh, M., Addie, G.R. & Maffett, J.R. (1986). Dredge pump performance prediction. *Pipelines*. 5: 171-190.
- Roco, M.C. & Addie, G.R. (1987). Erosion wear in slurry pumps and pipes. *Power Technology*. 50: 35-46
- Roco, M. C. (1990). Wear mechanisms in centrifugal slurry pumps. *Corrosion*. 46(5): 424-431.
- Roy, M., Vishwanathan, B., & Sundararajan, G. (1994). The solid particle erosion of polymer matrix composites. *Wear*. 171: 149-161
- Ravichandra, J.S.; Pagalthivarthi, K.V. & Sanghi, S. (2005): Multi-size particulate flow in horizontal ducts – modeling and validation. *Progress in Computational Fluid Dynamics*. Vol. 5, Issue 8, pp. 466-481.
- Rajahram, S.S., Harvey, T.J. & Wood, R..J.K. (2011) Electrochemical investigation of erosion-corrosion using a slurry pot erosion tester. *Tribology International*. 44: 232-240.
- Sheldon, G.L. (1970). Similarities and differences in the erosion behavior of materials. *Journal of basic engineering*. Vol. 92, pp.619-626
- Summer, R. M. (1987). A Review of Pipeline Slurry Erosion Measurements and Research Recommendations. *Slurry Erosion: Uses, Applications, and Test Methods*. pp. 91–100.
- Soboli, M. I. (1998). *Mathematical Methods Monte Carlo*. Nedra, Moscow, pp. 34–72.

Sarker, N. R. (2016). A preliminary study of slurry pipeline erosion using a toroid wear tester (master's thesis).

Sarkar, S., Sen, S. & Mishra, C. (2010). Studies on Aluminum-fly-ash composite produced by impeller mixing. *Journal of Reinforced Plastics and Composites*. 29(1): 144-148.

Shukla, S., Roy, A. K., & Kumar, K. (2015). Material selection for blades of mixed flow pump impeller using ANSYS. *Materials Today: Proceedings*. 2(4th International Conference on Materials Processing and Characterization), 2022-2029.

Shen, Z.J., Li, R.N., Han, W., Zhao, W.G. & Wang, X.H. (2016). The research on particle trajectory of solid-liquid two-phase and erosion predicting in screw centrifugal pump. *Materials Science and Engineering*. 129: 12-52.

Sino garnet (China). (2017) *Sil Industrial Minerals*.

Sood, A.K., Equbal, A., Toppo, V., Ohdar, R., & Mahapatra, S. (2012). An investigation on sliding wear of FDM built parts. *CIRP Journal of Manufacturing Science and Technology*. 5: 48-54.

Suh, M., Hinoki, T. & Kohyama, A. (2011) Erosive wear mechanism of new SiC/SiC composites by solid particles. *Tribology Letters*. 41: 503-513.

Tuzson, J.J. & Scheibe-Powell, K.A. (1984). Slurry erosion tests with centrifugal erosion tester. *Proc. FEDSM 98 ASME Fluids Eng. Division Summer Meeting*. pp. 1-5

Tian, H.H., Graeme, R., Krishnan, V. & Pagalthivarthi, V. (2005). Determination of wear coefficients for erosive wear prediction through Coriolis wear testing. *Wear*. 259: 160-170.



Tian, H.H. Graeme, R.A. & Edward, P.B (2007). A new impact erosion testing setup through Coriolis approach. *Wear*. 263: 289-294

Visintainer, R.; Pagalthivarthi, K.V.; Tian, H.H. (2005): Wear coefficient's dependence on particle size. *GIW Internal Report*.

Worster, B.C. & Denny, D.F. (1955) Hydraulic transport of solids material in pipes. *Proceeding of the Institution of Mechanical Engineers*. 169(1): 563-586

Walker, C.I. & Goulas, A. (1984). Performance characteristics of centrifugal pumps when handling non-Newtonian homogeneous slurries. *Proceedings of the Institution of Mechanical Engineers, Part A: Journal of Power and Energy*. 198(1): 41-49

Walker, C.F., Wells, P.J. & Pomat, C. (1992). The effect of impeller geometry on the performance of centrifugal slurry pumps. Proc. 4<sup>th</sup> Int. Conf. on Bulk material Handling and Transportation, IE Aust, Wollongong, Australia, pp. 97-101

Walker, D.T., Chen, C.Y. & Willmarth, W.W. (1995). Turbulent structure in free-surface jet flows. *Journal of Fluid Mechanics*. Vol.291, pp. 223-261

Wilson, R., & Hawk, J. (1999). Impeller wear impact-abrasive wear test. *Wear*, 225-229 (PART II), 1248-1257.

Walker, C.I. & Bodkin, G.C. (2000). Empirical wear relationships for centrifugal slurry pumps: Part 1: side-liners. *Wear*. 242(1-2): 140-146.

Wilson, K.C., Addie, G.R., Sellgren, A. & Clift, R. (2006). Slurry transport using centrifugal pumps. Springer US

Westra, R.W., Broersma, L. Andel, K.V. & Kruyt, N.P. (2010). PIV measurements and CFD computations of secondary flow in a centrifugal pump impeller. *Journal of Fluids Engineering*. Vol. 132.

Wu, J. Graham, L. J. W. et al. (2011). An effective modeling for studying erosion. *Wear*. 270: 598-605

Wong, K.V. & Hernandez, A. (2012). A review of additive manufacturing. *International Scholarly Research Notices*. Vol. 2012

Walker, C.J. & Hambe, M. (2015). Influence of particle shape on slurry wear of white iron. *Wear*. 332-333: 1021-1027

Wu, B., Wang, X., Liu, H. & Xu, H. (2015). Numerical simulation and analysis of solid-liquid two-phase three-dimensional unsteady flow in centrifugal slurry pump. *Journal of Central South University*. Vol.22(8): 3008-3016.

Xing, D., Hai-lu, Z., & Xin-yong, W. (2009). Finite element analysis of wear for centrifugal slurry pump. *Procedia Earth and Planetary Science*. 1: 1532-1538.

Xie, Y., Jiang, J., Tufa, K.Y. & Yick, S. (2015). Wear resistance of materials used for slurry transport. *Wear*. 332-333(20th International Conference on Wear of Materials): 1104-1110.

Yoganandh, J., Natarajan, S. & Kumares Babu, S.P. (2013). Erosive wear behavior of nickel-based high alloy white cast iron under mining conditions using orthogonal array. *Journal of Materials Engineering and Performance*. 22: 2534-2541

Zhong, Y., & Minemura, K. (1996). Measurement of erosion due to particle impingement and numerical prediction of wear in pump casing. *Wear*. 199(1): 36-44.

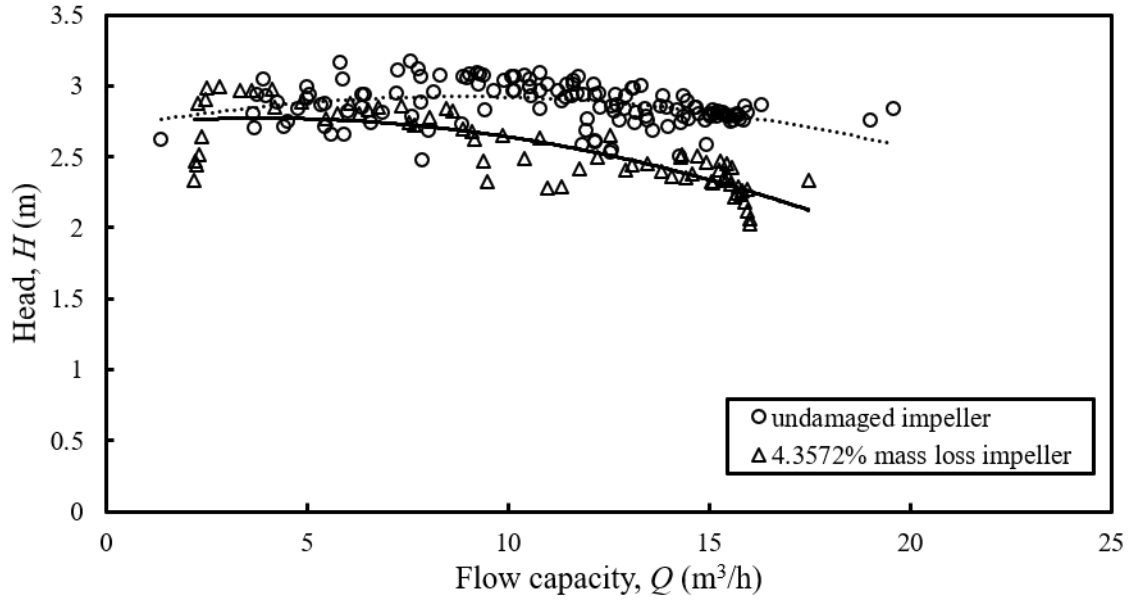
Zhang, Y., Li, Y., Cui, B., Zhu, Z. & Dou, H. (2013). Numerical simulation and analysis of solid-liquid two-phase flow in centrifugal pump. *Chinese journal of Mechanical Engineering*. 26 (1): 53-60.

Zhao, Y., Zhou, F., Yao, J., Dong, S. & Li, N. (2015). Erosion-corrosion behavior and corrosion resistance of AISI 316 stainless steel in flow jet impingement. *Wear*. 328-329: 464-474

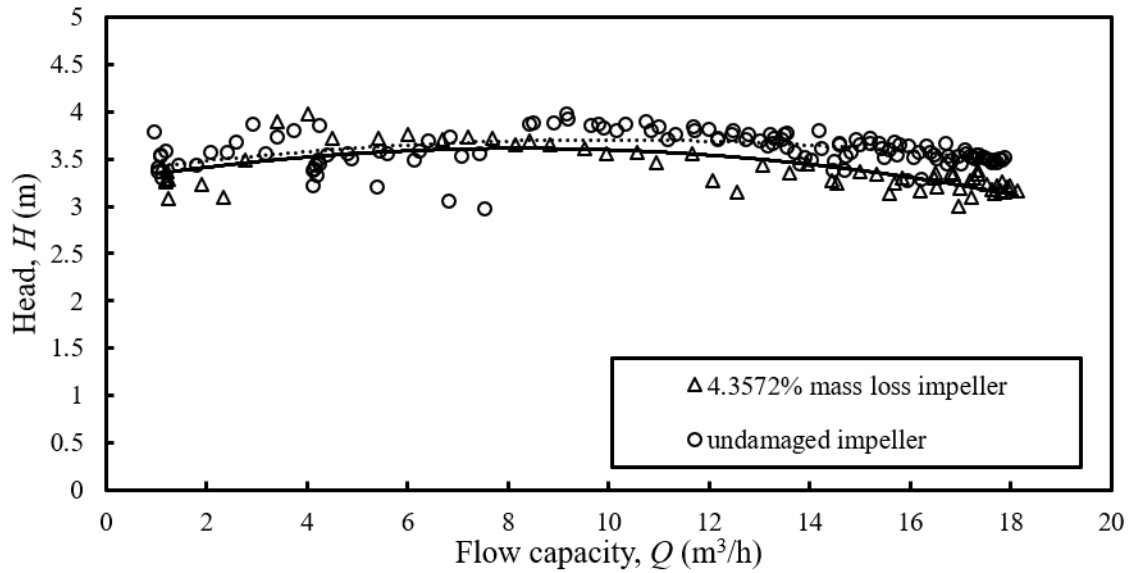
Zhang, H., Zhang, L. & Yao, J. (2016). Numerical investigation sediment wear in a centrifugal pump impeller. *Advanced Materials, Technology and Application*. pp. 264-271

# **Appendices**

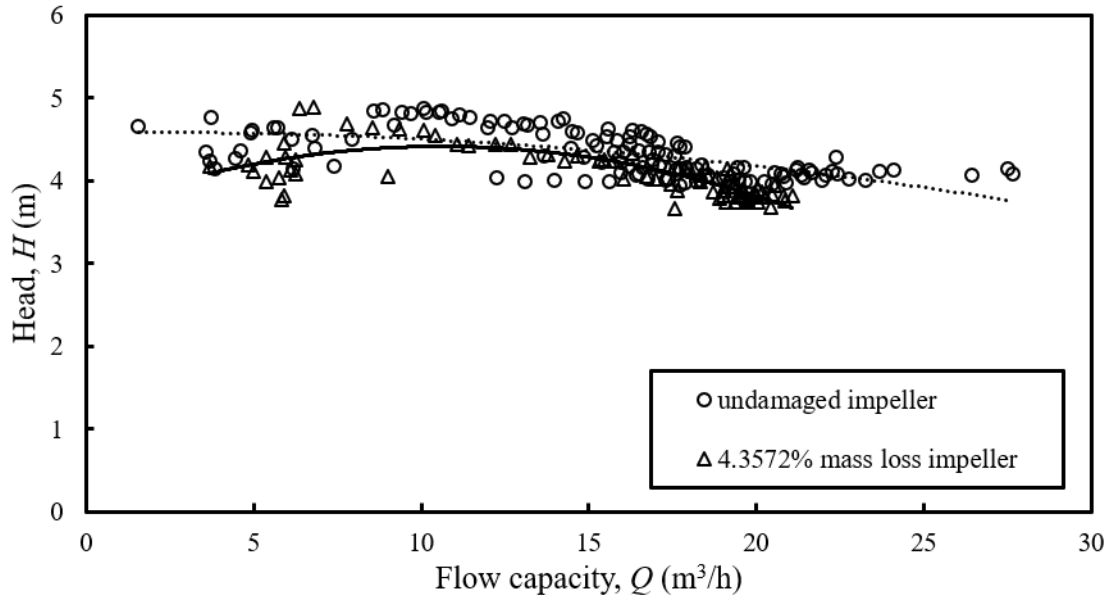
## **A.Data of other percentages of mass loss**



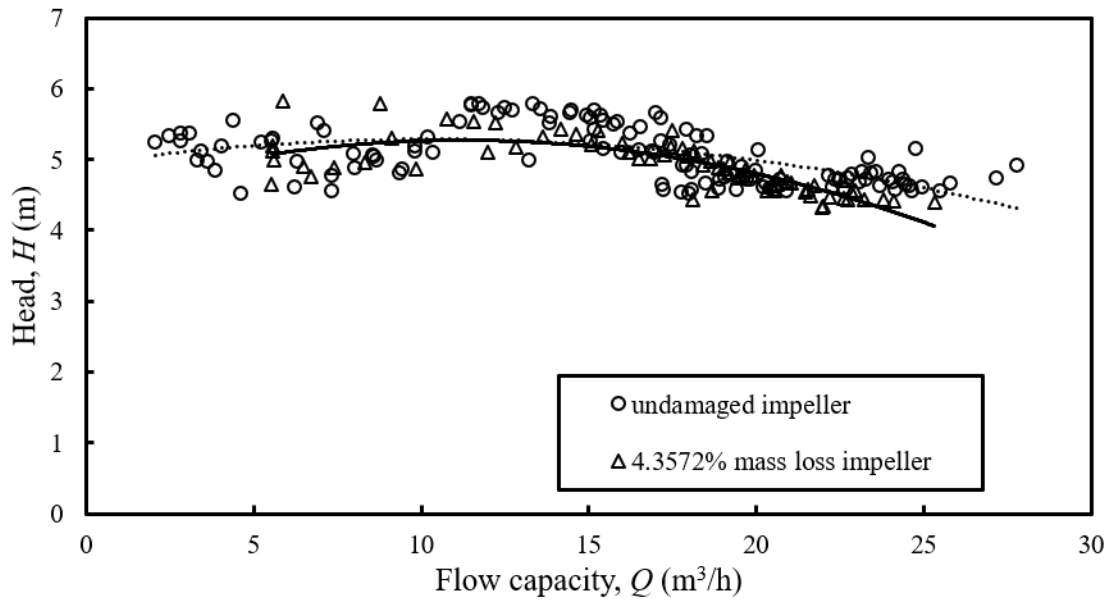
A.1. Head-flow capacity relationship at 850 rpm & 5wt.% concentration after 24 hours  
 1500 rpm wearing



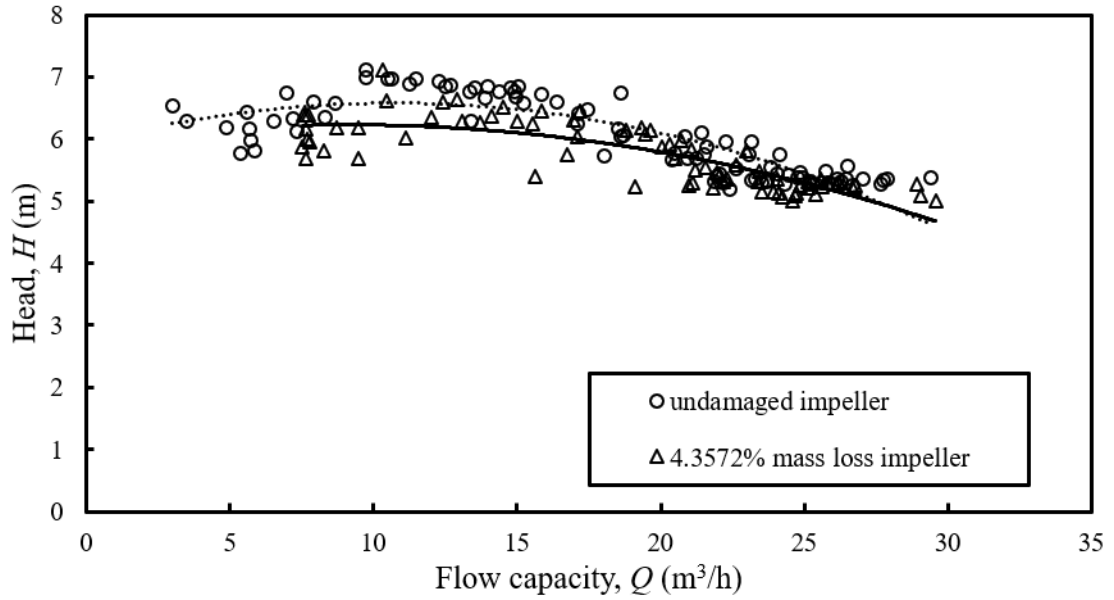
A.2. Head-flow capacity relationship at 950 rpm & 5wt.% concentration after 24 hours  
 1500 rpm wearing



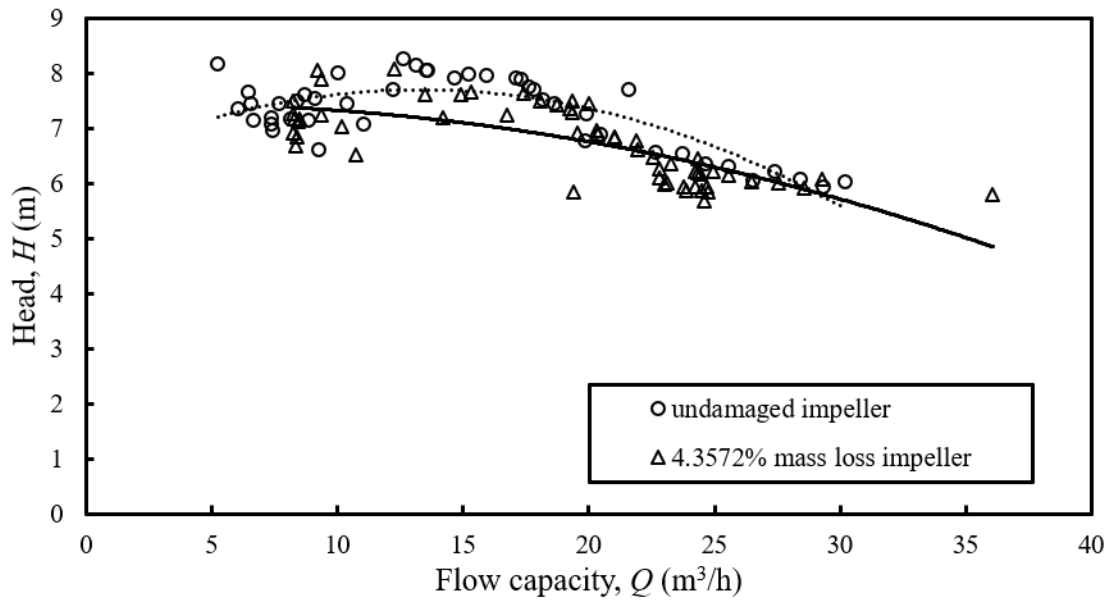
A.3. Head-flow capacity relationship at 1050 rpm & 5wt.% concentration after 24 hours  
1500 rpm wearing



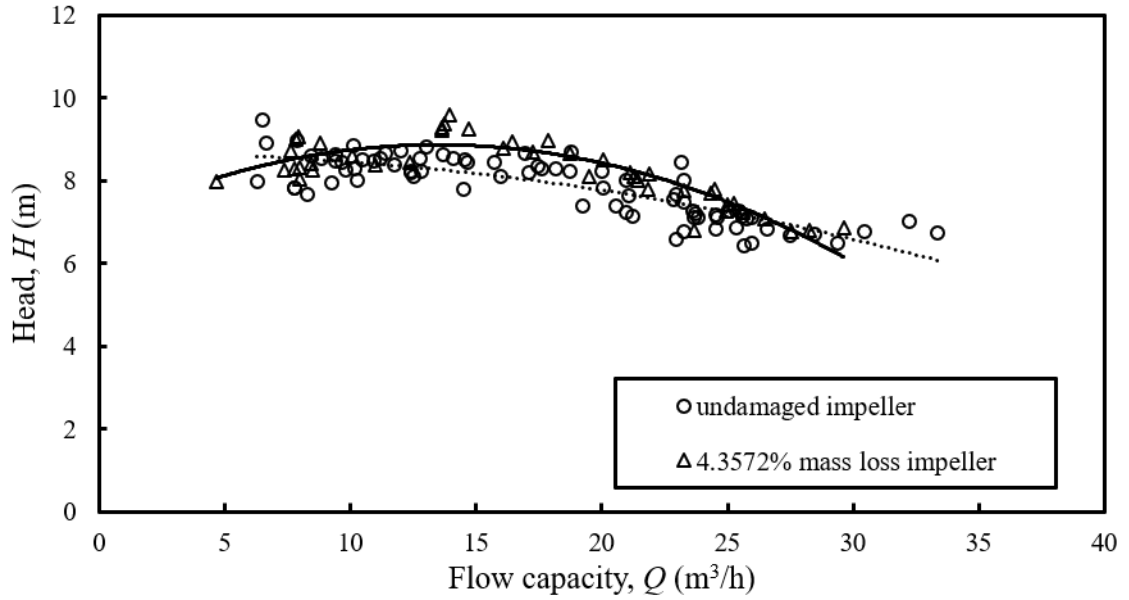
A.4. Head-flow capacity relationship at 1150 rpm & 5wt.% concentration after 24 hours  
1500 rpm wearing



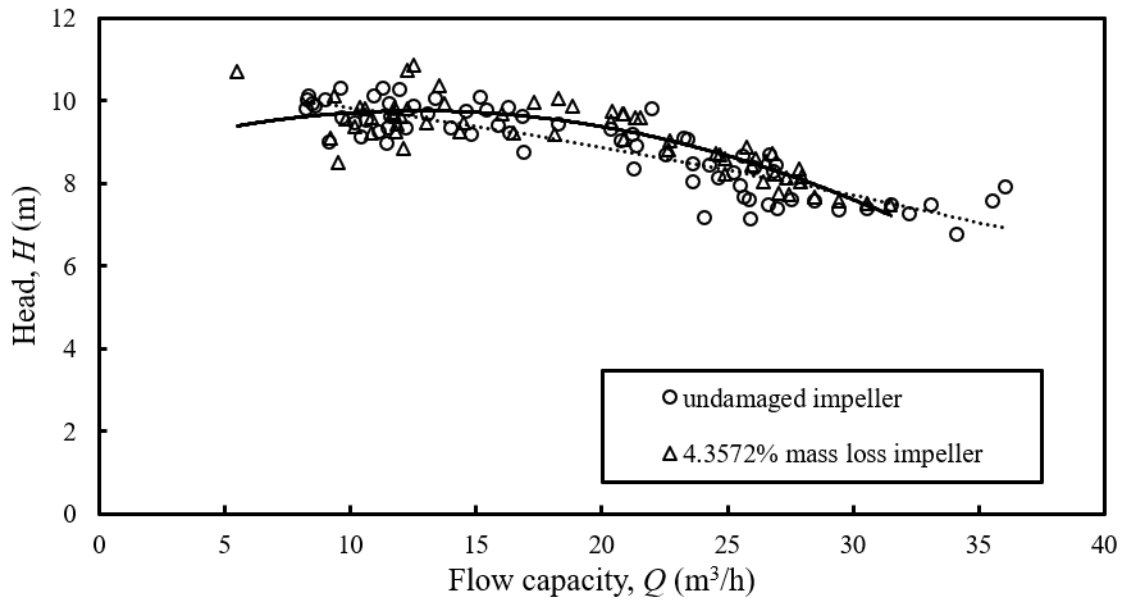
A.5. Head-flow capacity relationship at 1250 rpm & 5wt.% concentration after 24 hours  
1500 rpm wearing



A.6. Head-flow capacity relationship at 1350 rpm & 5wt.% concentration after 24 hours  
1500 rpm wearing

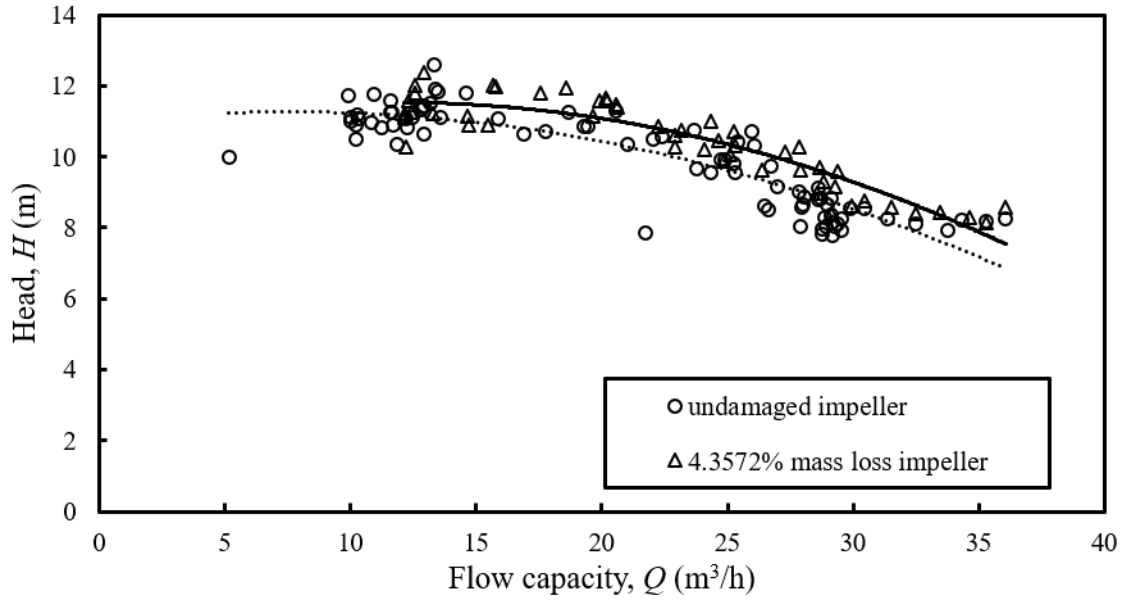


A.7. Head-flow capacity relationship at 1450 rpm & 5wt.% concentration after 24 hours  
1500 rpm wearing

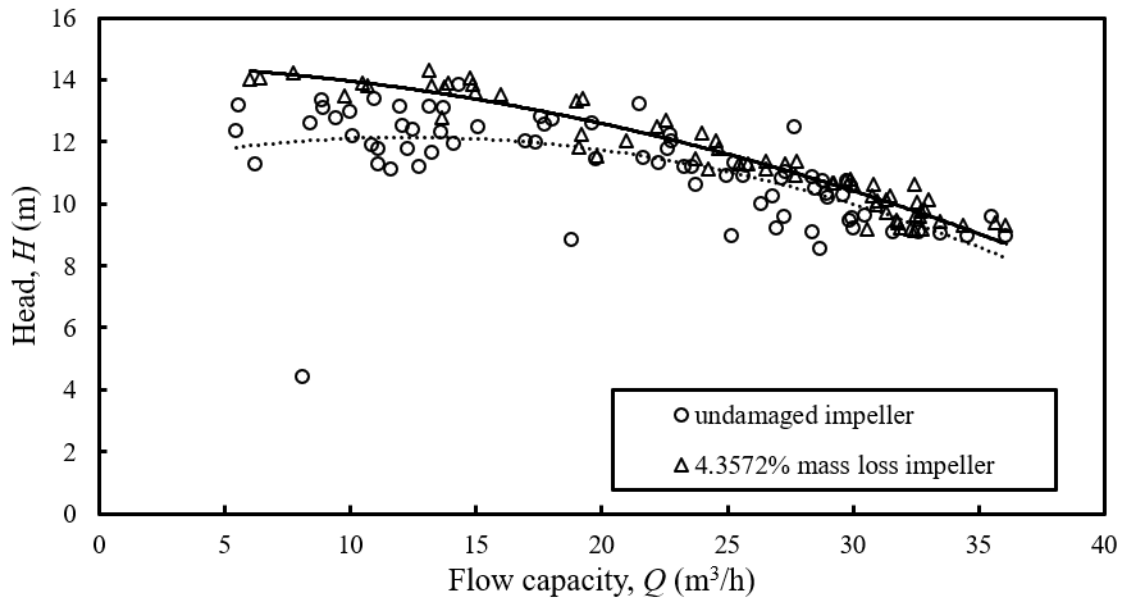


A.8. Head-flow capacity relationship at 1550 rpm and 5wt.% concentration after 24 hours  
1500 rpm wearing

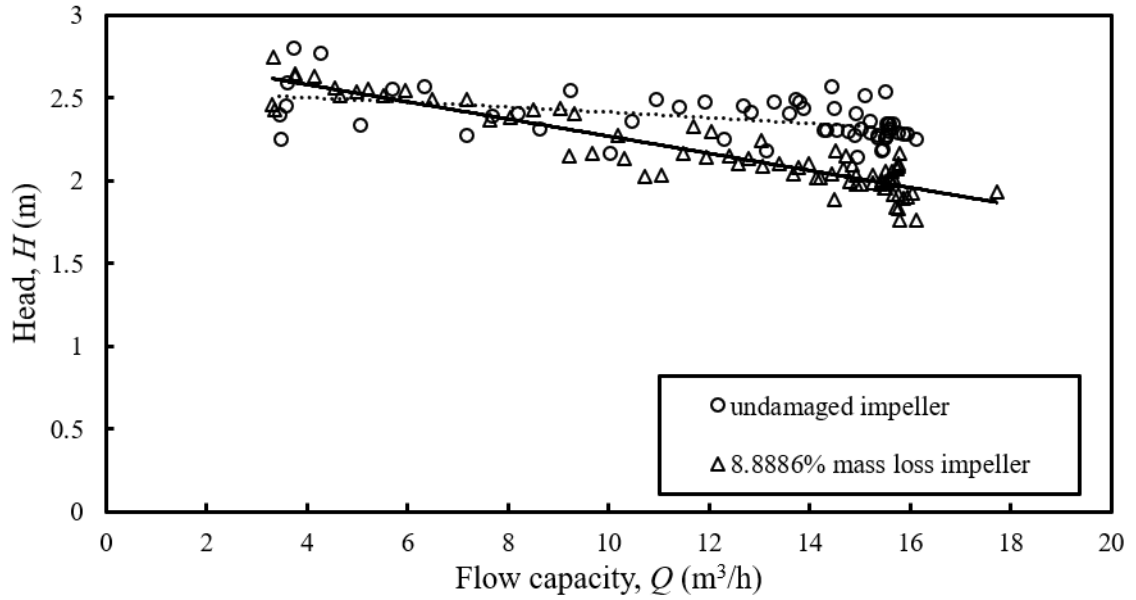




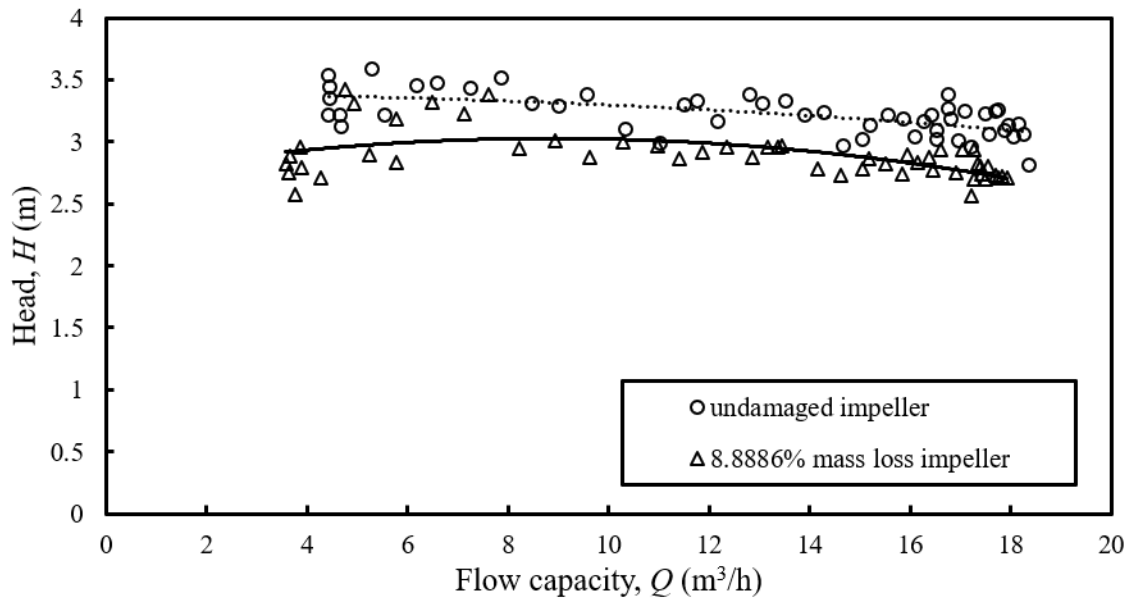
A.9. Head-flow capacity relationship at 1650 rpm & 5wt.% concentration after 24 hours  
1500 rpm wearing



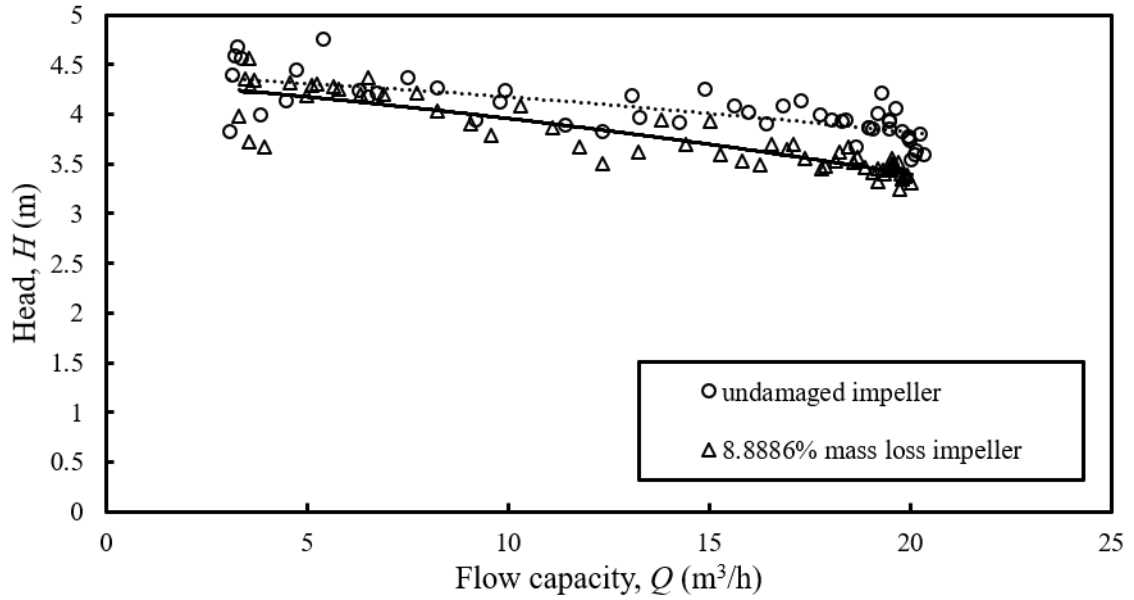
A.10. Head-flow capacity relationship at 1750 rpm & 5wt.% concentration after 24 hours  
1500 rpm wearing



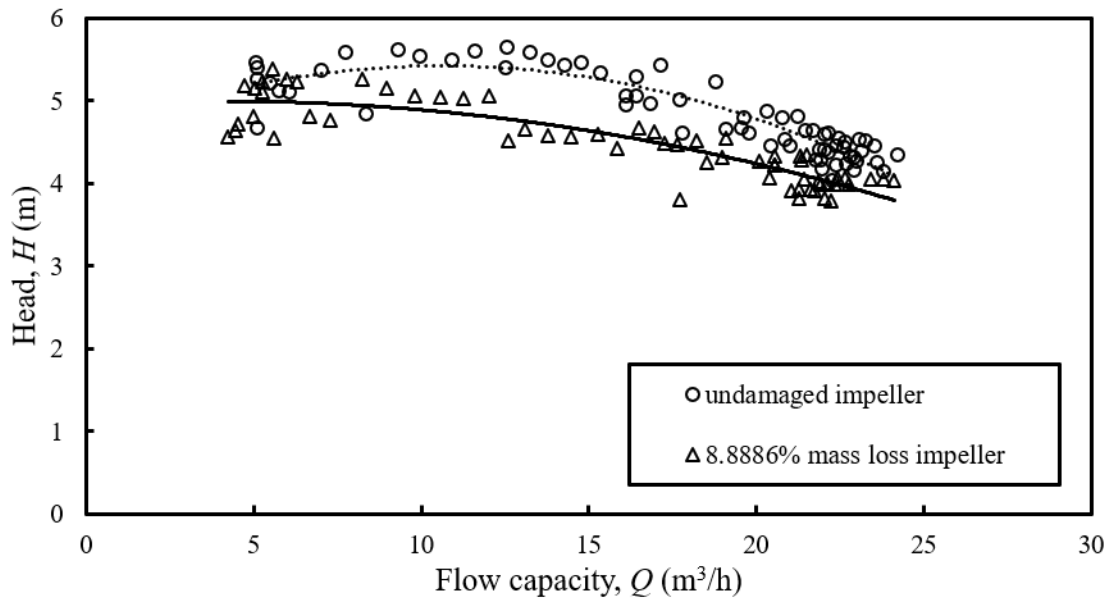
A.11. Head-flow capacity relationship at 850 rpm & 5wt.% concentration after 24 hours  
1750 rpm wearing



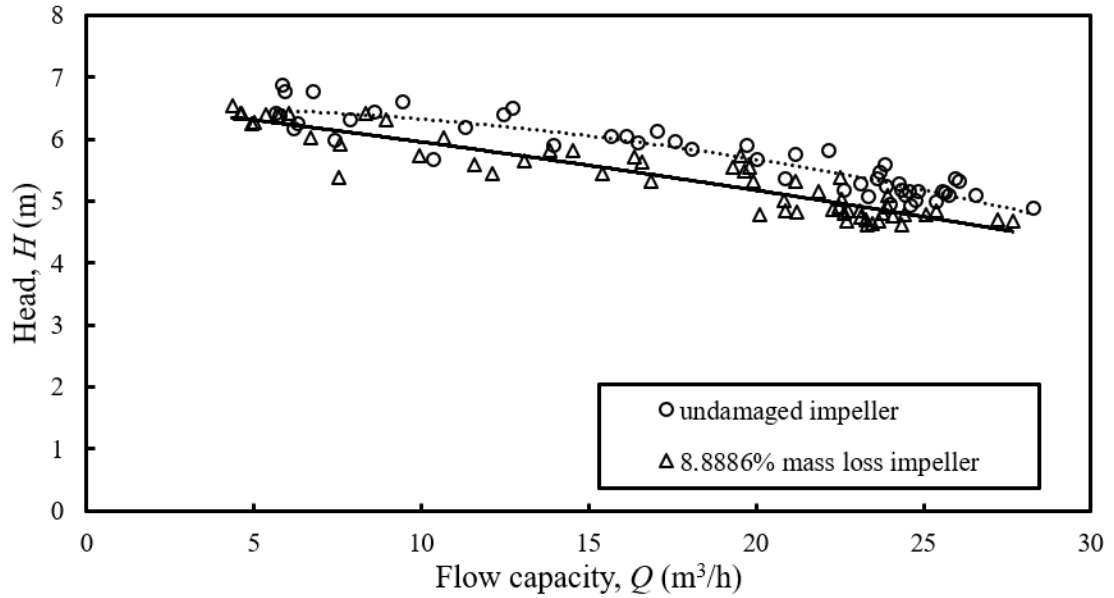
A.12. Head-flow capacity relationship at 950 rpm & 5wt.% concentration after 24 hours  
1750 rpm wearing



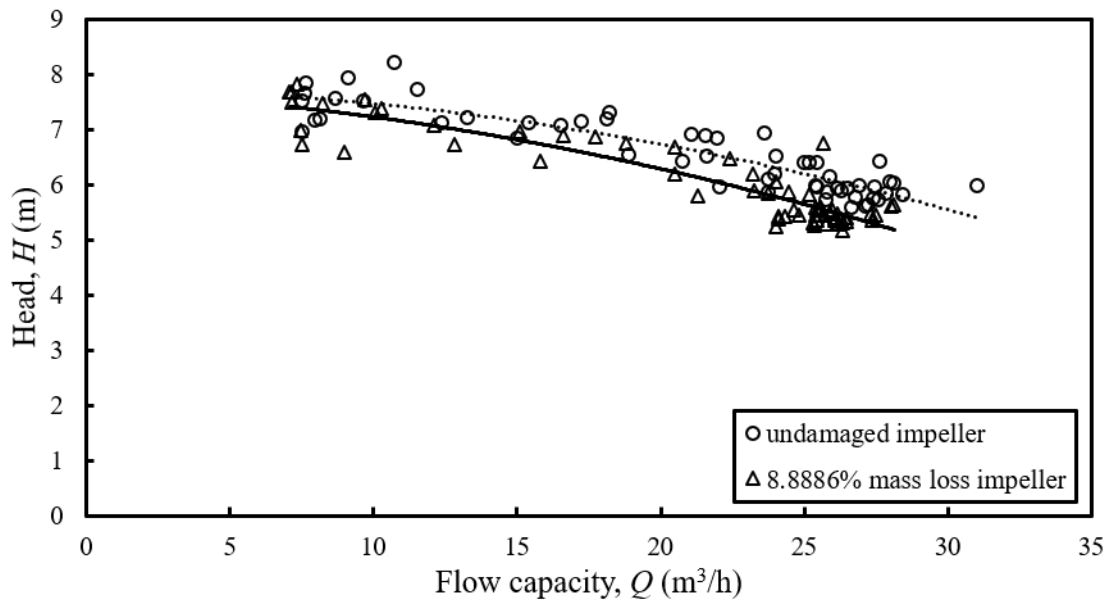
A.13. Head-flow capacity relationship at 1050 rpm & 5wt.% concentration after 24 hours  
1750 rpm wearing



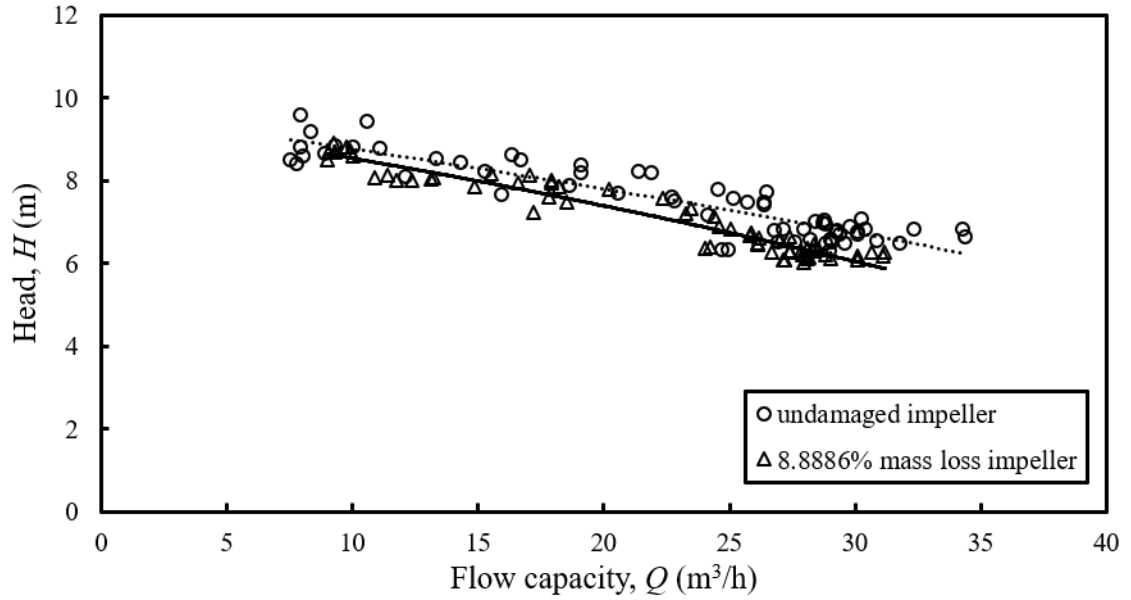
A.14. Head-flow capacity relationship at 1150 rpm & 5wt.% concentration after 24 hours  
1750 rpm wearing



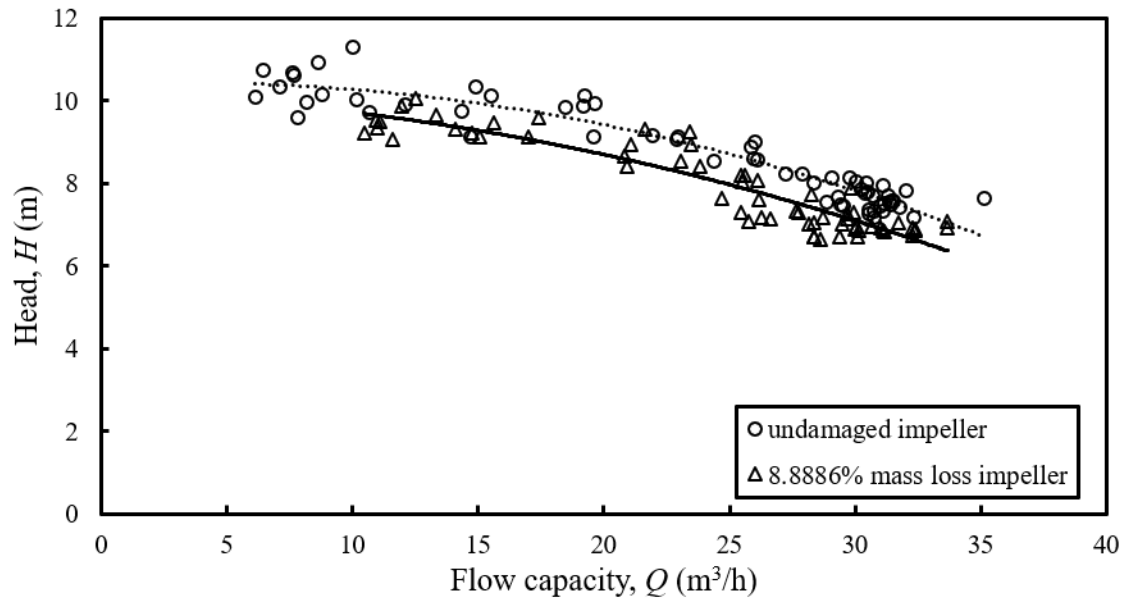
A.15. Head-flow capacity relationship at 1250 rpm & 5wt.% concentration after 24 hours  
1750 rpm wearing



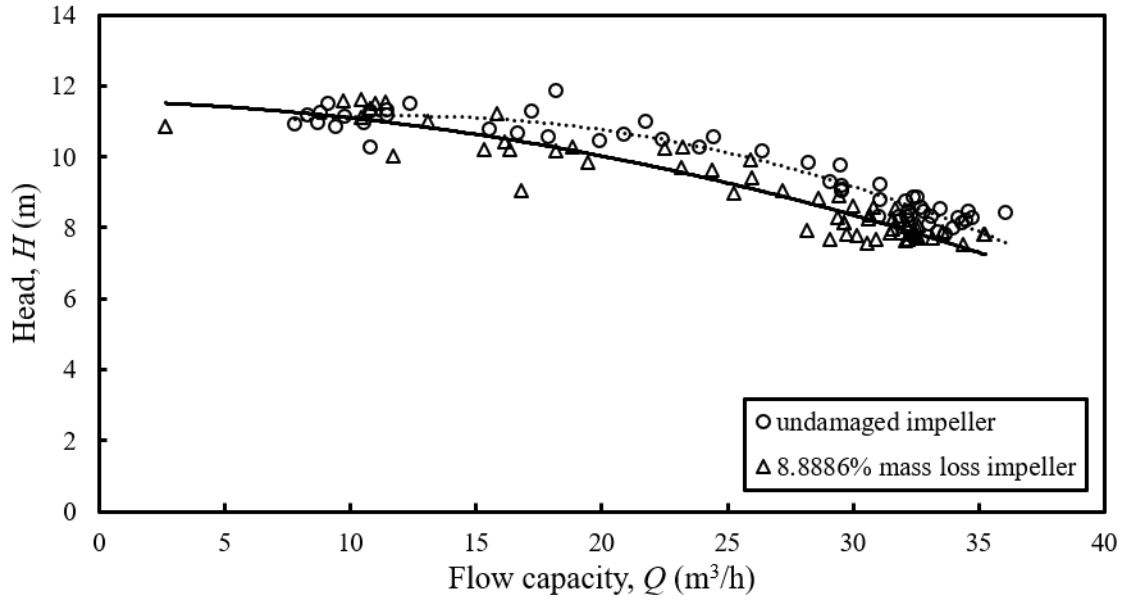
A.16. Head-flow capacity relationship at 1350 rpm & 5wt.% concentration after 24 hours  
1750 rpm wearing



A.17. Head-flow capacity relationship at 1450 rpm & 5wt.% concentration after 24 hours  
1750 rpm wearing

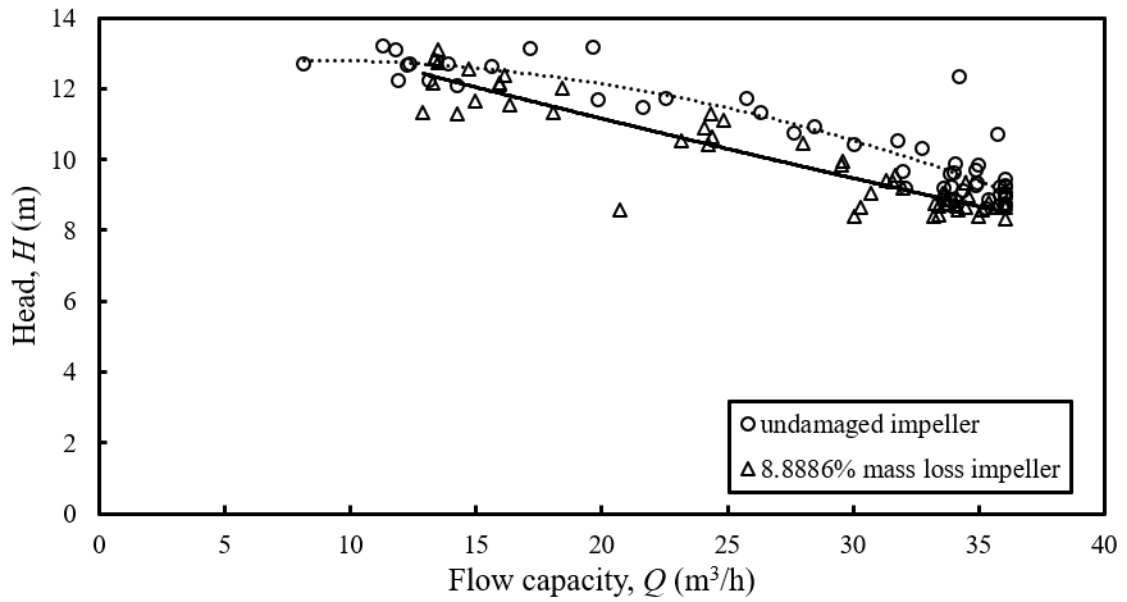


A.18. Head-flow capacity relationship at 1550 rpm & 5wt.% concentration after 24 hours  
1750 rpm wearing



A.19. Head-flow capacity relationship at 1650 rpm & 5wt.% concentration after 24 hours

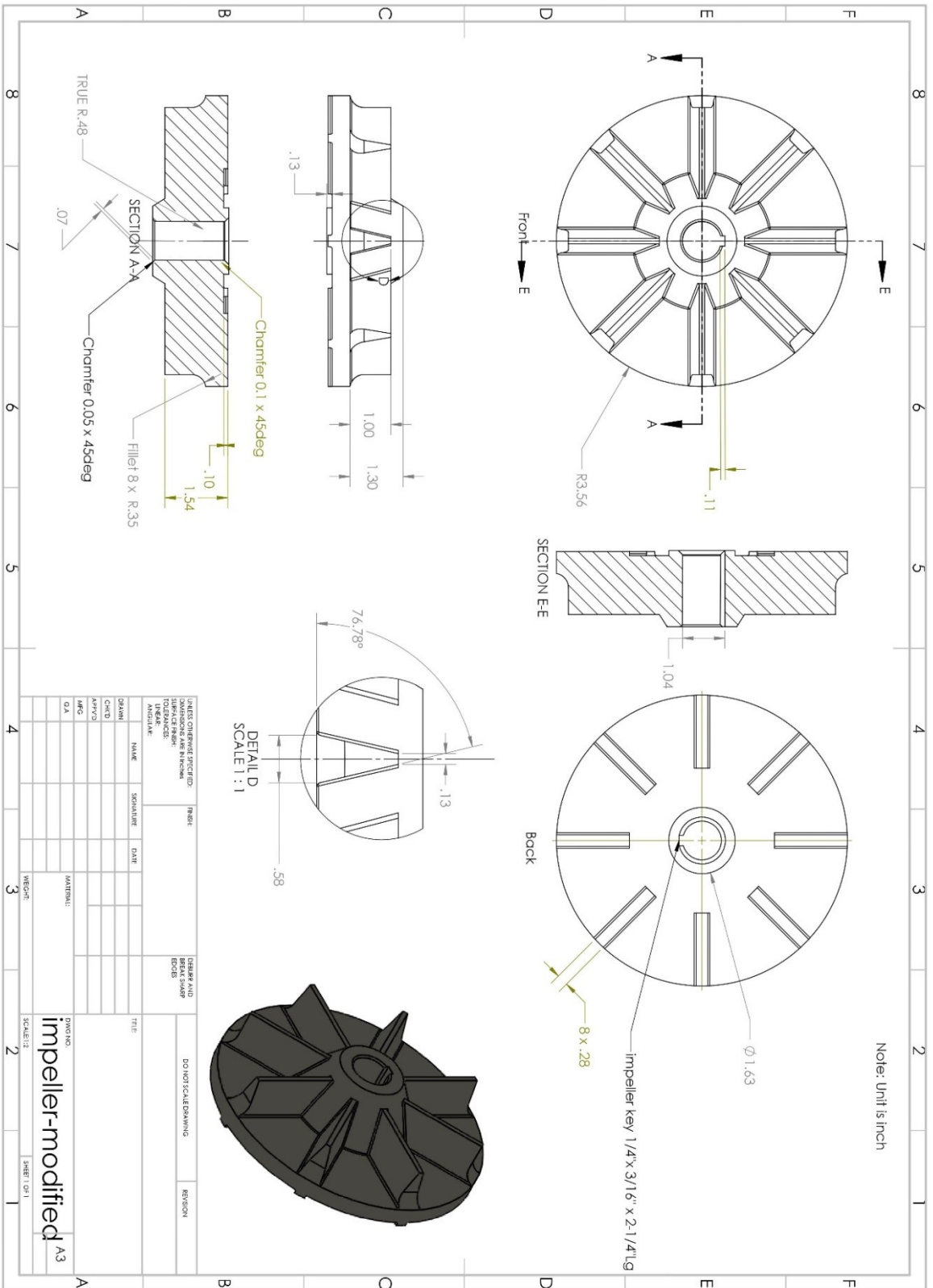
1750 rpm wearing



A.20. Head-flow capacity relationship at 1750 rpm & 5wt.% concentration after 24 hours

1750 rpm wearing

## **B.2D drawing for tested samples**

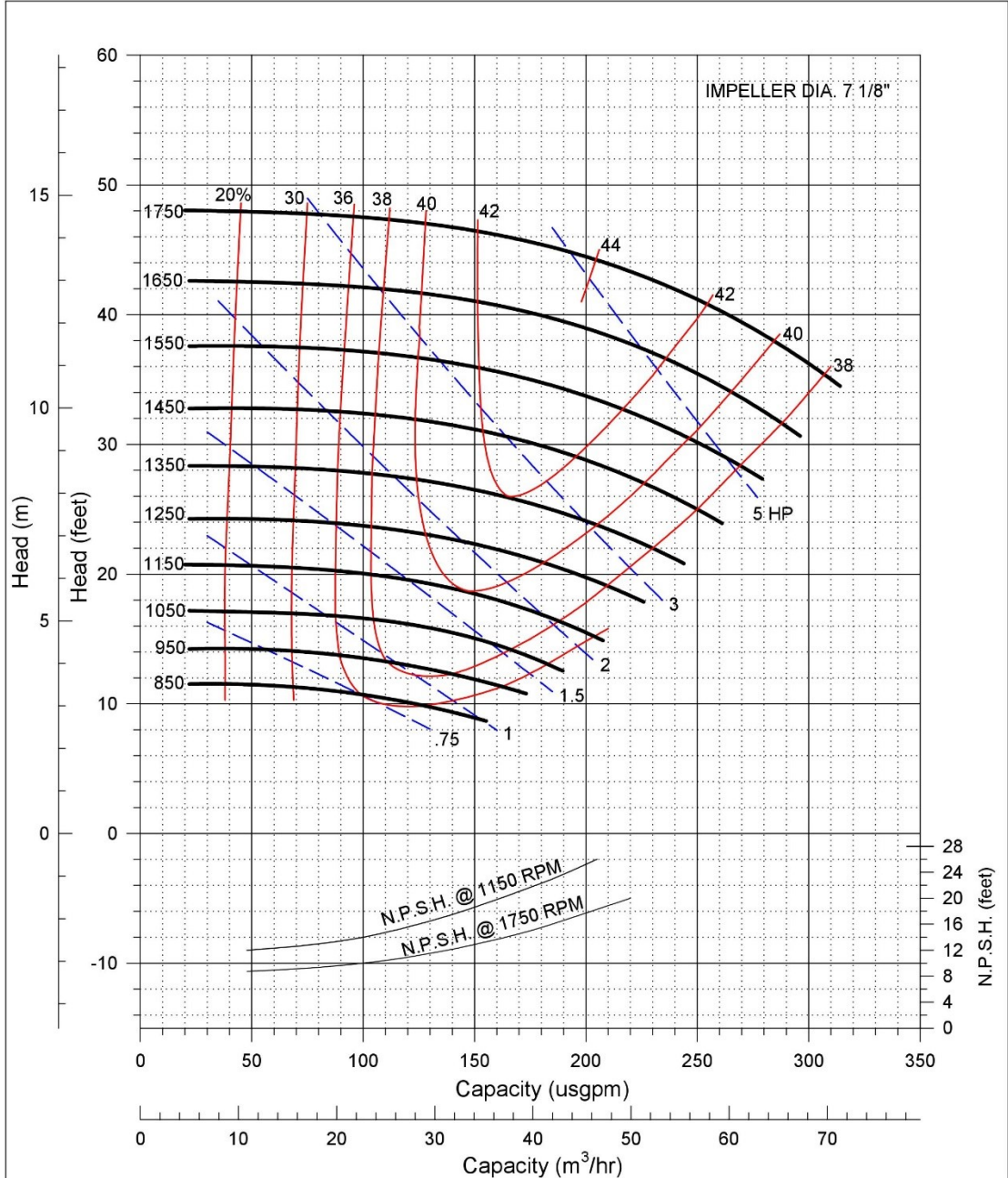



Note: Unit is Inch

UNLESS OTHERWISE SPECIFIED:		FINISH		DRAWN AND CHECKED	
DIMENSIONS ARE IN INCHES		SURFACE FINISH		SCALE AND DATE	
TOLERANCES:		MATERIAL		TITLE	
FRACTIONS		SPECIFICATIONS		DO NOT SCALE DRAWING	
DECIMALS		TEMPERATURE		REVISION	
ANGLES		TREATMENT		PART 1 OF 1	
DESIGN	NAME	SIGNATURE	DATE	PROJECT	
CHKD				SCALE: 1:1	
APP'CD				PROJECT NO.	
MG				impeller-modified	
QA				A3	
MATERIAL:				SCALE: 1:1	
SPECIFICATIONS:				PROJECT NO.	

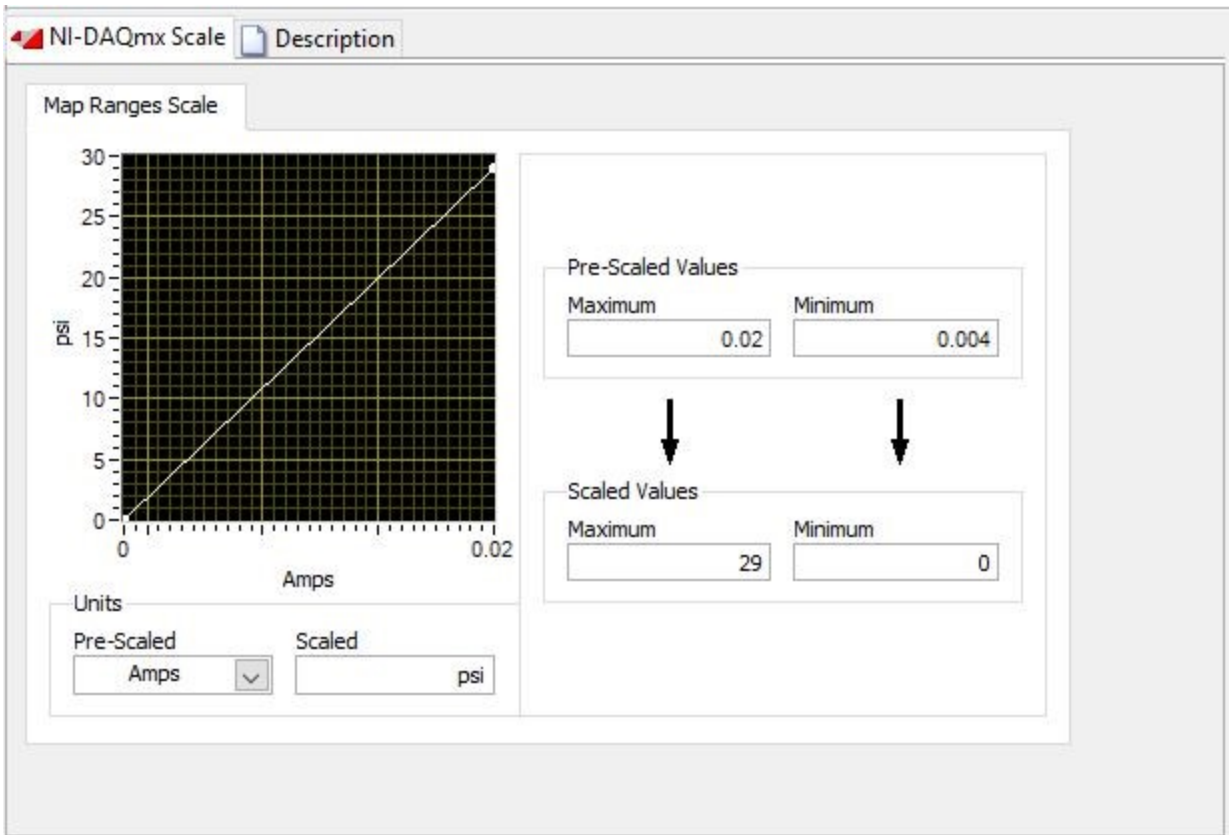


**C.Data sheet of performance curves of the pump (Given  
by manufacturer)**



<b>HAYWARD GORDON</b>  <b>Performance Curves</b> <b>TORUS Pumps</b>	MODEL	SIZE	CURVE	REV.
	XR2(7)	2 x 3 x 7	095-10110	3
	DRN. DATE 04.03.96 REV. DATE 10.05.07	DRN. J.M. REV. LF	MAX SPHERE 2"	SPEED VARIABLE

## **D. NI-DAQmx interface**



A.21. NI-DAQmx interface of scaling of pressure transducer

Express Task Connection Diagram

Channel	Value
Current_0	0
Current_1	0
Current_2	0
Current_3	0

Table  Display Type

---

Configuration **Triggering** Advanced Timing Logging

Channel Settings

- Current\_0
- Current\_1
- Current\_2**
- Current\_3

*Click the Add Channels button (+) to add more channels to the task.*

**Current Input Setup**

Settings **Device** Calibration

Signal Input Range

Max  Scaled Units

Min

Shunt Resistor

Terminal Configuration

Custom Scaling

Timing Settings

Acquisition Mode  Samples to Read  Rate (Hz)

A.22. Interface of setting data acquisition system

**E. Dimensional analysis on wear rate from particle perspective**

In this work, to investigate the abrasive wear rate of the impeller from particle perspective, it should depend on flow velocity, Hardness of the target material, particle diameter.

$$[v] = \frac{L}{T}$$

$$[H_v] = \frac{M}{LT^2}$$

$$[D] = L$$

$$[E] = \frac{M}{T}$$

Then,

$$[E] = [v^a H_v^b D^c]$$

And

$$\frac{M}{T} = \left(\frac{L}{T}\right)^a \left(\frac{M}{LT^2}\right)^b (L)^c$$

Then, the system is obtained

$$b = 1$$

$$a - b + c = 0$$

$$-a - 2b = -1$$

Then:

$$a = -1$$

$$b = 1$$

$$c = 2$$

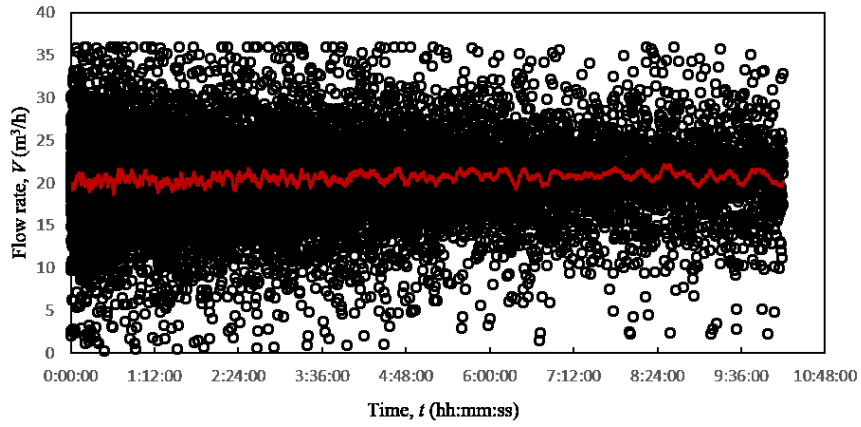
Thus,

$$E = \alpha \frac{H_v D^2}{v}$$

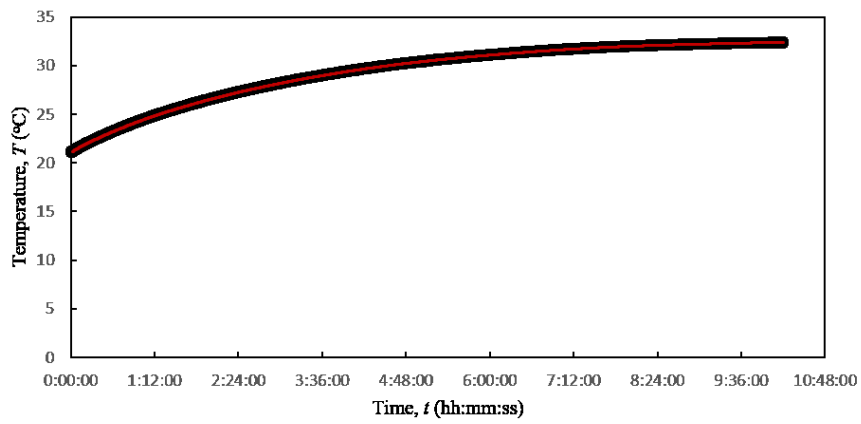
In conclusion, with dimensional analysis, the wear rate for a single particle is proportional to  $\frac{H_v D^2}{v}$ .



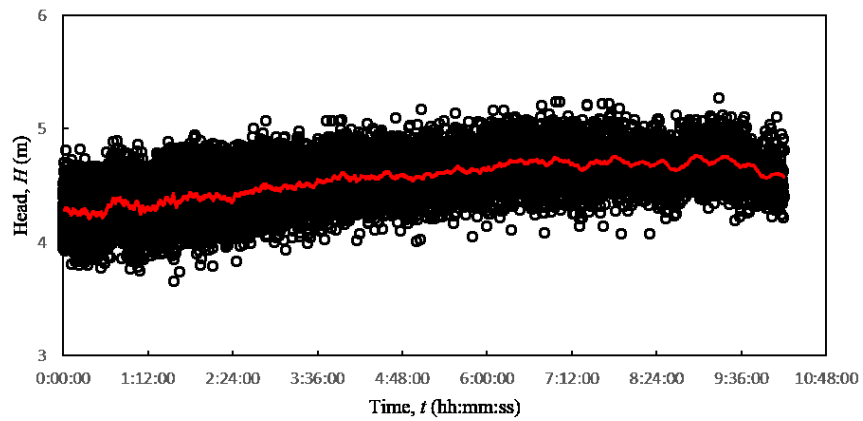
## **F. Experimental data of wear tests**



a) Flow rate vs. time for 1200RPM, 5wt.% solids concentration

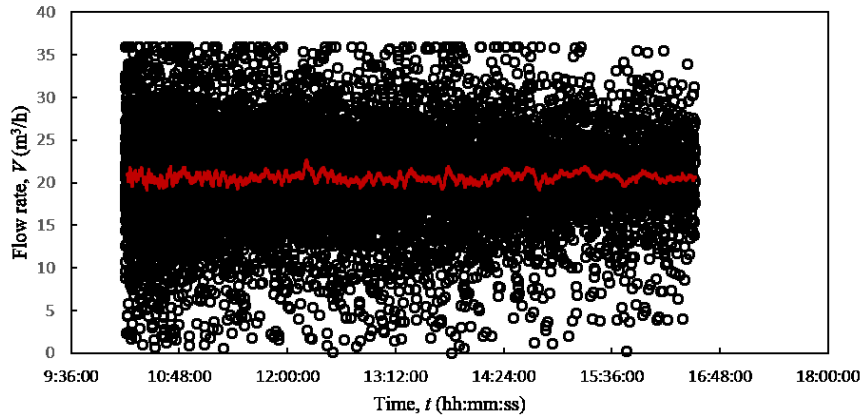


b) Temperature vs. time for 1200RPM, 5wt.% solids concentration

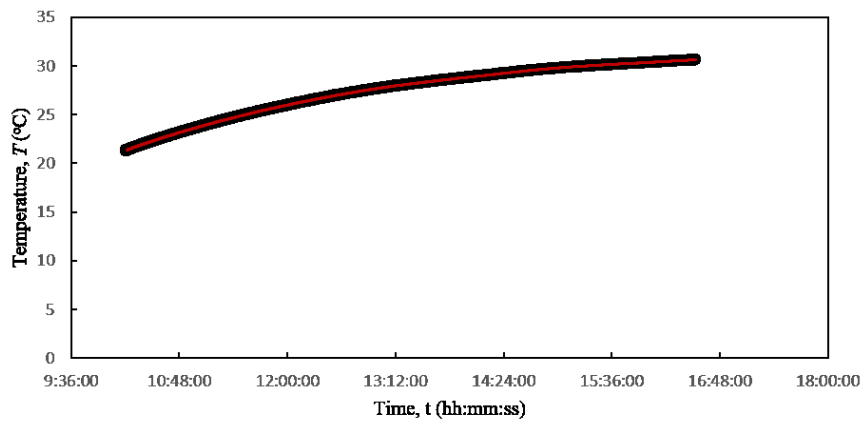


c) Head vs. time for 1200RPM, 5wt.% solids concentration

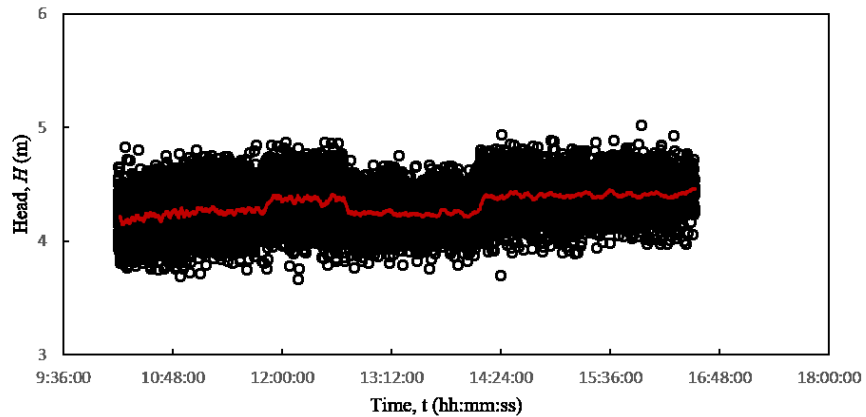
A.23. Flow rate, temperature and head vs. time in the experiments for 1200 rpm and 5wt.% solids concentration, part 1



a) Flow rate vs. time for 1200RPM, 5wt.% solids concentration

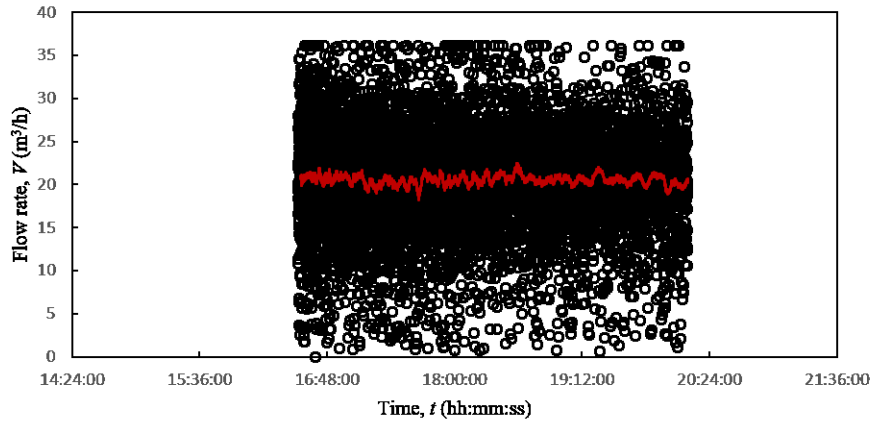


b) Temperature vs. time for 1200RPM, 5wt.% solids concentration

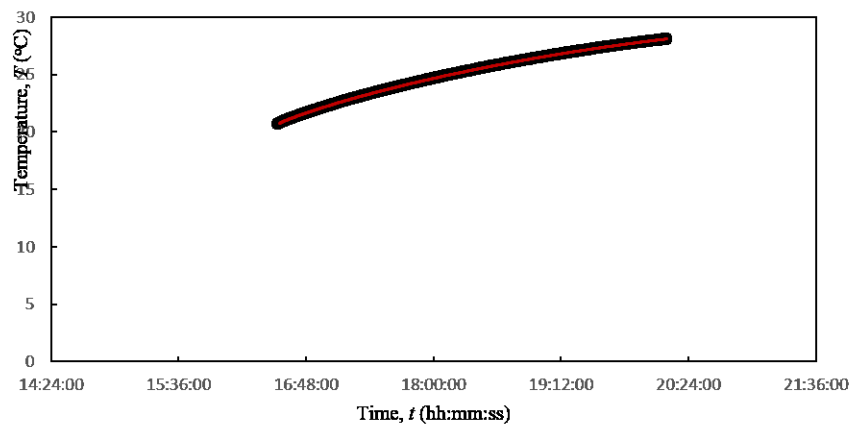


c) Head vs. time for 1200RPM, 5wt.% solids concentration

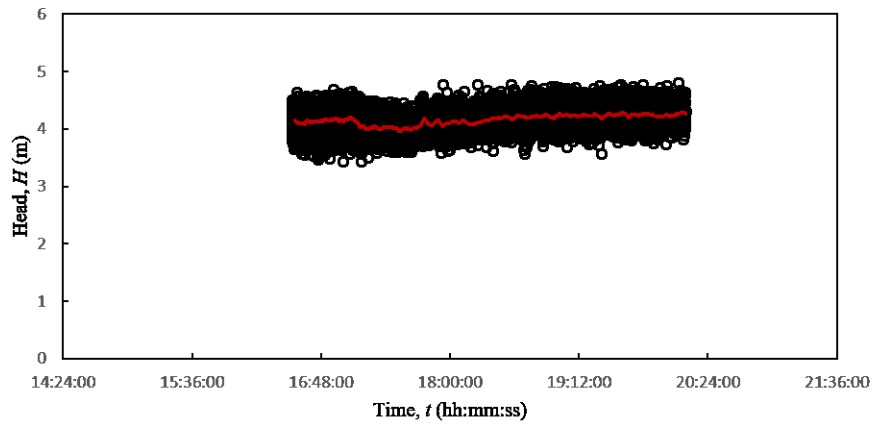
A.24. Flow rate, temperature and head vs. time in the experiments for 1200 rpm and 5wt.% solids concentration, part 2



a) Flow rate vs. time for 1200RPM, 5wt.% solids concentration

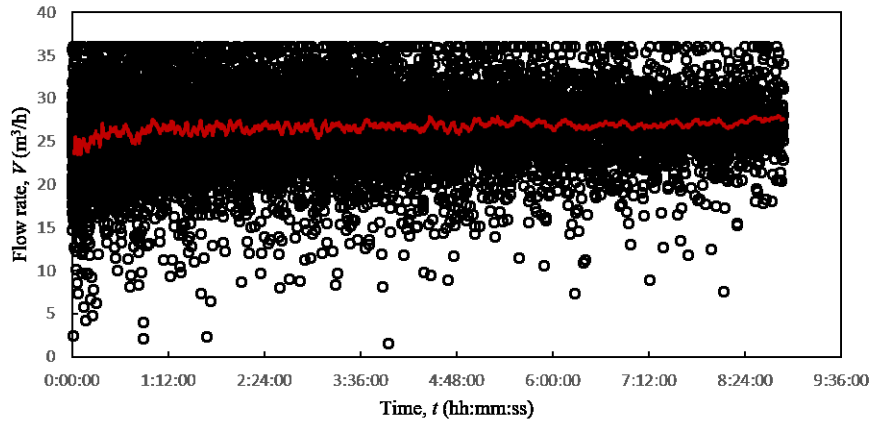


b) Temperature vs. time for 1200RPM, 5wt.% solids concentration

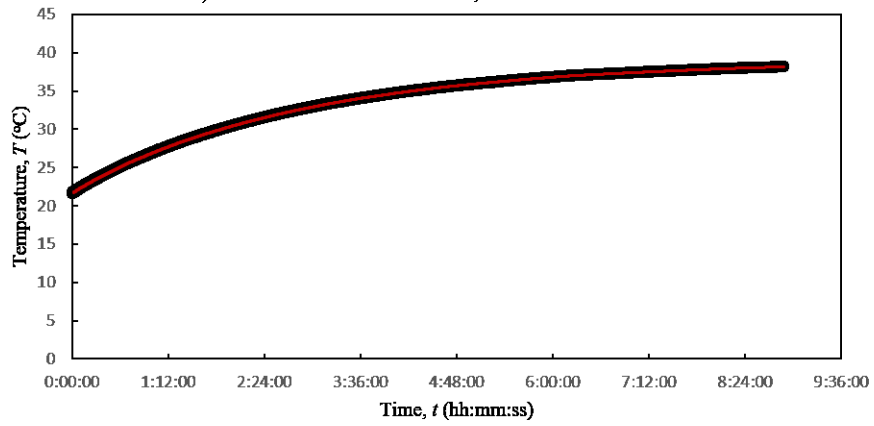


c) Head vs. time for 1200RPM, 5wt.% solids concentration

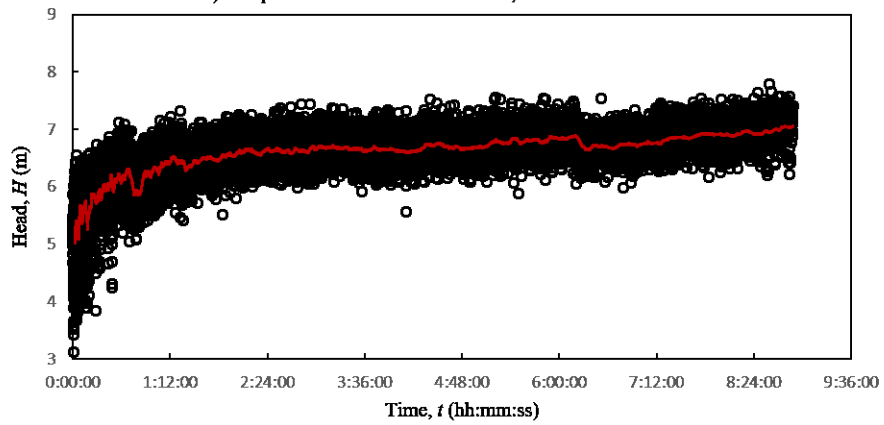
A.25. Flow rate, temperature and head vs. time in the experiments for 1200 rpm and 5wt.% solids concentration, part 3



a) Flow rate vs. time for 1500RPM, 5wt.% solids concentration

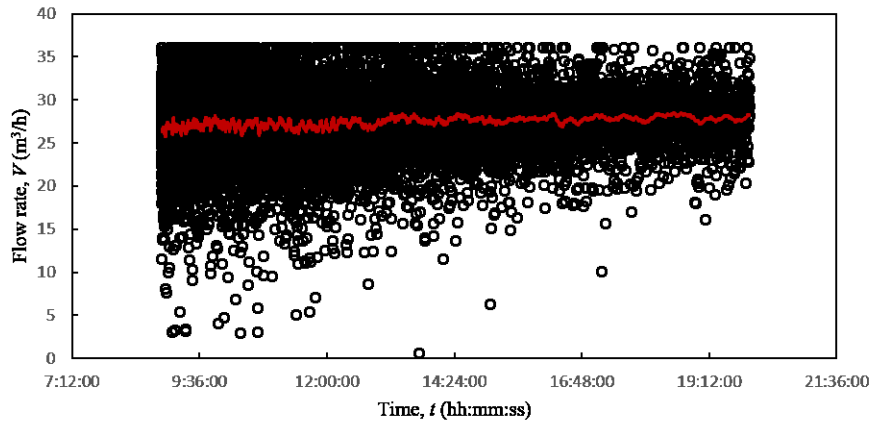


b) Temperature vs. time for 1500RPM, 5wt.% solids concentration

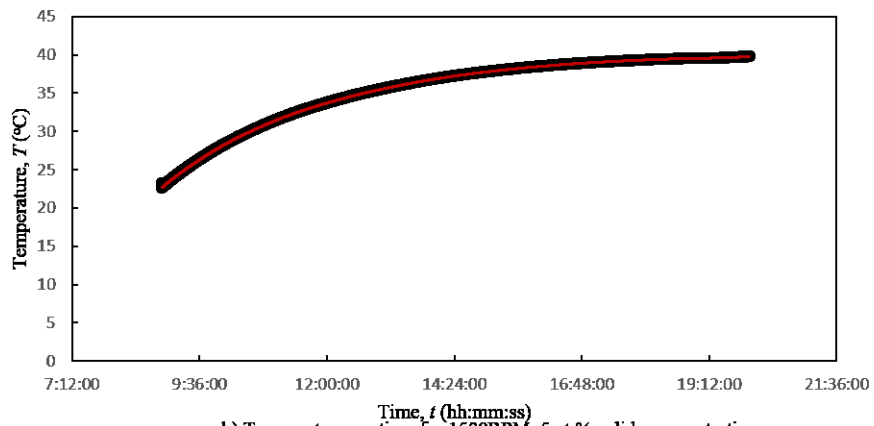


c) Head vs. time for 1500RPM, 5wt.% solids concentration

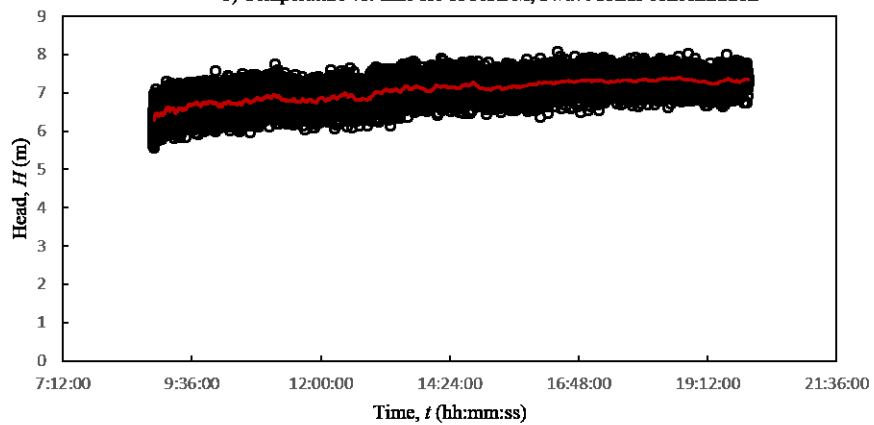
A.26. Flow rate, temperature and head vs. time in the experiments for 1500 rpm and 5wt.% solids concentration, part 1



a) Flow rate vs. time for 1500RPM, 5wt.% solids concentration

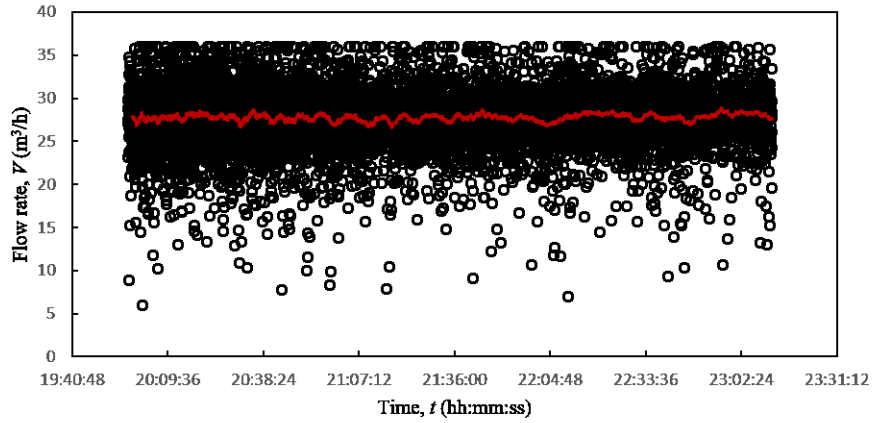


b) Temperature vs. time for 1500RPM, 5wt.% solids concentration

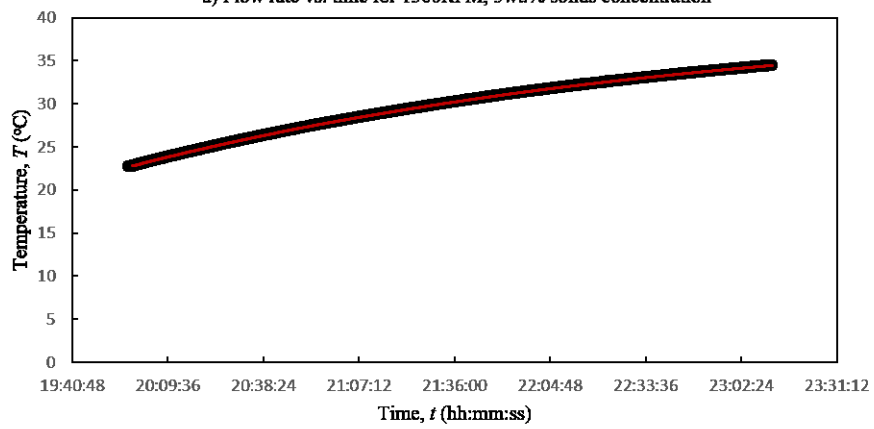


c) Head vs. time for 1500RPM, 5wt.% solids concentration

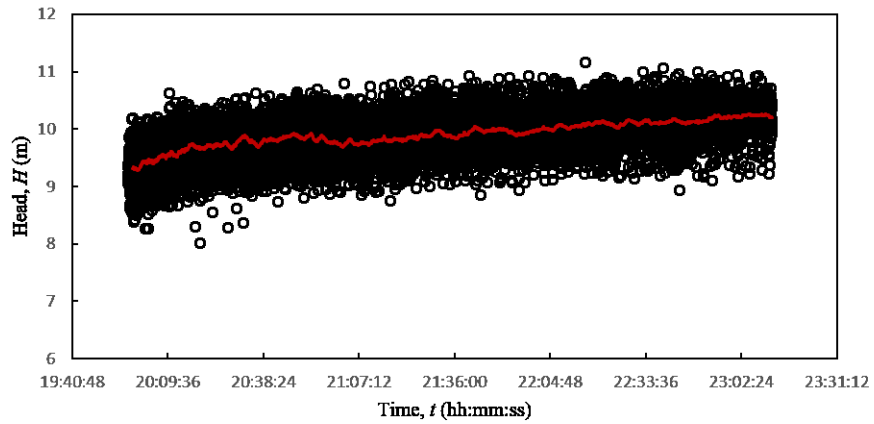
A.27. Flow rate, temperature and head vs. time in the experiments for 1500 rpm and 5wt.% solids concentration, part 2



a) Flow rate vs. time for 1500RPM, 5wt.% solids concentration

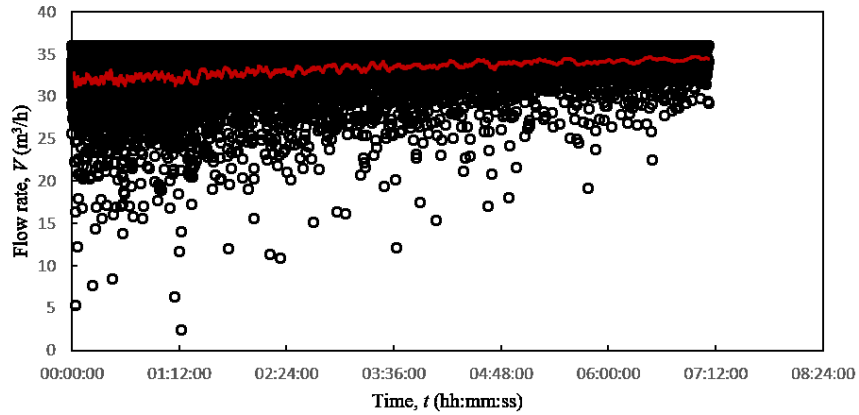


b) Temperature vs. time for 1500RPM, 5wt.% solids concentration

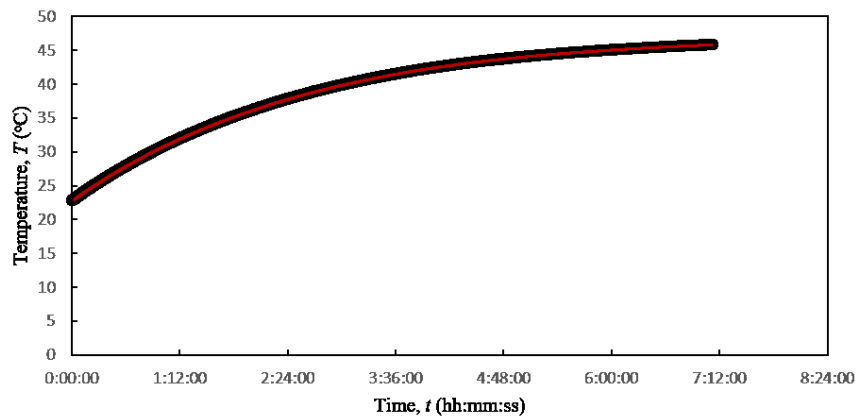


c) Head vs. time for 1500RPM, 5wt.% solids concentration

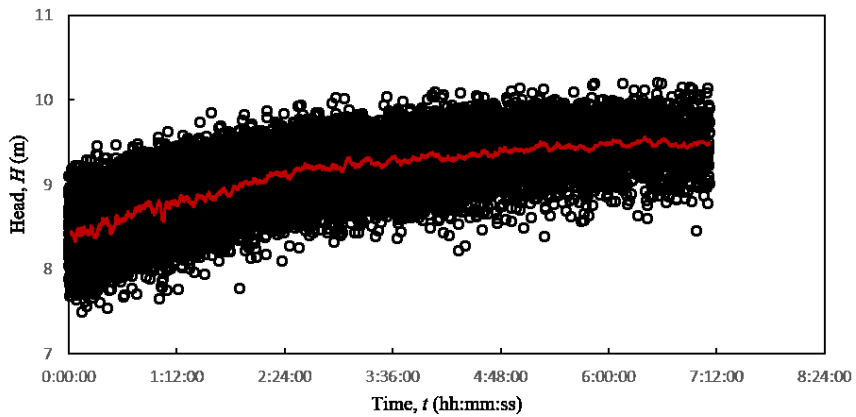
A.28. Flow rate, temperature and head vs. time in the experiments for 1500 rpm and 5wt.% solids concentration, part 3



a) Flow rate vs. time for 1750RPM, 5wt.% solids concentration



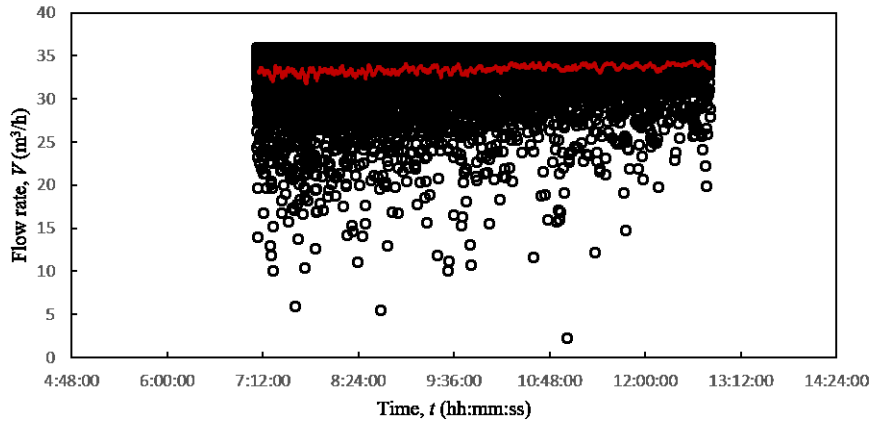
b) Temperature vs. time for 1750RPM, 5wt.% solids concentration



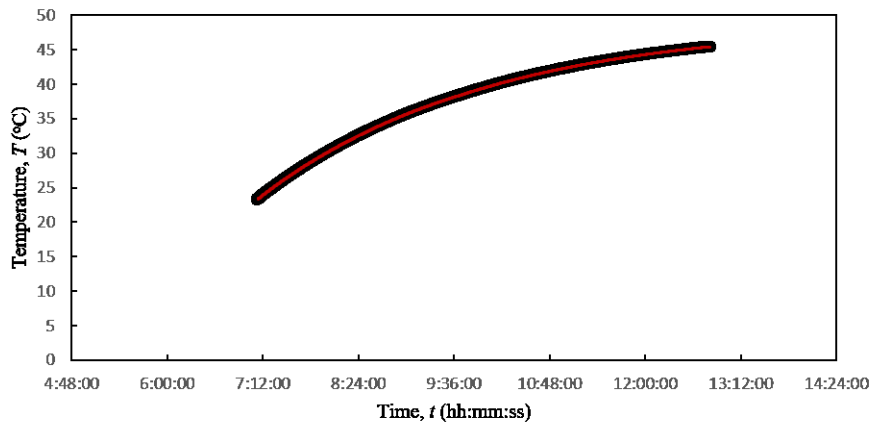
c) Head vs. time for 1750RPM, 5wt.% solids concentration

A.29. Flow rate, temperature and head vs. time in the experiments for 1750 rpm and 5wt.% solids concentration, part 1

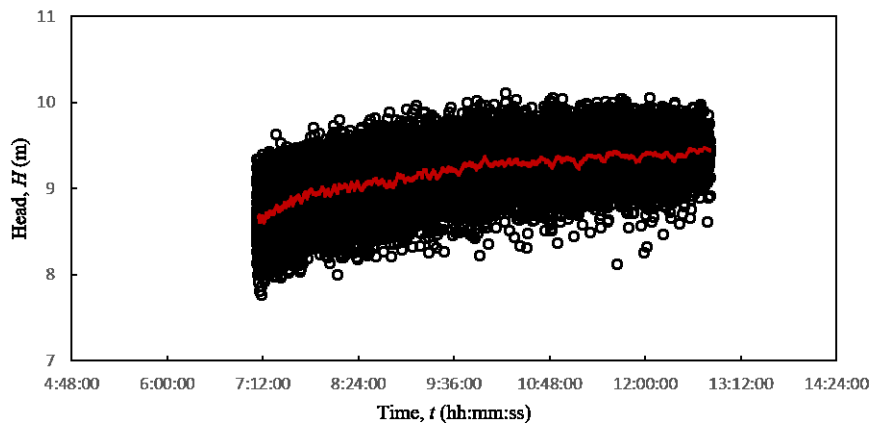




a) Flow rate vs. time for 1750RPM, 5wt.% solids concentration

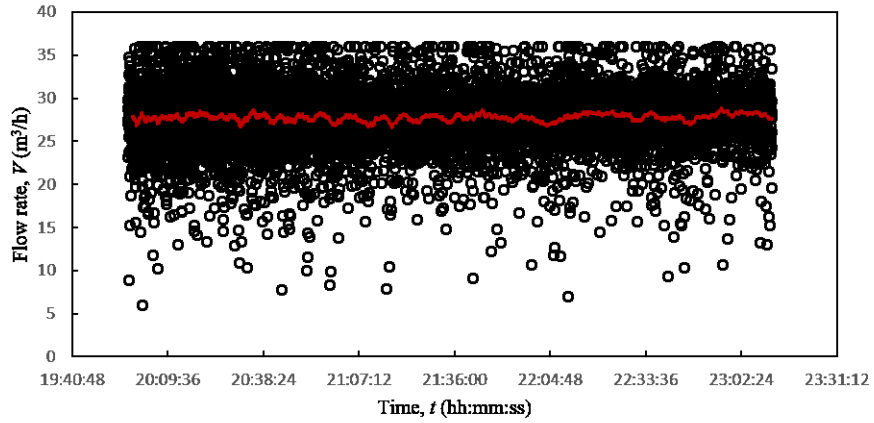


b) Temperature vs. time for 1750RPM, 5wt.% solids concentration

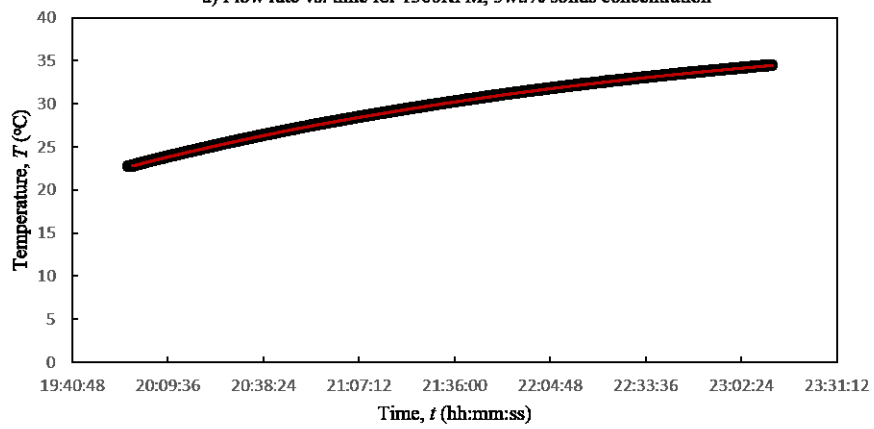


c) Head vs. time for 1750RPM, 5wt.% solids concentration

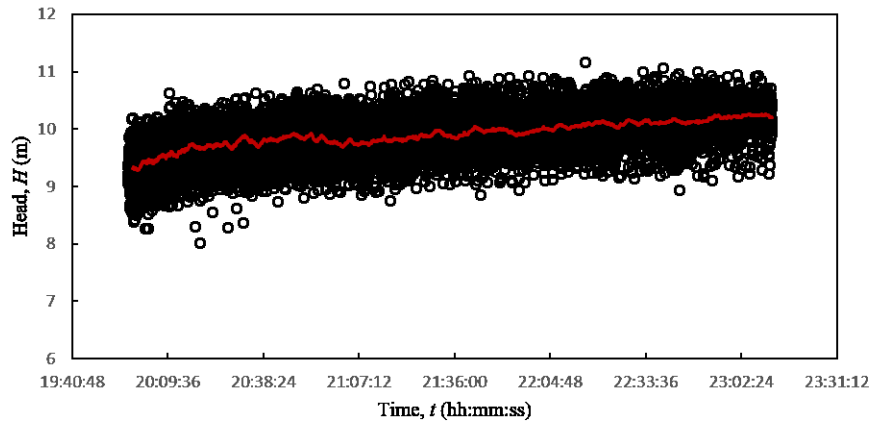
A.30. Flow rate, temperature and head vs. time in the experiments for 1750 rpm and 5wt.% solids concentration, part 2



a) Flow rate vs. time for 1500RPM, 5wt.% solids concentration

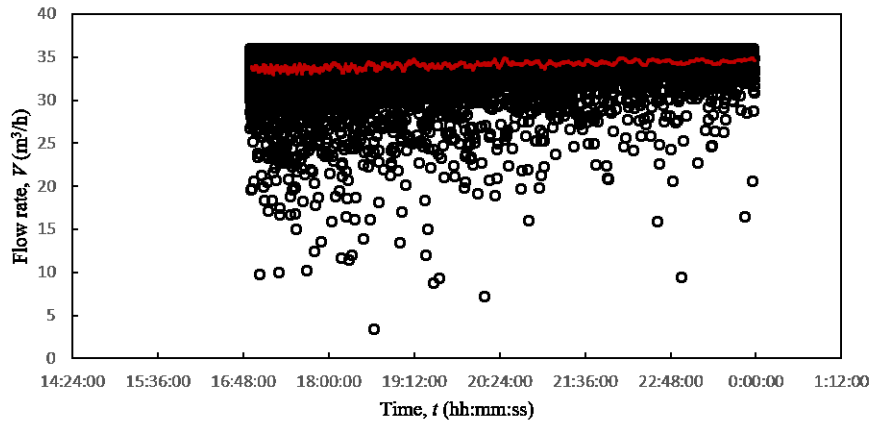


b) Temperature vs. time for 1500RPM, 5wt.% solids concentration

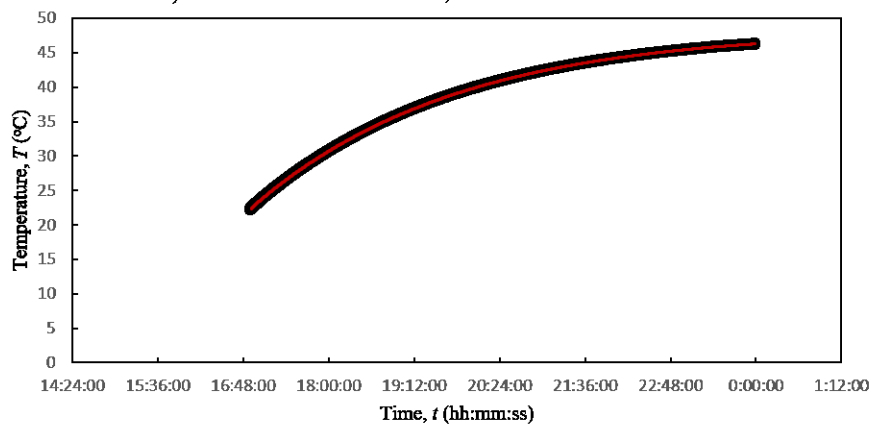


c) Head vs. time for 1500RPM, 5wt.% solids concentration

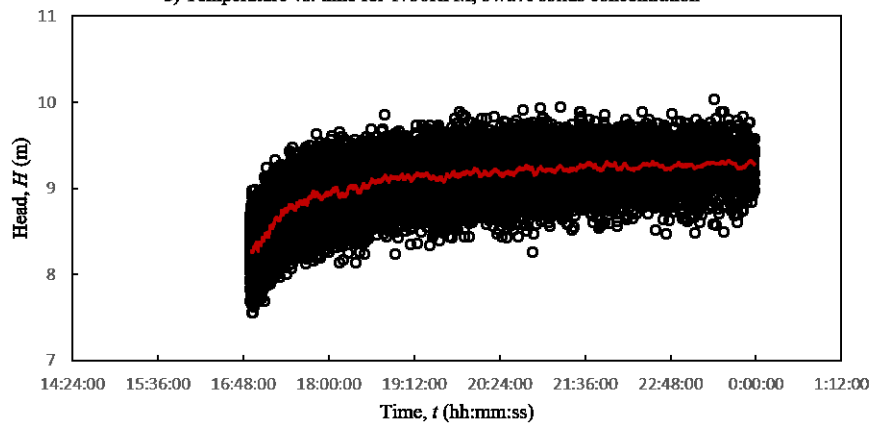
A.31. Flow rate, temperature and head vs. time in the experiments for 1750 rpm and 5wt.% solids concentration, part 3



a) Flow rate vs. time for 1750RPM, 5wt.% solids concentration

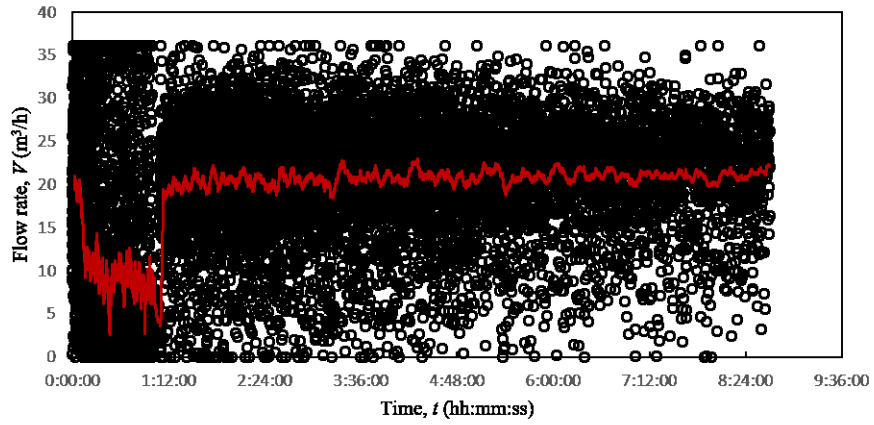


b) Temperature vs. time for 1750RPM, 5wt.% solids concentration

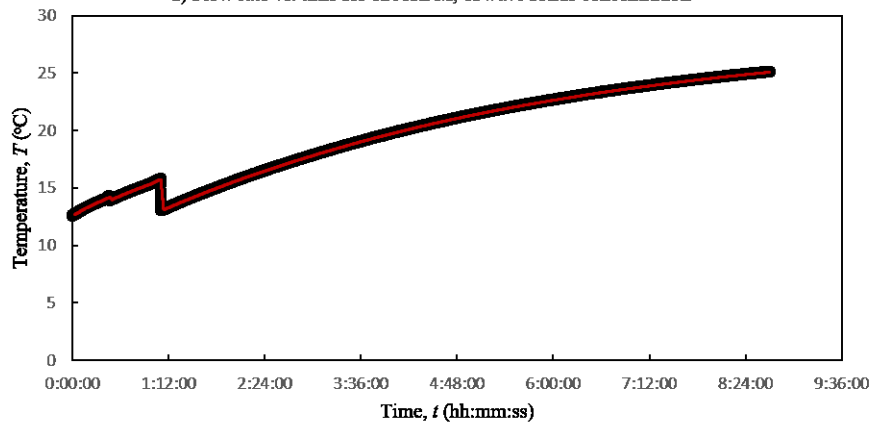


c) Head vs. time for 1750RPM, 5wt.% solids concentration

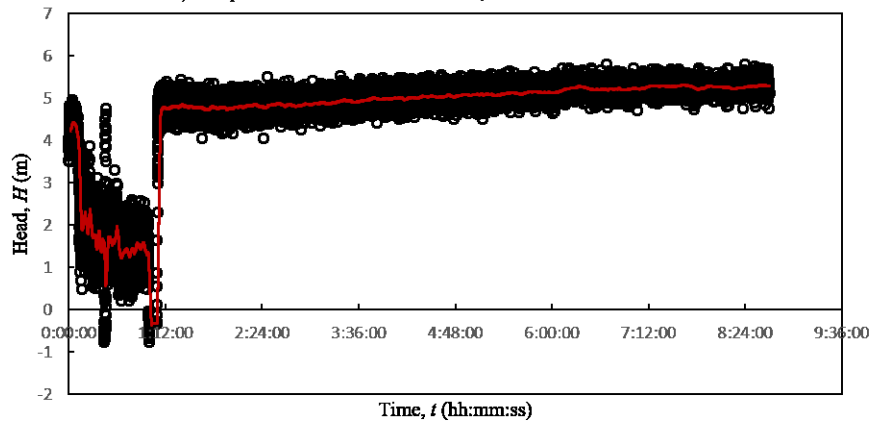
A.32. Flow rate, temperature and head vs. time in the experiments for 1750 rpm and 5wt.% solids concentration, part 4



a) Flow rate vs. time for 1200RPM, 15wt.% solids concentration

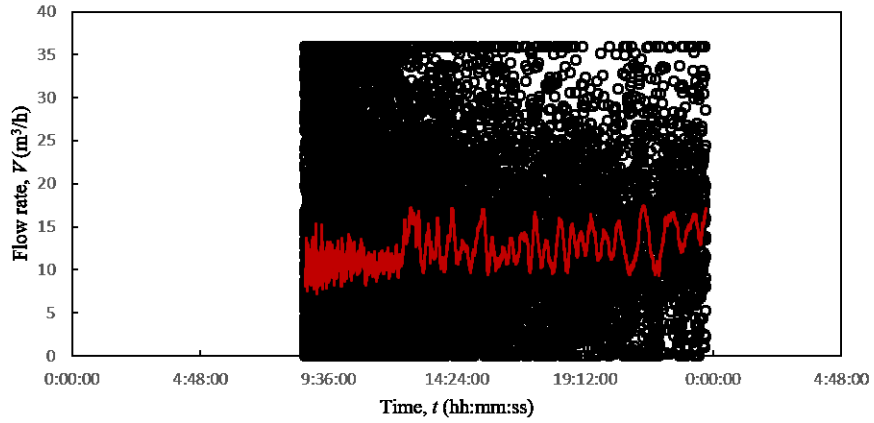


b) Temperature vs. time for 1200RPM, 15wt.% solids concentration

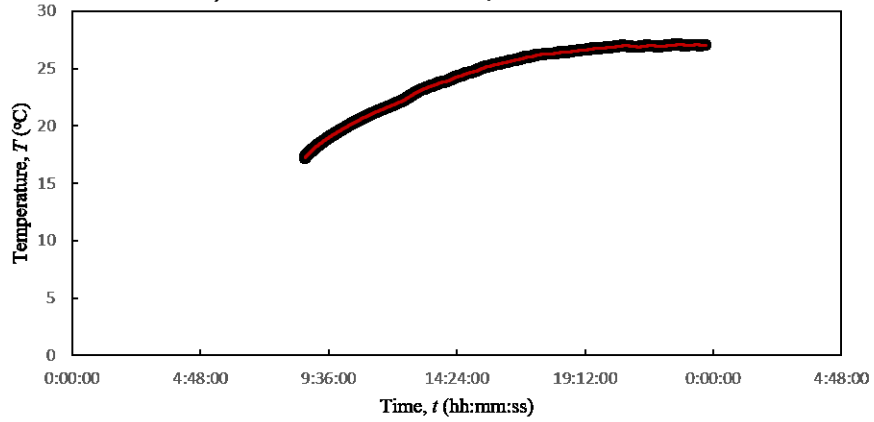


c) Head vs. time for 1200RPM, 15wt.% solids concentration

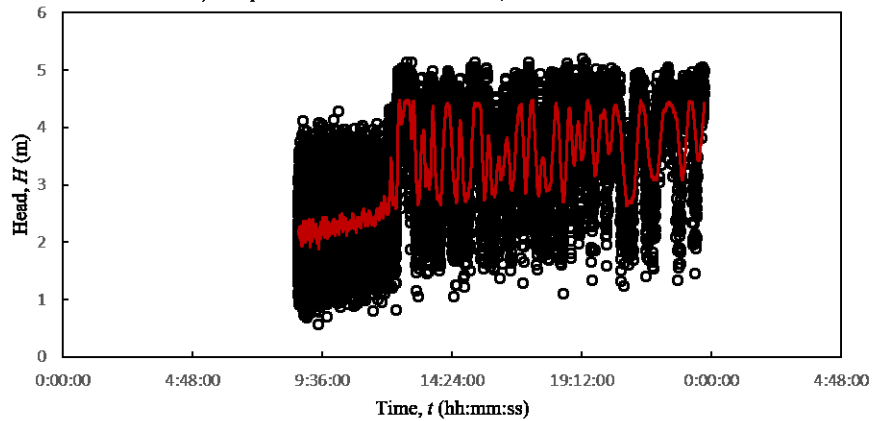
A.33. Flow rate, temperature and head vs. time in the experiments for 1200 rpm and 15wt.% solids concentration, part 1



a) Flow rate vs. time for 1200RPM, 15wt.% solids concentration

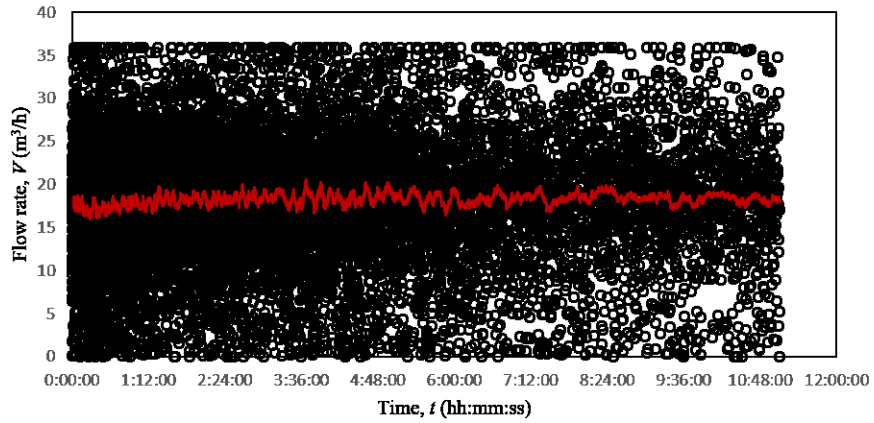


b) Temperature vs. time for 1200RPM, 15wt.% solids concentration

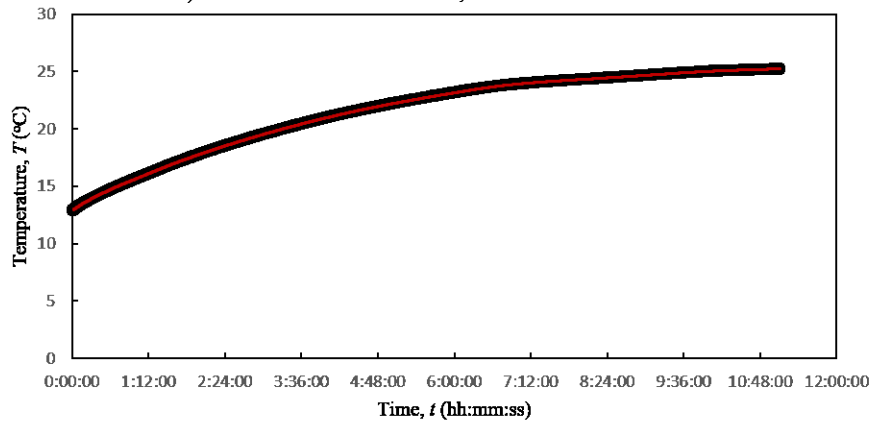


c) Head vs. time for 1200RPM, 15wt.% solids concentration

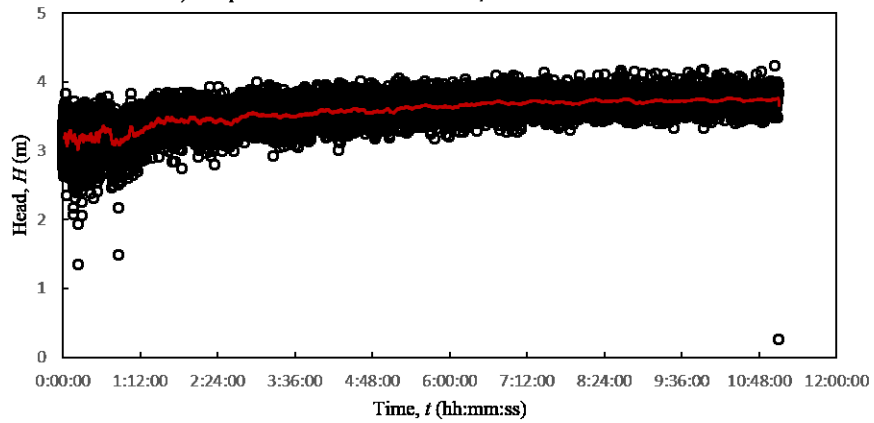
A.34. Flow rate, temperature and head vs. time in the experiments for 1200 rpm and 15wt.% solids concentration, part 2



a) Flow rate vs. time for 1050RPM, 5wt.% solids concentration

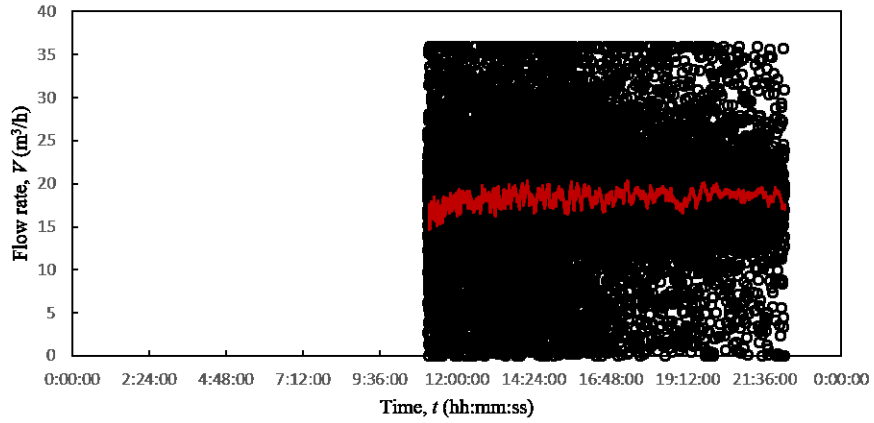


b) Temperature vs. time for 1050RPM, 5wt.% solids concentration

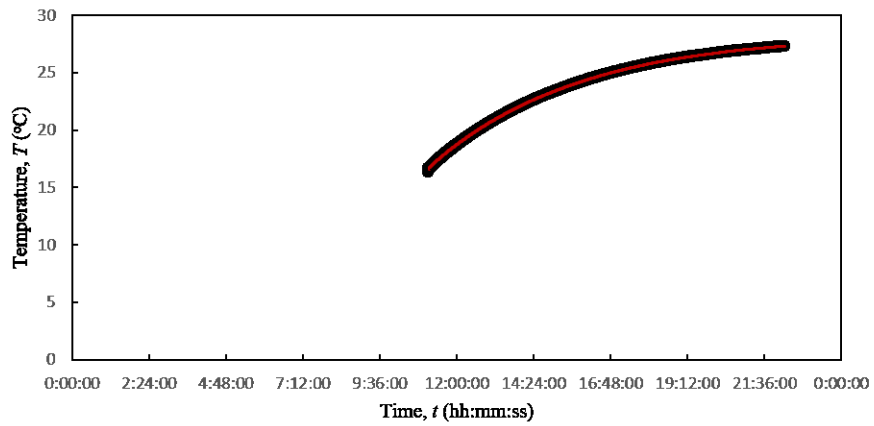


c) Head vs. time for 1050RPM, 5wt.% solids concentration

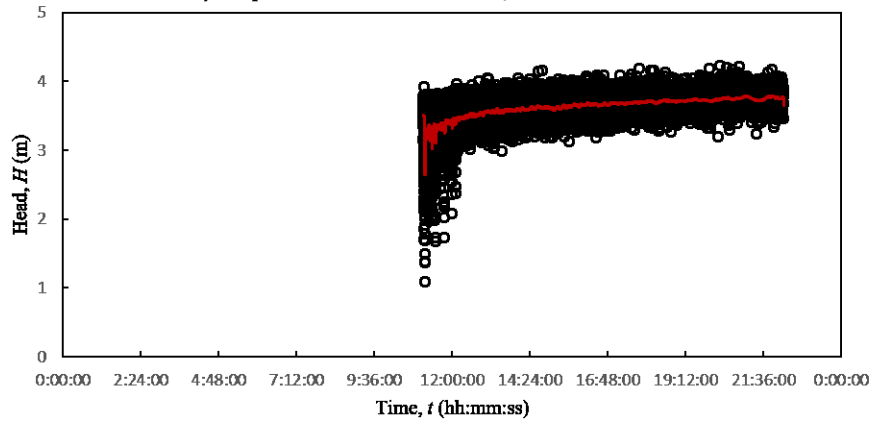
A.35. Flow rate, temperature and head vs. time in the experiments for 1050 rpm and 5wt.% solids concentration, part 1



a) Flow rate vs. time for 1050RPM, 5wt.% solids concentration

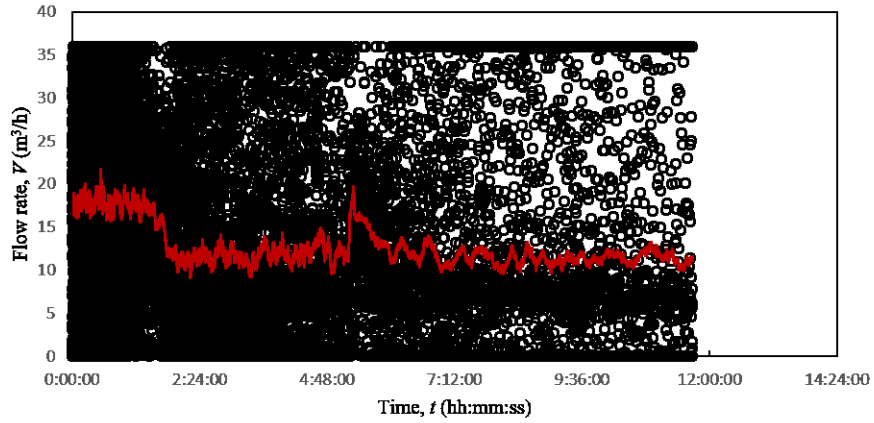


b) Temperature vs. time for 1050RPM, 5wt.% solids concentration

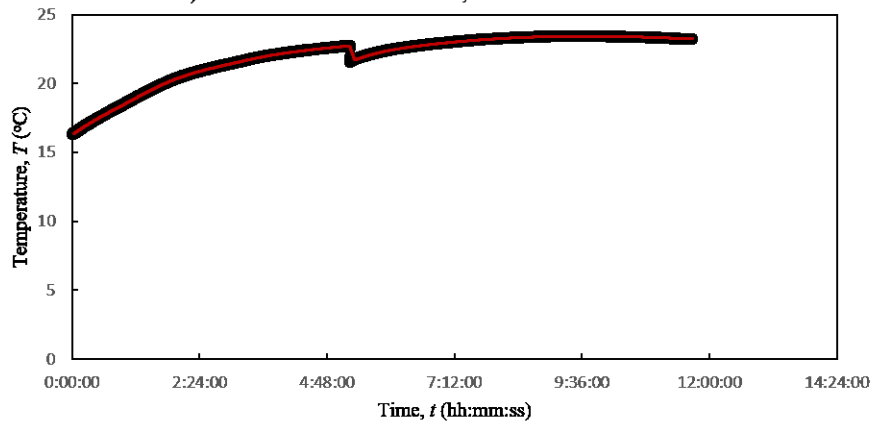


c) Head vs. time for 1050RPM, 5wt.% solids concentration

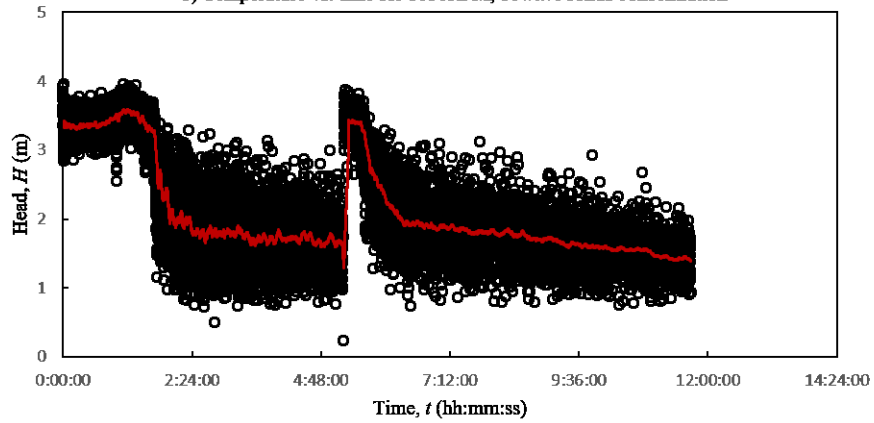
A.36. Flow rate, temperature and head vs. time in the experiments for 1050 rpm and 5wt.% solids concentration, part 2



a) Flow rate vs. time for 1050RPM, 10wt.% solids concentration



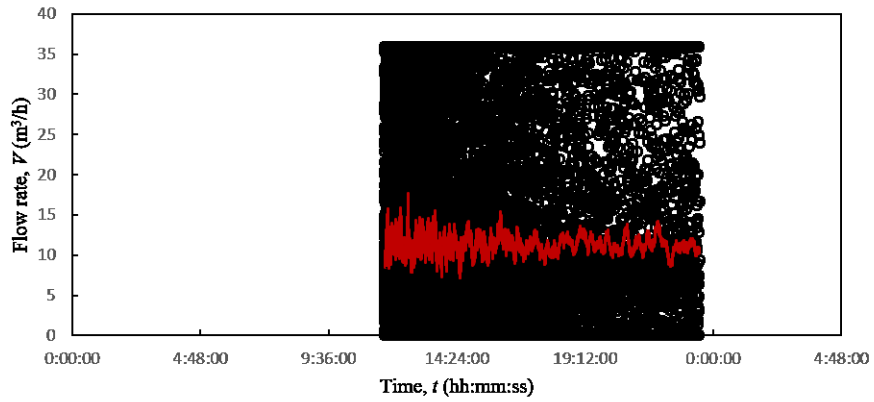
b) Temperature vs. time for 1050RPM, 10wt.% solids concentration



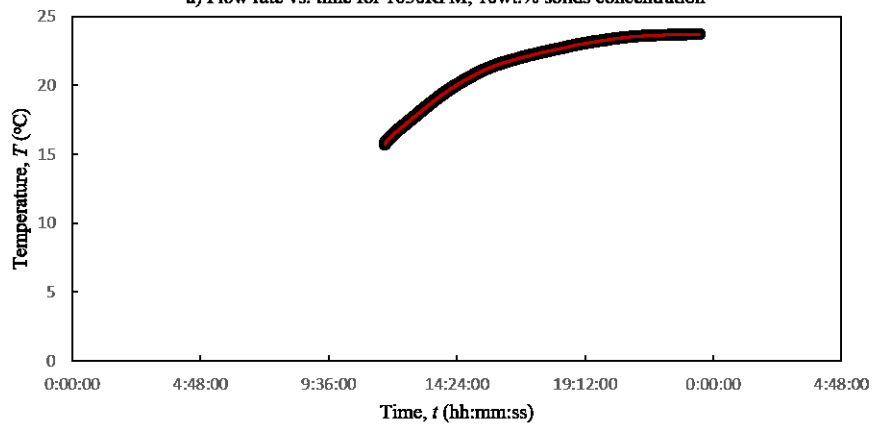
c) Head vs. time for 1050RPM, 10wt.% solids concentration

A.37. Flow rate, temperature and head vs. time in the experiments for 1050 rpm and 10wt.% solids concentration, part 1

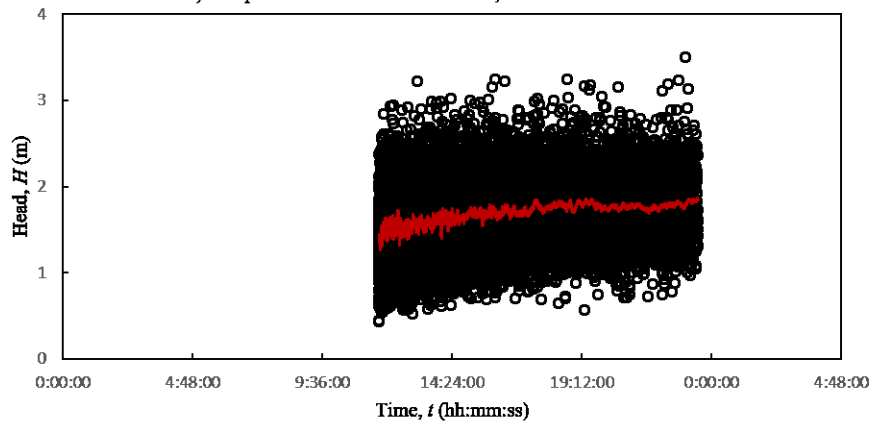




a) Flow rate vs. time for 1050RPM, 10wt.% solids concentration

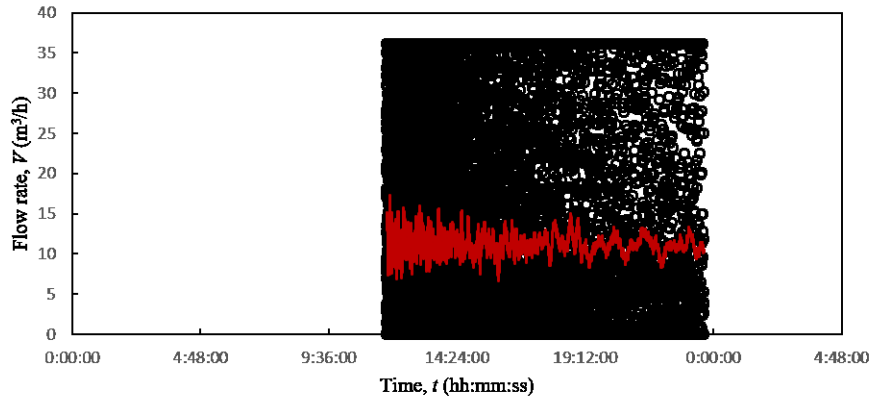


b) Temperature vs. time for 1050RPM, 10wt.% solids concentration

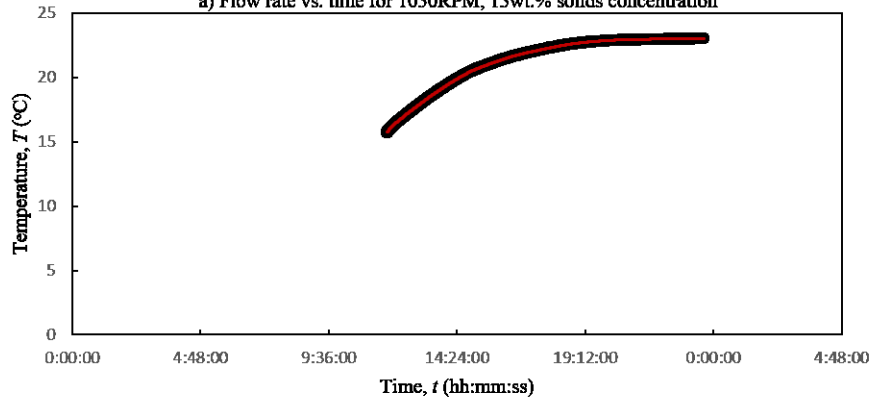


c) Head vs. time for 1050RPM, 10wt.% solids concentration

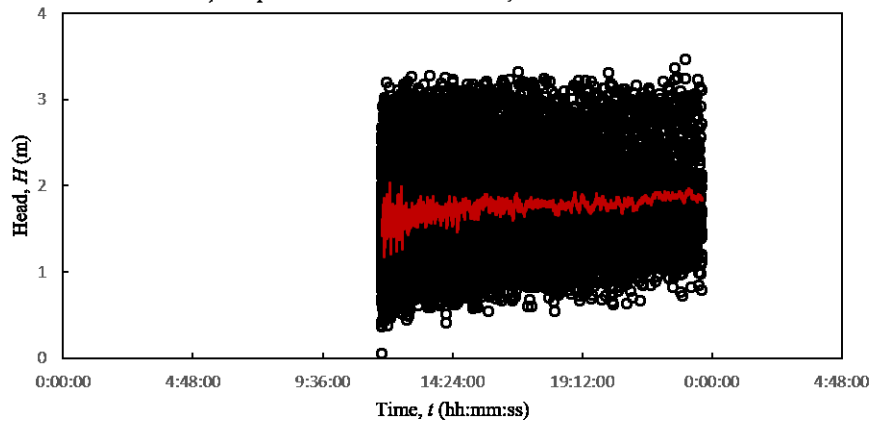
A.38. Flow rate, temperature and head vs. time in the experiments for 1050 rpm and 10wt.% solids concentration, part 2



a) Flow rate vs. time for 1050RPM, 15wt.% solids concentration

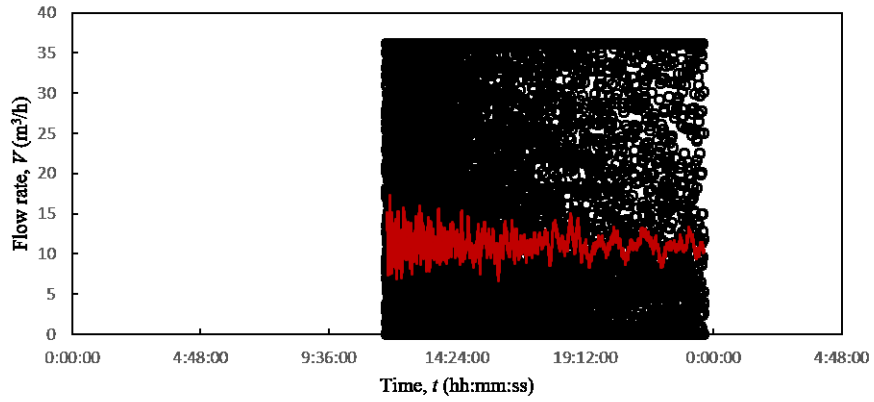


b) Temperature vs. time for 1050RPM, 15wt.% solids concentration

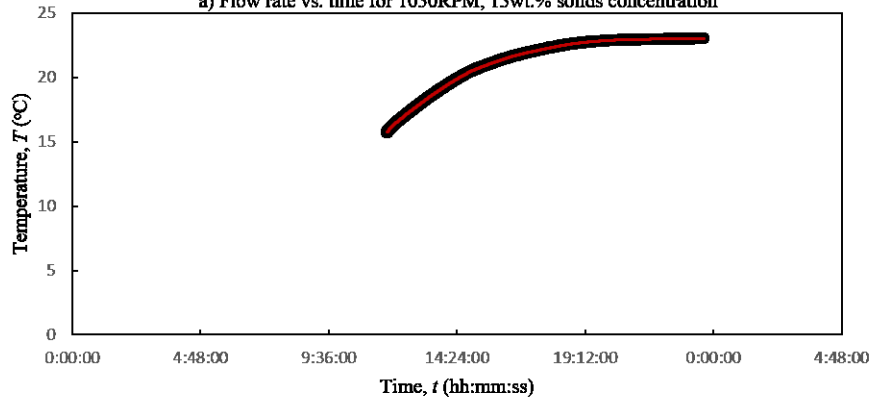


c) Head vs. time for 1050RPM, 15wt.% solids concentration

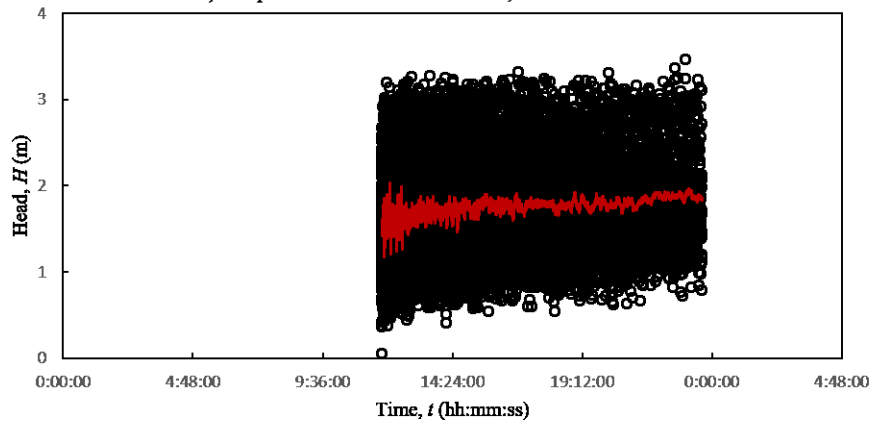
A.39. Flow rate, temperature and head vs. time in the experiments for 1050 rpm and 15wt.% solids concentration, part 1



a) Flow rate vs. time for 1050RPM, 15wt.% solids concentration



b) Temperature vs. time for 1050RPM, 15wt.% solids concentration



c) Head vs. time for 1050RPM, 15wt.% solids concentration

A.40. Flow rate, temperature and head vs. time in the experiments for 1050 rpm and 15wt.% solids concentration, part 2